

ENGINEERING PERSPECTIVE

CONTENTS

<u>Research Articles</u>	<u>Page Number</u>
Yanan CAMARAZA-MEDINA, Abel HERNANDEZ-GUERRERO, Jose L. LUVIANO-ORTIZ View Factor Calculations Between Triangular Surfaces	49-59
Racha BAYZOU, Adrien SOLOY, Thomas BARTOLI, Fatima HAIDAR Thermal Model of Lithium-Ion Batteries for Hybrid Electric Vehicles	60-67
Edson da Graça M. CUMBE, Ângelo António PASCOAL, Valdemar FULANO, Domingos do Rosário N. JOÃO, Philemon NIYOGAKIZA, Marc NSHIMIYIMANA, Yenezer Genene HAILE Analysis of the Seismic Vulnerability of a 3-Story Building, Using Typical Structural Sizing Methods Used In Mozambique	68-84
Mustafa YAZAR, Hilal KIR, Şükrü TALAS The Effect of Welding Wire Feed Speed on Weld Bead Penetration, Length and Width in Robotic Gas Metal Arc Welding	85-89
Jean Claude SUGIRA, Jean de Dieu NINTERETSE, Marc NSHIMIYIMANA, Philemon NIYOGAKIZA Comparative Analysis of Road Safety Performance in Sub-Saharan African Countries Using Road Safety Performance Index	90-99

ENGINEERING PERSPECTIVE

Volume: 5

Issue: 2

30 June 2025

ENGINEERING PERSPECTIVE

An International Journal

Volume: 5 Issue: 2 30 June 2025

e-ISSN: 2757-9077

Open Access

ENGINEERING PERSPECTIVE

An International Journal

Publishing Manager
Prof. Dr. Hamit SOLMAZ

Editor
Assoc. Prof. Dr. Alper CALAM

Subject Editors

Dr. Lina Montuori, Universitat Politècnica de València (UPV), Spain
Dr. Gang Li, Mississippi State University, USA
Dr. Xing Zheng Wu, Hebei University in Baoding, China
Dr. Mamdouh El Haj Assad, University of Sharjah, United Arab Emirates
Dr. Anle Mu, Xi'an University of Technology, China
Dr. Gulsen Taskin, Gazi University, Türkiye
Dr. Anderson Chu, Columbia University, USA
Dr. Diego Fettermann, Federal University of Santa Catarina (UFSC), Brazil
Dr. Sivasankaran Sivanandam, King Abdulaziz University, Kingdom of Saudi Arabia
Dr. Aniefiok Livinus, University of Uyo, Nigeria
Dr. Murat Akin, Gazi University, Türkiye
Dr. Seyed Mohammad Safieddin Ardebili, Shahid Chamran University of Ahvaz, Iran
Dr. Gultekin Uzun, Gazi University, Türkiye
Dr. Babak Keykhosro Kiani, International Institute of Earthquake Engineering and Seismology, Iran
Dr. Mingjun Xu, Nanyang Technological University, Singapore
Dr. Malek Hassanpour, Osmania University, India
Dr. Seyfettin Vadi, Gazi University, Türkiye

Editorial Board

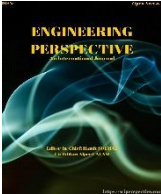
Dr. J. Sadhik Basha, National University of Science & Technology (IMCO), Oman
Dr. Farzad Jaliliantabar, Universiti Malaysia Pahang, Malaysia
Dr. Bakenaz A. Zeidan, Tanta University, Egypt
Dr. Roohollah Zanganeh, Iran University of Science and Technology (IUST), Iran
Dr. Praveen Kumar Dadheech, Rajasthan Technical University Kota, India
Dr. Behrouz Khoshbakht Irdmoussa, Michigan Technological University, USA
Dr. N. Shivakumar, Aarupadai Veedu Institute of Technology, India
Dr. Tamilselvan Pachiannan, Jiangsu University, China
Dr. Andrei Alexandru BoroIU, University of Pitesti, Romania
Dr. Tugba Tabanligil Calam, Gazi University, Türkiye
Dr. Kamran Poorghasemi, Islamic Azad University, Iran
Dr. Omar Bait, University of Batna, Algeria
Dr. Anilkumar Shere, Indian Institute of Technology Delhi, India
Dr. Sujit Kumar Verma, GLA University, India
Dr. Seyfi Polat, Hitit University, Türkiye
Dr. Freddie Inambao, University of KwaZulu-Natal, South Africa
Dr. Ridha Ennetta, Gabes University, Tunis
Dr. Mohammad Amini, University of Saskatchewan, Canada

Language Editor

Dr. Burtay Hatice İnce, Gazi University, Türkiye

Volume: 5	Issue: 2	30 June 2025
Engineering Perspective publishes four issues per year.		

REVIEWERS WHO CONTRIBUTED TO THIS ISSUE (VOLUME: 5 ISSUE: 2)	
Dr. Mehmet Tahir Erdinç	Dr. İlker Göktepeli
Dr. Othmane Zakir	Dr. Mehdi Oubahmane
Dr. Muhirwa Fernand	Dr. Ceyhun Aksoylu
Dr. Emre Korkmaz	Dr. Murathan Kalender
Dr. Ali Payidar Akgüngör	Dr. Mehmet Ali Dereli
<u>Correspondence Address :</u> Gazi University, Faculty of Technology, Department of Automotive Engineering, Teknikokullar - Ankara, TURKIYE <u>e-mail:</u> engineering@sciperspective.com	
<u>Technical Editor:</u> Regaip Menküç Gazi University	
<u>Layout Editors:</u> İrem Tanış, Gazi University Zehra Ebrar Ağca, Gazi University	



View Factor Calculations Between Triangular Surfaces

Yanan Camaraza-Medina^{1*} , Abel Hernandez-Guerrero¹ , Jose L. Luviano-Ortiz¹ ¹Department of Mechanical Engineering, University of Guanajuato, Guanajuato, Mexico

ABSTRACT

In radiative heat transfer calculations, to determine the view factor between surfaces is crucial. Currently, the available technical literature on the subject lacks an analytical expression for estimating the view factor for combinations of triangular surfaces. An analytical solution requires the summation of multiple integrals, given the changes in the integration contours, which becomes more complex in irregular contours. This work aims to develop an expression for computing the view factor between 32 triangular geometric configurations with a common edge and included angle θ . Very importantly, in modern engineering, mesh generators rarely use rectangles or squares (unless the overall geometry is a perfect cube), with triangular elements being the most commonly used elements. For comparison, 48 cases with diverse geometric relationships were calculated using the analytical solution (AS), numerical integration using Simpson's multiple 1/3 rule (MSR), the Sauer graphical solution (SGS), and Bretzhtsov cross roots (BCR). From eight basic geometries, the view factor was computed for the remaining 24 combinations using the sum rule. In all cases, identical fit values were obtained for MSR and SGS with respect to AS, while BCR showed the best correlation in all cases examined. In all the cases evaluated, the BCR showed the best fits, with an error of $\pm 6\%$ in more than 90% of the sample s, while the MSR showed an average dispersion of $\pm 6\%$ in 65% of the data. Given the practical nature of the contribution and the reasonable values of the fits obtained, the current proposal constitutes a suitable tool for application in thermal engineering.

Keywords: Bretzhtsov cross roots; Radiative heat transfer; Triangular surfaces; View factor

History

Received: 15.03.2025

Revised : 23.04.2025

Accepted: 14.05.2025

Author Contacts: ycamaraza1980@yahoo.com, abel@ugto.mx, luis.luviano@ugto.mx

Cite this paper: Camaraza-Medina, Y., Hernandez-Guerrero, A., Luviano-Ortiz, J. L. (2025). View factor calculation between triangular surfaces. Engineering Perspective, 5 (2), 49-59. <http://dx.doi.org/10.29228/eng.pers.81688>

*Corresponding Author

1. Introduction

In many engineering applications, radiative heat transfer between surfaces needs to be assessed. The view factor allows calculating the fraction of radiant energy emitted by one surface that reaches another. Therefore, the geometric relationship between two surfaces and its influence on the view factor has been the subject of research for decades. In previous work, various analytical and numerical solutions have been proposed for different configurations [1-5]. An expanded collection of view factors for over 340 different configurations is provided by Howell [6].

Several methods are known in the literature for estimating view factors, including graphical, analytical, and visual methods. Furthermore, using the summation rule and the algebraic factor, view factors of already known geometries can be used to determine other view factors of derived or more complex geometries [7-10].

The current increase in data processing in computational techniques has enabled the use of commercial programs based on the Finite Element Method (FEM) to solve various heat transfer problems, including thermal radiation. Solutions for edge and border

problems generally reduce to surfaces with a common edge and included angle θ , for which analytical solutions are already known [11-15]. However, in modern engineering, mesh generators rarely use rectangles or squares (unless the overall geometry is a perfect cube), with triangular elements being the most commonly used.

The AS of the view factor between triangular geometries requires the summation of multiple integrals, given the changes in the integration contours, which makes it difficult to obtain solutions in complex configurations. Numerical integration can be a partial solution to the problem; however, only a few contributions to the topic are available in the specialized literature [16].

By numerical integration using the RMS and five intervals, the view factors for various triangular geometries with a common edge and an angle $\theta = 90^\circ$ were obtained. The results for the most elementary ones were graphed and the remaining geometries derived using the summation rule [17]. SGS are useful, but they require the interpretation of graphs, which introduces reading and interpretation errors. Therefore, they are not suitable for generating triangular meshes and subsequently calculating view factors, as they lack an

analytical solution or a numerical approximation for their estimation.

The BCR is a mathematical tool that allows for obtaining reasonable fits in the approximations of complex functionals, in addition to generating an analytical expression that includes the boundary conditions or unknowns to be addressed. Therefore, it can be used to calculate view factors without the need to use or interpret graphs. The method in question allows for fitting by sections or branches, with common nodes for several solutions [18, 19]. Its mathematical conception is similar to that of the FEM, making it suitable for this work.

Currently, there is no analytical expression in the specialized literature that allows directly calculating the view factor for combinations of triangular surfaces. In the expanded compilation of view factor configurations available for the case of finite triangular surfaces, it is verified that only Sauer's graphical results are used [6]. In other consulted sources, Sauer graphs are also presented for the determination of view factors [18, 20]. The above shows that currently there are no exact or approximate analytical solutions for the determination of view factors between triangular geometries with a common edge and included angle θ , which is the main objective of this work.

Therefore, this research aims to develop approximate solutions that allow computing the view factor in various triangular geometries. These solutions do not present high mathematical complexity and their correlation with respect to the AS provides a better fit than the SGS. This constitutes a new analytical method for application to the calculation of view factors using FEM and to constituting new expressions that can be included in existing catalogs.

In this work, the exact analytical solutions for eight basic triangular geometries and their respective Bretzhtsov cross roots are given. For comparison, 48 examples with various aspect ratios were calculated for each geometry, using the AS, the numerical solution of the quadruple integral using the MSR with five intervals, the SGS and the view factors calculated using the BCR. From the eight basic geometries, the view factor for another 24 triangular geometries is obtained using the summation rule. In all cases, identical fit values were obtained for RMS and SGS with respect to AS, while BCR showed the best fit in all cases examined, confirming the validity of the hypothesis regarding its use.

Given the practical nature of the contribution and the reasonable values of the fits obtained, the proposal presented in this work constitutes a suitable tool for application in thermal engineering and related practices that require thermal radiation calculations.

2. Materials and methods

2.1 Basic considerations on the view factor

The view factor is fundamental to the exchange of radiant energy. It depends on the configuration and position of the receiving and emitting surfaces, making its evaluation complex and, in many cases, generating erroneous results. Then, the view factor F_{12} is the fraction of the radiation emitted by surface A_1 that is intercepted by surface A_2 , expressed as [21]:

$$F_{12} = \frac{1}{\pi A_1} \int_{A_1} \int_{A_2} \frac{\cos \theta_1 \cos \theta_2}{r^2} dA_1 dA_2 \quad (1)$$

where A_1, A_2 are the emitting and receiving surfaces, respectively; θ_1, θ_2 are the angles between the normal vector to the area $dA_1 dA_2$ and the line joining the centers of surfaces A_1, A_2 , respectively; r is the distance between the centers of surfaces A_1 and A_2 (see Figure 1).

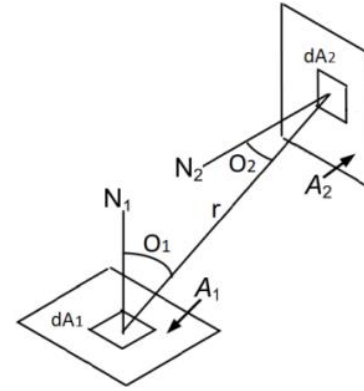


Figure 1. Basic geometry for view factor definition

Eq. (1) includes double integration, which in many cases can be a very laborious mathematical problem. Therefore, calculating the view factor in any geometry requires handling a considerable amount of integrals and solving complex mathematical equations. To simplify the analysis, numerical approximations are used that provide adequate fits, with a reasonable margin of error, allowing for its application in practical engineering. For three-dimensional configurations, several methods can be implemented to estimate the view factor, such as direct integration, contour integration, summation and reciprocity techniques, MSR, Monte Carlo, ray tracing, FEM, and matrix methods [22-28].

In this investigation, the direct integration method was implemented to obtain the view factors associated with the 32 configurations studied. The BCR method was used to approximate the special functions generated in direct integration.

2.2 Mathematical solution for the view factor

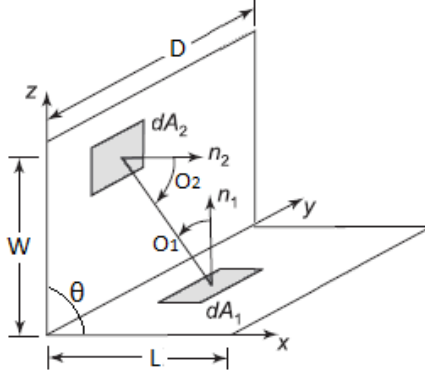
The view factor between two finite rectangles of the same width with a common edge and included angle θ (see Figure 2) is given by:

$$f_{(1)} = \frac{\sin^2 \theta}{\pi A_1} \int_0^L dy_1 \int_0^D dx \int_0^W dz \int_0^D \frac{xz}{\{(y_1 - y_2)^2 + x^2 + z^2 - 2xz \cos \theta\}^2} dy_2 \quad (2)$$

To evaluate Eq. (2) the following definitions are used:

$$X = W/D \quad ; \quad Y = L/D \quad ; \quad R = \frac{\sqrt{X^2 + Y^2 - 2XY \cos \theta}}{\sqrt{X^2 + Y^2 - 2XY \cos \theta}} \quad (3)$$

$$f_{(1)} = F_{a-b} = \frac{1}{\pi Y} \left\{ -\frac{\sin 2\theta}{4} \left\{ Y^2 \tan^{-1} \left(\frac{X}{Y} \csc \theta - \cot \theta \right) + X^2 \tan^{-1} \left(\frac{Y}{X} \csc \theta - \cot \theta \right) + XY \sin \theta + \left(\frac{\pi}{2} - \theta \right) (X^2 + Y^2) \right\} + \right. \\ \left. + \frac{1}{4} \ln \left\{ \left(\frac{X^2}{R^2} \left(\frac{1+X^2}{1+R^2} \right) \cos 2\theta \right)^{X^2 \sin^2 \theta} \left(\frac{Y^2+Y^2 R^2}{R^2+Y^2 R^2} \right)^{Y^2 \sin^2 \theta} \left(\frac{(1+X^2)(1+Y^2)}{1+R^2} \right)^{\cos^2 \theta + 1} \right\} + \right. \\ \left. + (\sin^3 \theta \cos \theta) \tan^{-1} \left(\frac{Y \sin \theta \sqrt{X^2 + \cot^2 \theta + 1}}{X^2 - YX \cos \theta + 1} \right) \sqrt{X^4 + X^2 (\cot^2 \theta + 1)} + X \tan^{-1} \left(\frac{1}{X} \right) + \right. \\ \left. + Y \tan^{-1} \left(\frac{1}{Y} \right) - R \cot^{-1}(R) + \frac{\sin 2\theta}{2} \int_0^Y \sqrt{z^2 + \cot^2 \theta + 1} \tan^{-1} \left(\frac{X \sin \theta \sqrt{z^2 + \cot^2 \theta + 1}}{z^2 - zX \cos \theta + 1} \right) dz \right\} \quad (4)$$

Figure 2. Rectangles with common edge and included angle θ

Evaluating Eq. (2), the following solution is obtained [29]:

In Eq. (2) and (4) the angle θ is given in radians. In a previous investigation [30], an expression similar to Equation (4) was obtained to solve the quadruple integral given in Eq. (2), tabulating the values of the viewing factors for the angles $\theta = (30^\circ; 45^\circ; 60^\circ; 90^\circ; 120^\circ; 135^\circ; 150^\circ)$. These values were later corrected because they sometimes violated the summation rule [31-33].

Eq. (4) is very complex. The last integral lacks primitives, so it was not possible to solve it. Therefore, its solution will be obtained using the MSR (with eight intervals). At each interval of the numerical integration, the variable z is replaced by its corresponding fraction of the length of the emitting surface L (see Table 1), obtaining a solution (ω_n) for each interval [29].

Table 1. Definition of z-scores for the MSR in Eq. (4).

0	Int. 1	Int. 2	Int. 3	Int. 4	Int. 5	Int. 6	Int. 7	Int. 8
0	0.125L	0.25L	0.375L	0.5L	0.625L	0.75L	0.875L	L
ω_1	ω_2	ω_3	ω_4	ω_5	ω_6	ω_7	ω_8	ω_9

Therefore, the numerical evaluation of the last integral given in Eq. (4) can be calculated as:

$$\int_0^Y \left\{ \sqrt{1 + z^2 \sin^2 \theta} \tan^{-1} \left(\frac{X \sqrt{1 + z^2 \sin^2 \theta}}{z^2 - zX \cos \theta + 1} \right) \right\} dz \cong \frac{L}{24} (\omega_1 + \omega_9 + 2(\omega_3 + \omega_5 + \omega_7) + 4(\omega_2 + \omega_4 + \omega_6 + \omega_8)) \quad (5)$$

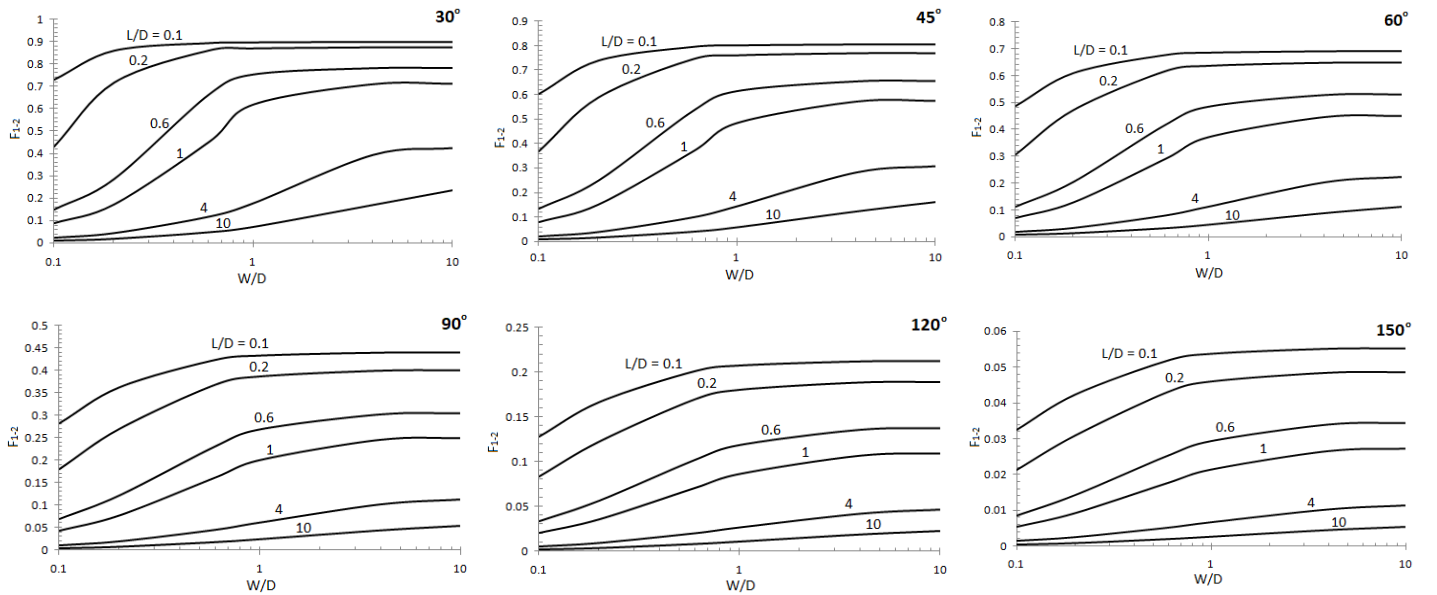
If $\theta = 90^\circ$, then Eq. (4) simplifies to the following relation:

$$f_{(1)} = \frac{1}{\pi Y} \left\{ X \tan^{-1} \left(\frac{1}{X} \right) + Y \tan^{-1} \left(\frac{1}{Y} \right) - R \cot^{-1}(R) + \frac{1}{4} \ln \left\{ \left(\frac{X^2 + X^2 R^2}{R^2 + X^2 R^2} \right)^{X^2} \left(\frac{Y^2 + Y^2 R^2}{R^2 + Y^2 R^2} \right)^{Y^2} \left(\frac{(1+X^2)(1+Y^2)}{1+R^2} \right) \right\} \right\} \quad (6)$$

In Eq. (6), the following definitions are used:

$$X = W/D \quad ; \quad Y = L/D \quad ; \quad R = \sqrt{X^2 + Y^2} \quad (7)$$

Figure 3 shows graphically the solutions to Eq. (4) for values of $\theta = (30^\circ, 45^\circ, 60^\circ, 90^\circ, 120^\circ, 150^\circ)$, in the intervals $0.1 \leq Y; X \leq 10$. For angle values $\theta \neq (30^\circ, 45^\circ, 60^\circ, 90^\circ, 120^\circ, 150^\circ)$, the view factor can be obtained by interpolation.

Figure 3. F_{a-b} values obtained with Eq. (4) for various values of θ .

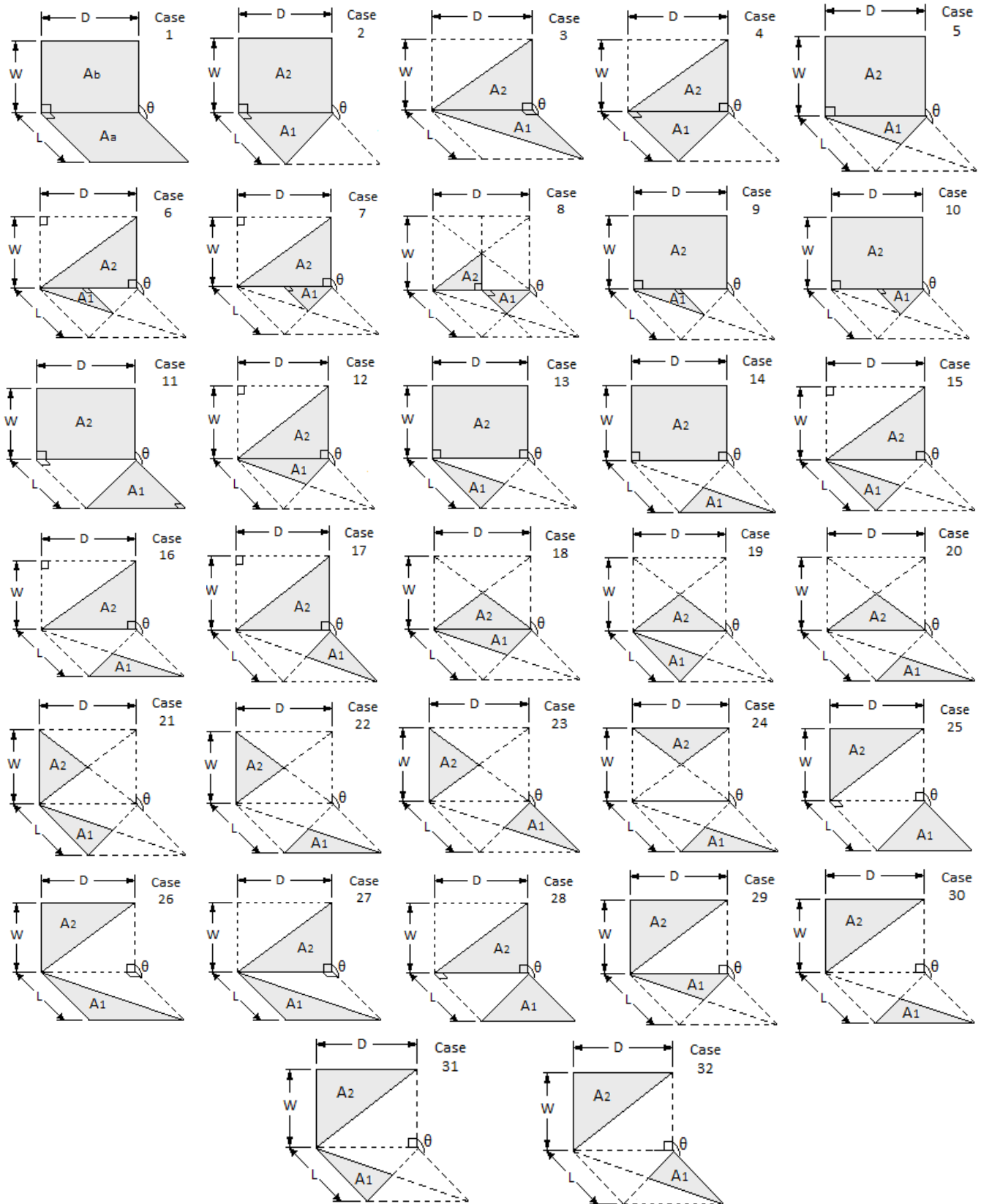


Figure 4. Basic configurations for triangular surfaces

2.3 Mathematical solution for the view factor

In modern engineering, mesh generators rarely use rectangles or squares, unless the overall geometry is a perfect cube. One of the most commonly used elements is triangular ones. The formulation of this type of geometry requires a mathematical approach that includes multiple sums of the quadruple integral. due to the variation of the projection contours on the coordinate axes. Diagonal lines can be extended over the rectangular surfaces in Figure 2, subdividing the rectangular plane domain into triangular elements (see Figure 4).

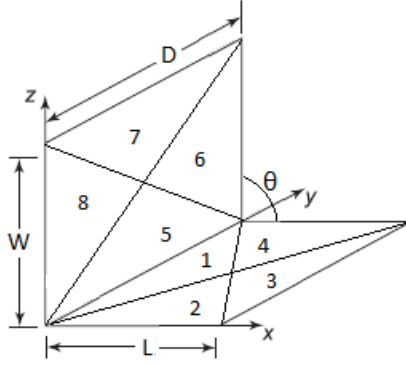


Figure 5. Decomposition of triangular elements

In Figure 5, the leaving and reaching surfaces A_a and A_b are divided into four triangular surfaces, with 64 possible combinations. The reciprocity of the viewing factors establishes that $A_a F_{a-b} = A_b F_{b-a}$; therefore, only 32 combinations will be evaluated. The basic geometries (Cases 1 to 8) and derived geometries (Cases 9 to 32) are given in Figure 4. The basic geometries (Cases 1 to 8) con-

stitute the basis of the study conducted, as the remaining combinations can be generated from them using the summation rule.

2.4 Mathematical modeling of the view factor

2.4.1 Case 2

In Case 2, the emitting and receiving surfaces are a rectangle and a right triangle, respectively, with common side D and angle θ between both surfaces. In Case 2 (see Figure 6), the integration limits are set for each projection on surfaces A_1 and A_2 , obtaining the following relation:

$$f_{(2)} = \frac{\sin^2 \theta}{\pi A_1} \int_0^L dy_1 \int_0^{\frac{y_1 D}{L}} dx \int_0^W dz \int_0^D \frac{xz}{\{(y_1 - y_2)^2 + x^2 + z^2 - 2xz \cos \theta\}^2} dy_2 \quad (8)$$

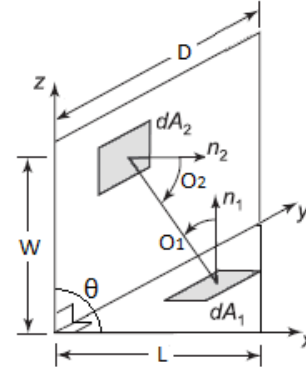


Figure 6. Basic Geometry for Case 2

The solution of Eq. (8) is given by:

$$\begin{aligned} f_{(2)} = 2f_{(1)} & \left\{ \frac{X^2}{2(X^2+1)^2} \ln \left\{ \left(\frac{1}{X} \right)^{2X^2} \left(\frac{X^2+Y^2}{Y^2+1} \right) \left(\frac{1}{X(X^2+Y^2)} \right)^{(X^2+1)} \right\} + \frac{1}{4} X^2 \ln \left\{ \left(\frac{X^6}{(X^2+1)^2} \right) \left(\frac{X^2+Y^2+1}{X^2+Y^2} \right) \right\} - \sqrt{X^2+Y^2} \tan^{-1} \left(\frac{1}{\sqrt{X^2+Y^2}} \right) + \right. \\ & \frac{1}{4} \ln \left\{ (X^2+1) \left(\frac{Y^2+1}{X^2+Y^2+1} \right) \right\} + \frac{1}{4} Y^2 \ln \left\{ \frac{Y^4(X^2+Y^2+1)}{(Y^2+1)(X^2+Y^2)^2} \right\} + Y \tan^{-1} \left(\frac{1}{Y} \right) + \frac{(X^2+1)(X^4+3X^2)+2X\pi(X^2-\frac{1}{2}(3X^2+1))}{4(X^2+1)^2} + \\ & \frac{X^3 \left(\frac{1}{X^2+1} - Y^2 - 1 \right)}{(X^2+1)^{\frac{3}{2}} \sqrt{X^2 Y^2 - \frac{X^2}{X^2+1} + X^2}} \tan^{-1} \left(\frac{X(X^2+1)^{\frac{3}{2}} \sqrt{X^2 Y^2 - \frac{X^2}{X^2+1} + X^2}}{(X^2+1) \left(X^2 Y^2 - \frac{X^2}{X^2+1} + X^2 \right) - X^4} \right) + \frac{3}{2} X \tan^{-1} \left(\frac{1}{X} \right) + \frac{X^2}{4(X^2+1)} \ln \left\{ \frac{Y^2+1}{(X^2+Y^2)X^2} \right\} + \frac{X^2 Y^2}{4(X^2+1)} \ln \left\{ \frac{X^2+2Y^2+1}{Y^2(X^2+Y^2)} \right\} + \\ & \left. 1 \right\} - \frac{1}{X} \int_0^X \left\{ \frac{z^2}{\sqrt{z^2+Y^2}} \tan^{-1} \left(\frac{\frac{1}{X^2}(z^2-Xz)+z^2+Y^2}{\frac{1}{X^2}} \right) + \frac{z}{\sqrt{z^2+Y^2}} \tan^{-1} \left(\frac{\frac{z}{X}-1}{\sqrt{z^2+Y^2}} \right) \right\} dz \end{aligned} \quad (9)$$

In Eq. (9) the term $f_{(1)}$ is the view factor computed with Eq. (4). Solving Eq. (8) requires solving $n^n = 4^4 = 256$ primitive functions. However, the last integral was not solved because no primitive functions existed for it, requiring a solution using the MSR (with seven intervals). Obtaining an analytical solution to Eq. (8) is extremely complex, as it involves the summation of infinite series with polylogarithms. An alternative solution is to treat these special functions as complex variables, with the addition of polynomials, which progressively tend toward convergence of the infinite Spence series, using BCR. Case 2 was obtained from the decomposition of rectangular surfaces into triangular elements (see Figure 4); therefore, the solution to the quadruple integral of Eq. (8) is derived from Eq. (4) and can be expressed as:

$$F_{1-2} = \varphi \cdot f_{(1)} \quad (10)$$

where $f_{(1)}$ is the view factor computed with Equation (4) and φ is the BCR.

The BCR is obtained from a stationary sum of view factors, fitting the family of curves generated in the evaluated domain using polynomials. There will be as many curves to fit as terms considered in the sum of the series of polylogarithms; therefore, the increase in the intervals will be proportional to the accuracy obtained in the results. In Equation (4), it is observed that the view factor depends on two parameters X, Y with a common denominator D; therefore, the real root will be a function of these. The common side D is opposite to the dimensions W, L on the surfaces A_a and A_b , which indicates that the period of the complex function is given by [18]:

$$\psi = \tan^{-1}(X/Y) \quad (11)$$

To apply the BCR, the solution to Eq. (10) is graphically represented in the interval $0.1 \leq X \leq 10$ and $0.1 \leq Y \leq 10$ using values $X = Y = (0.1; 0.3; 0.6; 1; 3; 6; 10)$ for its construction. Therefore, from the upper and lower nodes, it is possible to draw the curve corresponding to the minimum and maximum values of $Y = (0.1; 10)$. In the infinite polylogarithmic series, a value of Y is fixed, and subsequently the polylogarithms are calculated for each value of X ; with this procedure, a family of curves a is obtained. Next, a similar procedure is applied, but fixing the values of X when calculating the polylogarithms for each value of Y , thus obtaining a family of curves b . Curves a and b are approximated individually using the least squares method, generating polynomials of the form $mX^3 + nX^2 + oX + p$. The constants m, n, o, p are subsequently weighted to generate a single function φ , which depends on the forming angle ψ [19]. Applying the method described in the previous paragraph, the BCR for Case 2 is given by:

$$\varphi_2 = (-0,022Y^3 + 0,316Y^2 - 0,89Y + 0,5)\psi^2 + (0,056Y^3 - 0,783Y^2 + 2,23Y - 1,43)\psi - 0,03Y^3 + 0,407Y^2 - 1,07Y + 2,02 \quad (12)$$

Substituting Eq. (4) and (12) in Eq. (11), the view factor for Case 2 is obtained through the BCR, which is given by the following relation:

$$f_{(2)} = F_{(1-2)} = \varphi_2 \cdot f_{(1)} \quad (13)$$

Figure 7 presents graphically the solution of Eq. (13) for $\theta = 90^\circ$.

2.4.2 Cases 3 to 8

$$\text{Case 3} \quad f_{(3)} = \frac{1}{\pi A_1} \iint \frac{\cos O_1 \cos O_2 dA_1 dA_2}{r^2} = \frac{\sin^2 \theta}{\pi A_1} \int_0^L dy_1 \int_0^{y_1 D/L} dx \int_0^W dy_2 \int_0^{y_2 D/W} \frac{xz}{\{(y_1 - y_2)^2 + x^2 + z^2 - 2xz \cos \theta\}^2} dz \quad (14)$$

$$\text{Case 4} \quad f_{(4)} = \frac{1}{\pi A_1} \iint \frac{\cos O_1 \cos O_2 dA_1 dA_2}{r^2} = \frac{\sin^2 \theta}{\pi A_1} \int_0^L dy_1 \int_0^{y_1 D/L} dx \int_0^W dy_2 \int_0^{y_2 D/W} \frac{xz}{\{(y_1 - y_2)^2 + x^2 + z^2 - 2xz \cos \theta\}^2} dz \quad (15)$$

$$\text{Case 5} \quad f_{(5)} = \frac{1}{\pi A_1} \iint \frac{\cos O_1 \cos O_2 dA_1 dA_2}{r^2} = \frac{\sin^2 \theta}{\pi A_1} \int_0^{L/2} dy_1 \int_0^{y_1 D/L} dx \int_0^W dz \int_0^Z \frac{xz}{\{(y_1 - y_2)^2 + x^2 + z^2 - 2xz \cos \theta\}^2} dy_2 \quad (16)$$

$$\text{Case 6} \quad f_{(6)} = \frac{1}{\pi A_1} \iint \frac{\cos O_1 \cos O_2 dA_1 dA_2}{r^2} = \frac{\sin^2 \theta}{\pi A_1} \int_0^{L/2} dy_1 \int_0^{y_1 D/L} dx \int_0^W dy_2 \int_0^{y_2 D/W} \frac{xz}{\{(y_1 - y_2)^2 + x^2 + z^2 - 2xz \cos \theta\}^2} dz \quad (17)$$

$$\text{Case 7} \quad f_{(7)} = \frac{1}{\pi A_1} \iint \frac{\cos O_1 \cos O_2 dA_1 dA_2}{r^2} = \frac{\sin^2 \theta}{\pi A_1} \int_0^{L/2} dy_1 \int_{-y_1 D/L}^0 dx \int_0^W dy_2 \int_0^{y_2 D/W} \frac{xz}{\{(y_1 - y_2)^2 + x^2 + z^2 - 2xz \cos \theta\}^2} dz \quad (18)$$

$$\text{Case 8} \quad f_{(8)} = \frac{1}{\pi A_1} \iint \frac{\cos O_1 \cos O_2 dA_1 dA_2}{r^2} = \frac{\sin^2 \theta}{\pi A_1} \int_0^{L/2} dy_1 \int_{-y_1 D/L}^0 dx \int_0^{W/2} dy_2 \int_0^{y_2 D/W} \frac{xz}{\{(y_1 - y_2)^2 + x^2 + z^2 - 2xz \cos \theta\}^2} dz \quad (19)$$

The BCR for each case are given by:

$$\text{Case 3} \quad f_{(3)} = f_{(1)} \cdot \{(-0,001Y^3 + 0,033Y^2 - 0,14Y + 0,265)\psi^2 + (0,011Y^3 - 0,177Y^2 + 0,7Y - 0,615)\psi - 0,01Y^3 + 0,142Y^2 - 0,475Y + 1,29\} \quad (20)$$

$$\text{Case 4} \quad f_{(4)} = f_{(1)} \cdot \{(-0,031Y^3 + 0,424Y^2 - 1,275Y + 1,1)\psi^2 + (0,071Y^3 - 0,975Y^2 + 2,92Y - 2,06)\psi - 0,034Y^3 + 0,462Y^2 - 1,268Y + 1,6\} \quad (21)$$

$$\text{Case 5} \quad f_{(5)} = f_{(1)} \cdot \{(-0,01Y^2 + 0,24Y + 0,67)\psi^2 + (0,02Y^2 - 0,31Y - 2,2)\psi - 0,02Y^2 + 0,27Y + 3\} \quad (22)$$

Cases 3 to 8 are reduced to the following geometries:

Case 3: right triangle to right triangle, with a common side and angle θ between both surfaces: vertices at a common point

Case 4: right triangle to right triangle, with a common side and angle θ between both surfaces: vertices at opposite ends

Case 5: isosceles triangle to right triangle, with a common side and angle θ between both surfaces

Case 6: right triangle to right triangle of different sizes, with angle θ between both surfaces: vertices at a common point

Case 7: right triangle to right triangle of different sizes, with angle θ between both surfaces: vertices at opposite ends

Case 8: perpendicular right triangles with an equal edge and arranged in opposite directions.

In Cases 3 to 8 (see Figure 5), the integration limits are established for each projection on surfaces A_1 and A_2 , obtaining the following integral relations:

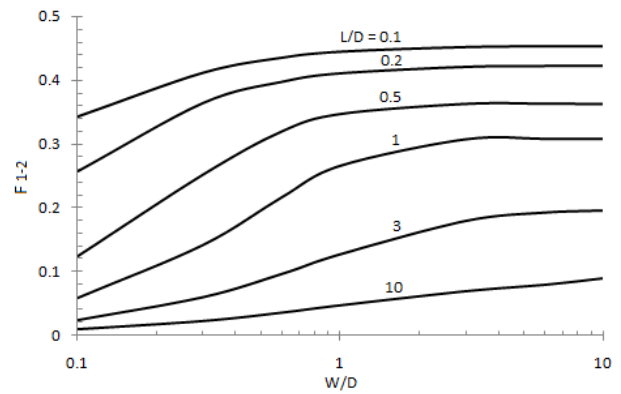


Figure 7. Graphical solution of Eq. (13) for $\theta = 90^\circ$

$$\text{Case 6} \quad f_{(6)} = f_{(1)} \cdot \{(-0,02Y^3 + 0,29Y^2 - 1,1Y + 0,6)\psi^2 + (0,06Y^3 - 0,88Y^2 + 2,96Y - 1,41)\psi - 0,04Y^3 + 0,55\} \quad (23)$$

$$Y^2 + 1,41Y + 1,87\}$$

$$\text{Case 7} \quad f_{(7)} = f_{(1)} \cdot \{(-0,011Y^3 + 0,12Y^2 - 0,025Y + 0,52)\psi^2 + (0,025Y^3 - 0,307Y^2 + 0,49Y - 1,64)\psi - 0,014\} \quad (24)$$

$$Y^3 + 0,183Y^2 - 0,35Y + 2,47\}$$

$$\text{Case 8} \quad f_{(8)} = f_{(1)} \cdot \{(0,015Y^2 - 0,108Y + 0,08)\psi^2 + (-0,015Y^2 + 0,096Y + 0,048)\psi - 0,001Y^2 + 0,04Y + 0,058\} \quad (25)$$

Figure 8 gives a graphical solution to Eq. (20) to (22), for $\theta = 90^\circ$.

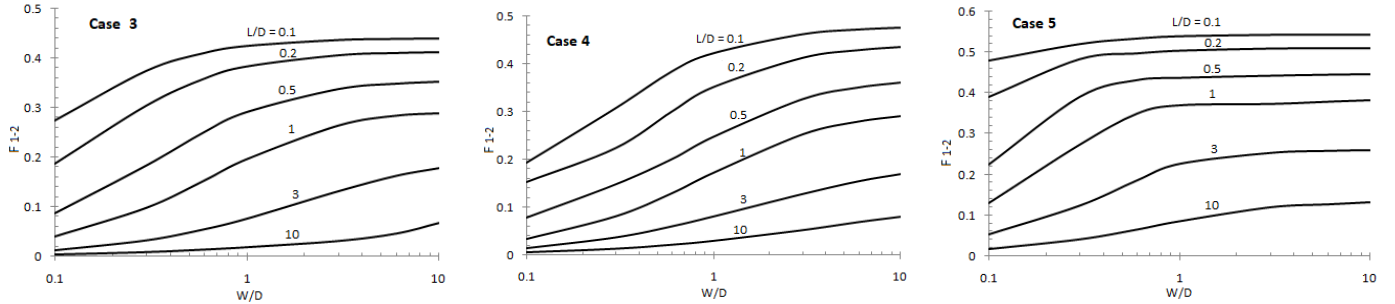


Figure 8 Graphical solutions of Equations (20) to (22) for $\theta = 90^\circ$.

Figure 9 gives a graphical solution to Eq. (23) to (25), for $\theta = 90^\circ$.

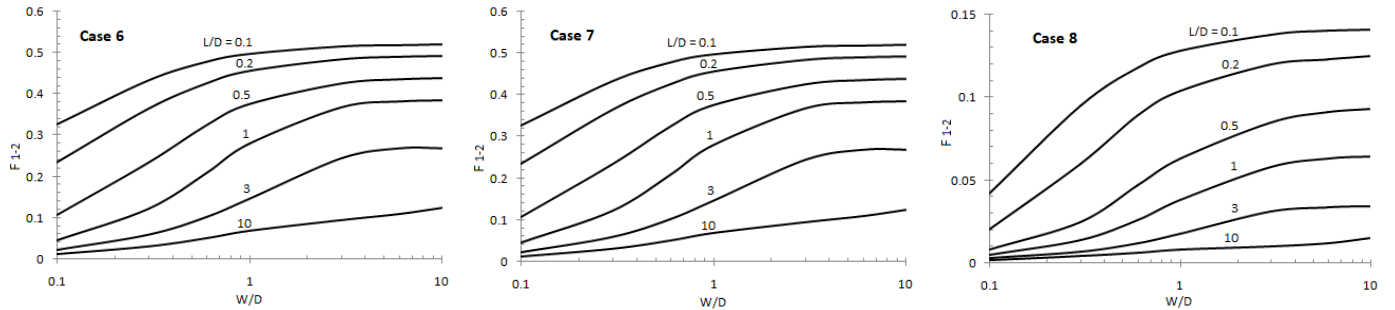


Figure 9 Graphical solutions of Equations (22) to (25) for $\theta = 90^\circ$.

2.4.3 Cases 9 to 32

By combining the view factors $f_{(1)}$ to $f_{(8)}$ it is possible to obtain the view factors for Cases 9 to 32 by applying the summation rule and the algebra of view factors. Table 2 summarizes the relationships for computing the view factor in the derived configurations (see Figure 4).

3 Analysis of Results

The percentage of deviation (error) is calculated with respect to the AS and computed as follows:

$$D_{\%} = 100 \cdot \left(\frac{SA - Val}{SA} \right) \quad (26)$$

Where: $D_{\%}$ is the percentage of deviation, in %, AS is the view factor computed using the analytical solution, and Val is the view factor obtained using other methods.

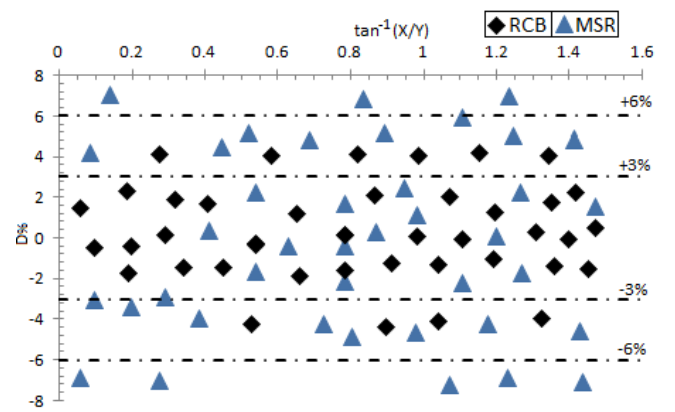


Figure 10. $D_{\%}$ values computed for Case 2

Figure 10 shows the $D_{\%}$ obtained with Eq. (26) for 42 view factors in the range $0.1 \leq X, Y \leq 10$ calculated with MSR and BCR for Case 2, plotted in error bands of $\pm 3\%$ and $\pm 6\%$.

For Case 2, Figure 10 shows that the BCR provides a better fit with respect to the AS, with a mean error of $\pm 3\%$ and $\pm 6\%$ for 80.8% and 100% of the points (Y,X) analyzed. In contrast, the view factors obtained with MSR provide a weaker fit respect to the AS, with mean errors of $\pm 3\%$ and $\pm 6\%$ for 42.9% and 88.1% of the points (Y,X) evaluated, respectively.

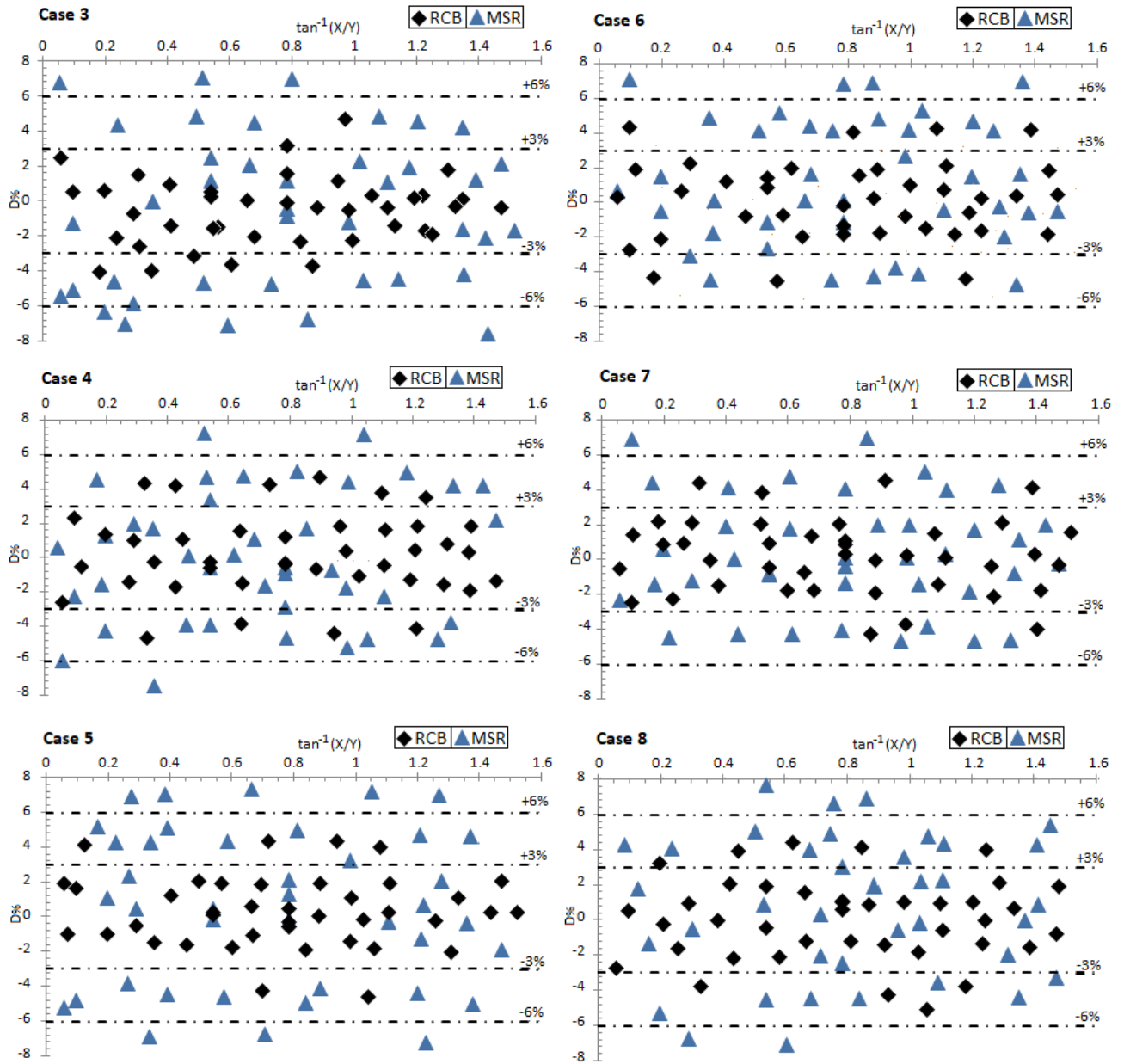


Figure 11. D_{θ} values for Cases 3 to 8.

Figure 11 shows the D_{θ} obtained using Eq. (26) for 42 view factors in the range $0.1 \leq X, Y \leq 10$, calculated using MSR and BCR for Cases 3 to 8, in error bands of $\pm 3\%$ and $\pm 6\%$.

For Case 3, Figure 11 shows that the BCR provides the best fit with respect to the AS, with an average error of $\pm 3\%$ and $\pm 6\%$ in 85.7% and 100% of the points (Y,X) analyzed. In contrast, the view factors obtained using MSR produce a weaker fit with respect to the AS, with average errors of $\pm 3\%$ and $\pm 6\%$ in 45.2% and 81.1% of the points (Y, X) evaluated, respectively.

For Case 4, Figure 11 shows that the BCR provide a better fit than the

AS, with mean errors of $\pm 3\%$ and $\pm 6\%$ in 76.2% and 100% of the points (Y,X) analyzed, while the view factors obtained with MSR provide a weaker fit with respect to the AS, computing mean errors of $\pm 3\%$ and $\pm 6\%$ in 47.6% and 90.5% of the points (Y,X) evaluated, respectively.

For Case 5, Figure 11 shows that the BCR provide a better fit with respect to the AS, with mean errors of $\pm 3\%$ and $\pm 6\%$ in 90.5% and 100% of the points (Y,X) analyzed. In contrast, the view factors obtained with MSR provide a weaker fit with respect to the AS, with mean errors of $\pm 3\%$ and $\pm 6\%$ in 50% and 78.6% of the points (Y,X) evaluated, respectively.

For Case 6, Figure 11 shows that the BCR provide a better fit with respect to the AS, with mean errors of $\pm 3\%$ and $\pm 6\%$ in 83.3% and 100% of the points (Y,X) analyzed, while the view factors obtained with MSR provide a weaker fit with respect to the AS, computing mean errors of $\pm 3\%$ and $\pm 6\%$ in 35.7% and 88.9% of the points (Y,X) evaluated, respectively.

For Case 7, Figure 11 shows that the BCR provide a better fit compared to the AS, with mean errors of $\pm 3\%$ and $\pm 6\%$ at 90.5% and 100% of the points (Y,X) analyzed. In contrast, the view factors obtained with MSR provide a weaker fit compared to the AS, with mean errors of $\pm 3\%$ and $\pm 6\%$ at 61.9% and 95.2% of the points (Y,X) evaluated, respectively.

For Case 8, Figure 11 shows that the BCR provide a better fit with respect to the AS, with mean errors of $\pm 3\%$ and $\pm 6\%$ in 76.2% and 100% of the points (Y,X) analyzed, while the view factors obtained with MSR provide a weaker fit with respect to the AS, computing mean errors of $\pm 3\%$ and $\pm 6\%$ in 40.5% and 81.1% of the points (Y,X) evaluated, respectively.

Table 2. View factor for Cases 9 to 32.

Case	$F_{1-2} \dots \{f_{(n)}\}$
Case 9	$f_{(9)} = f_{(5)}$
Case 10	$f_{(10)} = f_{(5)}$
Case 11	$f_{(11)} = 2f_{(1)} - f_{(2)}$
Case 12	$f_{(12)} = f_{(6)} + f_{(7)}$
Case 13	$f_{(13)} = 2f_{(2)} - f_{(5)}$
Case 14	$f_{(14)} = 4f_{(1)} + f_{(5)} - 4f_{(2)}$
Case 15	$f_{(15)} = 2f_{(4)} - f_{(6)} - f_{(7)}$
Case 16	$f_{(16)} = 4f_{(1)} + f_{(6)} + f_{(7)} - 2f_{(3)} - 2f_{(4)}$
Case 17	$f_{(17)} = 2f_{(3)} - f_{(6)} - f_{(7)}$
Case 18	$f_{(18)} = f_{(3)} + f_{(8)}$
Case 19	$f_{(19)} = f_{(6)} + f_{(7)} - f_{(3)} - f_{(8)}$
Case 20	$f_{(20)} = 4f_{(5)} + f_{(3)} + f_{(8)} - 2f_{(6)} - 2f_{(7)}$
Case 21	$f_{(21)} = 3f_{(3)} + f_{(8)} - 2f_{(6)} - 2f_{(7)}$
Case 22	$f_{(22)} = 4f_{(1)} + 3f_{(6)} + 3f_{(7)} - 3f_{(3)} - 2f_{(4)} - 4f_{(5)} - f_{(8)}$
Case 23	$f_{(23)} = 4f_{(5)} + f_{(3)} + f_{(8)} - 2f_{(6)} - 2f_{(7)}$
Case 24	$f_{(24)} = 5f_{(3)} + 4f_{(4)} + 5f_{(5)} + f_{(8)} - 4f_{(1)} - 4f_{(2)} - 4f_{(6)} - 4f_{(7)}$
Case 25	$f_{(25)} = 2f_{(1)} + f_{(4)} - 2f_{(2)}$
Case 26	$f_{(26)} = 2f_{(1)} + f_{(3)} - 2f_{(2)}$
Case 27	$f_{(27)} = f_{(2)} - f_{(3)}$
Case 28	$f_{(28)} = f_{(2)} - f_{(4)}$
Case 29	$f_{(29)} = f_{(5)} - f_{(6)} - f_{(7)}$
Case 30	$f_{(30)} = 2f_{(3)} + 2f_{(4)} + f_{(5)} - 4f_{(2)} - f_{(6)} - f_{(7)}$
Case 31	$f_{(31)} = 2f_{(2)} + f_{(6)} + f_{(7)} - f_{(5)} - 2f_{(4)}$
Case 32	$f_{(32)} = 2f_{(2)} + f_{(6)} + f_{(7)} - f_{(5)} - 2f_{(3)}$

4. Conclusions

Determining the view factor is one of the most important features during analysis of radiant energy exchange, since an analytical solution considerably facilitates the work of thermal engineers, allowing its rapid and accurate estimation. This work has provided insight into the development of methods for calculating the view factor during radiant energy exchange between 32 combinations of triangular geometries with a common edge.

Twelve examples with various aspect ratios were calculated for each geometry, using AS, MSR, SGS, and BCR. From the eight basic geometries, the view factor was obtained for 24 other triangular geometries using the summation rule. In all cases, identical fit values were obtained for MSR and SGS with respect to AS, while BCR showed the best correlation in all cases examined. In all the cases evaluated, the BCR showed the best fits, with an error of $\pm 6\%$ in more than 90% of the samples, while the MSR showed an average dispersion of $\pm 6\%$ in 65% of the data.

Given the practical nature of the contribution and the reasonable values of the fits obtained, the proposal constitutes a suitable tool for application in thermal engineering and related practices requiring thermal radiation calculations.

Very importantly, in modern engineering, mesh generators rarely use rectangles or squares (unless the overall geometry is a perfect cube), with triangular elements being the most commonly used elements.

Given the lack of similar precedents in the literature, the proposed analytical solutions reinforce the scientific and practical value of this research and can be incorporated into the currently available catalogs for calculating the view factor.

Acknowledgment

The authors acknowledge the help provided by Dr. M. Zeki Yilmazoglu, from the Department of Mechanical Engineering, Gazi University, Turkey.

Nomenclature

- a Length of the surface A_1 , m
- A_1 Leaving surface, m^2
- A_2 Reaching surface, m^2
- D Width of the surfaces A_1 and A_2 , m
- $D_{\%}$ percentage of deviation, defined in Eq. (26)
- L Length of the surface A_1 , m
- r Distance between surfaces A_1 and A_2 , m
- R Constant, defined in Eq. (3)
- x displacement at surface A_2 , defined in Fig. 4
- W Length of the surface A_2 , m
- X Constant, defined in Eq. (3)
- Y Constant, defined in Eq. (3)

- θ Angle between surfaces A_1 and A_2
- θ_1 Angle between the normal and surface A_1
- θ_2 Angle between the normal and surface A_2
- φ Bretzhtsov cross roots

Conflict of Interest Statement

The authors declare that there is no conflict of interest in the study.

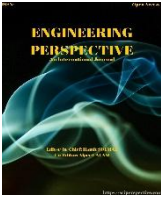
CRediT Author Statement

Yanan Camaraza-Medina: Conceptualization, Data curation, Formal analysis, Investigation, Supervision, Validation, Writing-original draft, Writing - review & editing **Abel Hernandez-Guerrero:** Supervision, Validation, Writing - review & editing **Jose L Luviano-Ortiz:** Formal analysis, Writing - review & editing

References

1. Camaraza-Medina, Y. (2021). Methods for the determination of the heat transfer coefficient in air cooled condenser used at biomass power plants. *International Journal of Heat and Technology*, 39 (5), 1443-1450. <https://doi.org/10.18280/ijht.390505>
2. Nassar, Y. F. (2020). Analytical-numerical computation of view factor for several arrangements of two rectangular surfaces with non-common edge. *International Journal of Heat and Mass Transfer*, 159, 120130. <https://doi.org/10.1016/j.ijheatmasstransfer.2020.120130>
3. Howell, J. R., & Mengüç, M. P. (2011). Radiative transfer configuration factor catalog: A listing of relations for common geometries. *Journal of Quantitative Spectroscopy and Radiative Transfer*, 112, 910-912. <https://doi.org/10.1016/j.jqsrt.2010.10.002>
4. Modest, F. M., & Mazumder, S. (2021). *Radiative heat transfer*, 4th ed., Academic Press,
5. Camaraza-Medina, Y., Hernandez-Guerrero, A., & Luviano-Ortiz, J. L. (2022). Analytical view factor solution for radiant heat transfer between two arbitrary rectangular surfaces. *Journal of Thermal Analysis and Calorimetry*, 147 (24), 14999–15016. <https://doi.org/10.1007/s10973-022-11646-4>
6. Howell, J. R. (2023). *A catalog of radiation heat transfer configuration factors*. 7th ed., MIT Press.
7. Narayanaswamy, A. (2015). An analytic expression for radiation view factor between two arbitrarily oriented planar polygons. *International Journal of Heat and Mass Transfer*, 91, 841-847. <https://doi.org/10.1016/j.ijheatmasstransfer.2015.07.131>
8. Narayanaswamy, A., & Meyappan, P. (2015). An analytic expression for radiation view factors between two planar triangles with arbitrary orientations. *Advances in Computational Heat Transfer*, 6, 2015-2019 <https://doi.org/10.1615/ICHMT.2015.IntSympAdvComputHeatTransf>
9. Gupta, M. K., Bumtariya, K. J., Shukla, H. A., Patel, P., & Khan, Z. (2017). Methods for evaluation of radiation view factor: a review. *Material Today Proceeding*, 4 (2), 1236-1243. <https://doi.org/10.1016/j.matpr.2017.01.143>
10. Howell, J. R., Mengüç, J. P., Daun, K., & Siegel, R. (2020). *Thermal Radiation Heat Transfer*, 7thed., CRC Press.
11. Ehlert, J. R., & Smith, T. F. (1993). View factors for perpendicular and parallel rectangular plates. *Journal of Thermophysics and Heat Transfer*, 7 (1), 173-175. <https://doi.org/10.2514/3.11587>
12. Yi, X. J., Zhong, L. Y., Wang, T. B., Liu, W. X., Zhang, D. J., Yu, T. B., & Liu, N. H. (2019). Near-field radiative heat transfer between hyperbolic metasurfaces based on black phosphorus. *The European Physical Journal B*, 92, e217. <https://doi.org/10.1140/epjb/e2019-100274-y>
13. Zhou, Y., Duan, R., Zhu, X., Wu, J., Ma, J., Li, X., Wang, Q. (2020). An improved model to calculate radiative heat transfer in hot combustion gases. *Combustion Theory and Modelling*, 24 (5), 829-851. <https://doi.org/10.1080/13647830.2020.1769866>
14. Reddy, R. S., Arepally, D., & Datta, A. K. (2023). View factor computation and radiation energy analysis in baking oven with obstructions: Analytical and numerical method. *Journal of Food Process Engineering*, 46 (3), 4270. <https://doi.org/10.1111/jfpe.14270>
15. Dam, Q.T., Haidar, F., Mama, N., & Chennapalli, S. J. (2024). Modeling and simulation of an Internal Combustion Engine using Hydrogen: A MATLAB implementation approach. *Engineering Perspective*, 4 (3), 108-118. <http://dx.doi.org/10.29228/eng.pers.76219>
16. Krishnaprakas, C. K. (1997). View factor between inclined rectangles. *Journal of Thermophysics and Heat Transfer*, 11 (3), 480-481. <https://doi.org/10.2514/2.6267>
17. Sauer, H. J. (1974). Configuration factors for radiant energy interchange with triangular areas. *ASHRAE Transactions*, 80 (2), 268-279.
18. Camaraza-Medina, Y., Hernandez-Guerrero, A., & Luviano-Ortiz, J. L. (2023). View factor for radiative heat transfer calculations between triangular geometries with common edge. *Journal of Thermal Analysis and Calorimetry*, 148 (10), 4523–4539. <https://doi.org/10.1007/s10973-023-11975-y>
19. Camaraza-Medina, Y. (2023). Polynomial cross-roots application for the exchange of radiant energy between two triangular geometries. *Ingenius, Revista de Ciencia y Tecnología*, 30, 29-41. <https://doi.org/10.17163/ings.n30.2023.03>
20. Thyageswaran, S. (2022). Simpler view factor calculations for mutually perpendicular rectangles. *Journal of Quantitative Spectroscopy and Radiative Transfer*, 283, 108151. <https://doi.org/10.1016/j.jqsrt.2022.108151>
21. Boeke, W., & Wall, L. (1976). Radiative exchange factors in rectangular spaces for the determination of mean radiant temperatures. *Building Services Engineer*, 43, 244-253.
22. Cabeza-Lainez, J. (2023). A New Principle for Building Simulation of Radiative Heat Transfer in the Presence of Spherical Surfaces. *Buildings*, 13 (6), 1447. <https://doi.org/10.3390/buildings13061447>
23. Cabeza-Lainez, J. (2024). New Geometric Theorems Derived from Integral Equations Applied to Radiative Transfer in Spherical Sectors and Circular Segments. *Mathematics*, 12 (18), 2875. <https://doi.org/10.3390/math12182875>
24. Lakhi, M., & Safavinejad, A. (2021). Numerical investigation of combined force convective–radiative heat transfer in a horizontal channel with lattice Boltzmann method. *Journal of Thermal Analysis and Calorimetry*, 146, 1911-1922. <https://doi.org/10.1007/s10973-020-10136-9>
25. Gomez-Gil, A., & Cabeza-Lainez, J. (2024). Ferrer House at Rocafort, an Early Case of Brise-Soleil's Design for the Mediterranean Region in Valencia. *Designs*, 8 (5), 96. <https://doi.org/10.3390/designs8050096>
26. Sönmez, F. F., Ziar, H., Isabella, O., & Zeman, M. (2019). Fast and accurate ray-casting-based view factor estimation method for complex geometries. *Solar Energy Materials and Solar Cells*, 200, 109934. <https://doi.org/10.1016/j.solmat.2019.109934>
27. Biehs, S. A., Messina, R., Venkataram, P. S., Rodriguez, A. W., Cuevas, J. C., & Ben-Abdallah, P. (2021). Near-field radiative heat

- transfer in many-body systems. *Reviews of Modern Physics*, 93 (2), 025009. <https://doi.org/10.1103/RevModPhys.93.025009>
28. Camaraza-Medina, Y., Hernandez-Guerrero, A., Luviano-Ortiz, J.L. (2024). Contour integration for the view factor calculation between two rectangular surfaces. *Heat Transfer*, 53 (1), 225-243. <https://doi.org/10.1002/htj.22950>
29. Camaraza-Medina, Y., Hernandez-Guerrero, A., Luviano-Ortiz, J.L. (2024). Contour integration for the exchange of radiant energy between diffuse rectangular geometries. *Thermal Science and Engineering Progress*, 47, 102289. <https://doi.org/10.1016/j.tsep.2023.102289>
30. Hamilton, D. C., & Morgan, M. R. (1952). Radiant-interchange configuration factors. NAAS TN 2836.
31. Feingold, A. (1966). Radiant-interchange configuration factors between various selected plane surfaces. *Proceedings of the Royal Society of London*, 292, 51-60. <https://doi.org/10.1098/rspa.1966.0118>
32. DeSutter, J., Tang, L., & Francoeur, M. (2019). A near-field radiative heat transfer device. *Nature Nanotechnology*, 14 (8), 751-755. <https://doi.org/10.1038/s41565-019-0483-1>
33. Yarahmadi, M., Robert Mahan, J., & McFall, K. (2020). Artificial neural networks in radiation heat transfer analysis. *ASME Journal of Heat Transfer*, 142 (9), 092801. <https://doi.org/10.1115/1.4047052>



Thermal Model of Lithium-Ion Batteries for Hybrid Electric Vehicles

Racha Bayzou^{1*} , Adrien Soloy¹ , Thomas Bartoli¹ , Fatima Haidar¹ 

¹ Capgemini engineering, Ile de France, Division APA, 12 rue de la Verrerie, 92190 Meudon, France

ABSTRACT

This study aims to develop a comprehensive model using MATLAB Simulink software to characterize the thermal behavior of lithium-ion battery packs. The model operates at both the cell and pack levels, enabling the determination of individual cell temperatures and the heat generated by Joule effect, influenced by chemical reactions during charge and discharge cycles. At the pack level, the model assesses temperature variations among cells by simulating heat transfers between them. Detailed principles, equations, and underlying hypotheses for constructing the model are elucidated.

Through simulations, the model's performance is evaluated against experimental data. Remarkably, strong correlations are observed in temperature variations of 18650 LFP cylindrical cells within a battery pack, not only under standard charge and discharge conditions but also when subjected to a standardized WLTC (Worldwide harmonized Light vehicles Test Cycle) driving cycle. This indicates the robustness and accuracy of the chosen methodology in model development. The study's findings hold significant implications for optimizing battery pack design and advancing thermal management strategies in various applications such as electric vehicles and renewable energy systems.

Future research endeavors may involve further refinement of the model and exploration of additional facets of battery behavior to enhance its predictive capabilities and applicability across diverse scenarios.

Keywords: Hybrid Electric Vehicles (HEV); Li-ion; MATLAB-Simulink; Thermal model.

History

Received: 14.05.2024

Revised : 05.02.2025

Accepted: 03.05.2025

Author Contacts : racha.bayzou@capgemini.com* adrien.soloy@capgemini.com thomas.bartoli@capgemini.com fatima.haidar@capgemini.com

Cite this paper: Bayzou, R., Soloy, A., Bartoli, T., Haidar, F. (2025). Thermal model of Lithium-ion batteries for hybrid electric vehicles. Engineering Perspective, 5 (2), 60-67. <http://dx.doi.org/10.29228/eng.pers.76492>

*Corresponding Author

1. Introduction

Environmental worries regarding the exhaustion of traditional energy resources have grown on a global scale in recent decades. The significant rise in atmospheric pollution and the greenhouse effect can be largely attributed to the extensive reliance on fossil fuels, particularly in the context of automotive usage [1]. Batteries, particularly Li-ion, have emerged as a solution to replace fossil fuels. While initially costly and offering limited range, Li-ion batteries have undergone substantial advancements in recent years, reducing the cost per kilowatt-hour (kWh) from \$1,000 in 2010 to approximately \$273 in 2016, with forecasts projecting further reductions to around \$109 per kWh by 2025 and \$73 per kWh [2-3]. Despite continuous improvements and current energy densities of around 250 Wh/kg, Li-ion batteries still exhibit certain drawbacks [4]. One significant issue is the reliance on metals like lithium and cobalt, which are used in cathode materials such as Lithium Cobalt Oxide (LCO), Nickel Manganese Cobalt (NMC), or Nickel Cobalt Aluminum (NCA) [5]. These materials pose economic challenges

due to their uneven geographic distribution and environmental concerns regarding their extraction, which has a substantial environmental impact [6].

Another limitation concerns cell safety in various scenarios such as crushing, puncturing, extreme temperatures, or thermal runaway. Therefore, effective temperature management within the battery pack is crucial. Car manufacturers achieve this through a battery management system (BMS), which incorporates multiple functions like monitoring current, voltage, resistance, state of charge (SOC), state of health (SOH), and thermal conditions within the cells. The BMS communicates with the vehicle's calculator, enabling the regulation of power consumption, the control of the cooling system, and the ability to raise alerts in case of potential dangers.

To address these challenges, the utilization of models to predict the thermal behavior of batteries is a critical concern for both cell and vehicle manufacturers [7-8]. These models help forecast temperature distribution within the cell based on its morphology (e.g., pouch cell, cylindrical, or prismatic cell) and material

composition. They also help to predict the cooling requirements to keep the battery pack in ideal temperature conditions. The cooling demands are influenced by various factors, including the number of cells, their configuration within the battery pack, and the thermal power generated. Proper sizing of these components allows for risk mitigation while optimizing the financial investments required for the development of this strategy. In this context, a straightforward method for predicting the thermal behavior of cells and battery packs is presented in this work. The aim of this study is to create a battery model allowing the simulation of the thermal behavior of cells contained in a Li-ion battery pack and of the battery pack itself. This model is then to be integrated into a complete battery model to be able to study the behavior of Li-ion batteries used in hybrid electric vehicles. The work described here will not detail the integration of the whole battery model but will rather focus on the method used to develop the battery thermal model itself.

2. Model choice consideration

Battery modeling has become essential in the automotive industry for designing high performance hybrid and electric vehicles. By understanding and predicting battery behavior, modeling ensures optimal and safe usage, maximizing performance, lifespan, and efficiency. It enables the development of effective battery management strategies and optimization of design for reliable electric vehicle operation [9]. Depending on the application, battery models vary in complexity, depending on the environment and parameters being analysed. Various types of battery models exist based on the parameters and properties under study. The main battery models found in the literature are: Electrochemical, electrical and thermal [10-11].

Starting the development of a suitable Li-ion battery thermal model, aligned with the predefined technical requirements, required the careful selection of a method. This selection process considered various criteria, including computational cost, simulation time, realism in relation to the physical system, and the complexity of method development and calculations. The following approaches were compared:

- The analytical resolution method for the 2D transient heat equation, employing the Fourier method and separation of variables (transient and steady state). This method incorporates the boundary and initial conditions of the system.

- The finite difference numerical resolution method.
- The finite element numerical resolution method.
- The thermal quadrupole method.
- The series thermal resistance method.
- The matrix method

After an exhaustive bibliographical study analyzing the modeling methods and a comprehensive assessment of different criteria, the matrix method, which is an adaptation of the thermal resistance method, was chosen. This method is not only computationally efficient and straight forward to implement, but it also aligns well with Simulink's matrix calculus constraints for the determination of temperatures and thermal powers.

In the upcoming section, the approach and principles behind the thermal modeling of a cell are detailed, along with the corresponding functionalities that have been developed.

2.1. Thermal model of battery cell

• Principle

Before starting the development of the Simulink model, it was imperative to delineate the assorted requirements and technical functionalities that needed to be addressed. Specifically, the Simulink model should allow:

- Compute the temperature of each layer of materials contained within every cell.
- Calculate the heat generated through Joule heating and chemical reactions within the volume of each layer in the cell.
- Facilitate the adjustment of physical parameters via a MATLAB script.
- Enable the modification of the cell dimensions.
- Evaluate thermal exchanges between cells.
- Dynamically compute the heat generated and temperature variations in each layer of every cell.

• Method

Initially, various hypotheses and approximations of the physical phenomena of the model were established to simplify the design and validation of the model in Simulink. The case of cylindrical cells was chosen.

The surface temperature is considered homogeneous, the median plane of the cell is mainly studied. Indeed, it is in this plane that the surface temperature is the highest and where temperatures are generally measured using a sensor. In addition, materials through which the conductive flow pass are considered anisotropic. As a result, the conductive flow is oriented in the radial direction (or x , as shown in Figure 1) within cylindrical cells. In addition, contact resistance is neglected. In the center of the cell, the flow is nil because the system under study is symmetrical around its axis. At the outer surface of the cell, the discharged conductive flow is equal to the convective flow. In addition, the initial temperature of the cell is considered the same as that of the fluid in the environment. Eq. (1) and Figure 1 describes and illustrates the boundary conditions of the cell system.

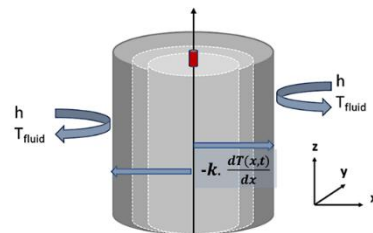


Figure 1. Schematic description of the boundary conditions of the cell.

The development process primarily involved identifying the various stages and requirements of the model. Initial steps included an in-depth examination of diverse thermal modeling techniques applied to Li-ion battery cells, scrutinizing the approach, approximations, and conditions employed. Subsequently, intermediate tests were conducted to validate each functionality of the model as it progressed.

$$\begin{aligned}
& \frac{\partial^2 T(r, t)}{\partial r^2} + r \cdot \frac{\partial T(r, z, t)}{\partial r} - \frac{1}{\alpha} \cdot T(r, t) = -\frac{q}{\lambda} \\
& \text{For } r = 0, \quad -\lambda \frac{dT(r, p)}{dr} = 0 \\
& \text{For } r = R, \quad -\lambda \frac{dT(r, t)}{dr} = h \cdot (T(r, t) - T_{fluid}) \\
& \text{For } t = 0 \text{ s}, \quad T(r, 0) = T_{fluid}
\end{aligned} \tag{1}$$

Table 1. Input and output parameters used for the model.

Input parameters	
Geometric cell properties	
Length	(mm)
Radius	(mm)
Thickness	(mm)
Interlayer exchange area	(mm ²)
Thermophysical properties	
Thermal conductivity	(W/(m.K))
Density	(kg/m ³)
Specific heat capacity	(J/(kg.K))
Boundary conditions properties	
Convective transfer coefficient	(W/(m ² .K))
Fluid temperature	(°C)
Convective flux	(W)
Fluid temperature T _{ext}	(°C)
Output parameters	
Surface and core temperatures	(°C)
Layer temperatures	(°C)
Joule effect	(W)
Entropy variation	(W)

These tests played a crucial role in refining and enhancing different versions of the Simulink code in comparison to results obtained from analogous cell models. This iterative process allowed for course correction and improvement, aiding in the selection of an optimal compromise between operational speed and model realism.

Input parameters for the model encompassed geometric, thermophysical data, and boundary conditions such as convective flow, convective transfer coefficient, and outlet temperature. Output parameters included temperatures (core, surface, layers) and various powers generated by the model, such as Joule effect and entropy variation. These parameters are succinctly presented in Table 1.

• Developed

After studying and selecting the most suitable method, it became possible to develop various functionalities that meet the initial requirements of the model. Indeed, the Simulink model performs the following:

Calculation of the thermal power generated by current dissipation in the cell through Joule effect and entropy variation is achieved by a Simulink subsystem. This subsystem takes the current of each cell, squares it, and multiplies it by the internal resistance of each cell. The thermal power generated by entropy variation during the electrochemical reaction due to charging or discharging is calculated based on the current of each cell, its open-circuit voltage, and temperature.

Calculation of the fraction of power generated within the volume

of each layer. A block takes the total power generated for a cell and multiplies it by a fraction of the volume associated with each layer. This volumetric fraction depends on the thickness of each layer.

Calculation of the temperature of each layer in each cell. It is performed by a MATLAB function integrated into the Simulink code. This function calculates the temperature of the first layer of the cell based on the initial temperature, the cell, the heat generated by the Joule effect, and the exchange surface between the cells. A balance of exchanged flows with the next layer is then conducted. Incoming and outgoing conductive fluxes are considered for internal layers.

Modification of the thermophysical and geometric parameters of the model through the execution of an initialization script. A script corresponding to the chosen cell technology is executed in advance on MATLAB to load different thermophysical and geometric parameters of the cell in the Simulink model. The ability to modify parameters in the script allows us to adapt easily the simulation to various cell technologies.

Calculation of thermal exchanges between cells. It is performed by a MATLAB function that retrieves the calculated temperature in different layers of a cell to extend the calculation to all cells constituting a battery pack.

The sequence of execution of various functionalities and the calculation steps of different quantities in the model are depicted in Figure 2. The main functionalities of the Simulink thermal model that has been developed are presented in Figure 3.

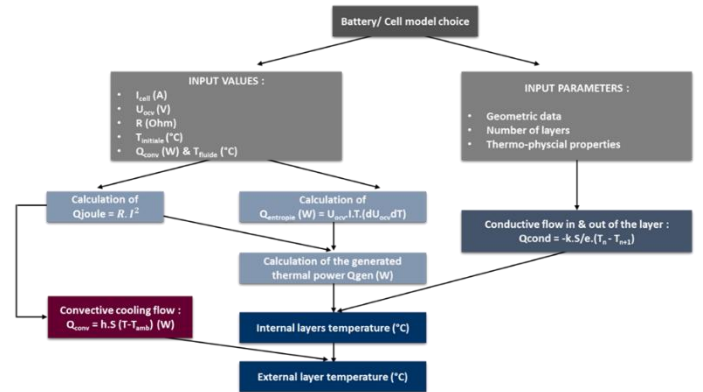


Figure 2. Calculation steps followed by the thermal model developed in Simulink.

It is worth noting that the current model includes certain limitations, such as the assumption of uniform material properties and steady-state operating conditions.

2.2. Thermal model of pack battery

• Pack model based on the cell model

The three-layer model describing cell behavior is used to build a comprehensive battery pack model. This section will present the model development process, outline the various assumptions and approximations made, and detail the results obtained.

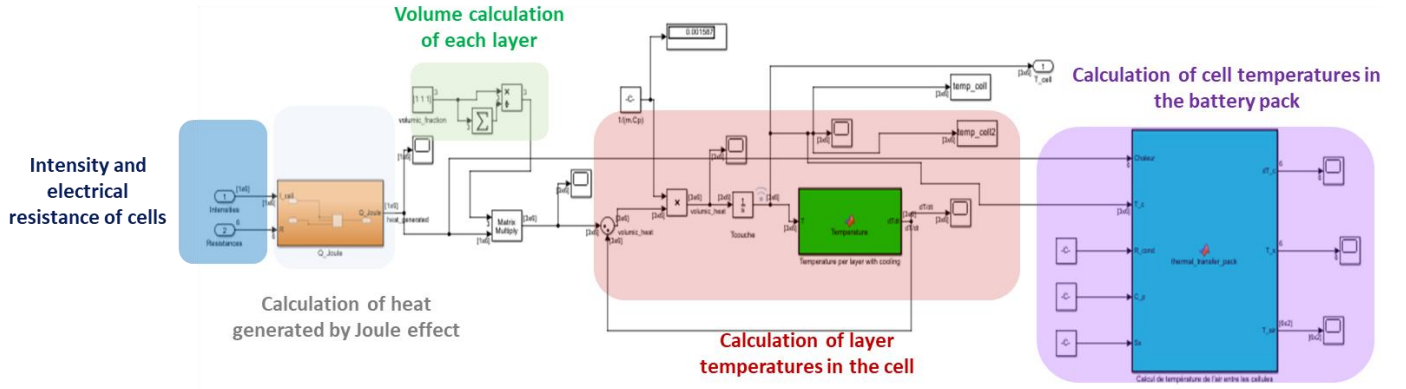


Figure 3. Simulink models and related features

The objective of the model is to simulate heat transfers among the cells constituting a battery pack. As for the Simulink-developed cell model, several assumptions, and approximations regarding the physical phenomena of the model were established to streamline the design and validation of the thermal model for a battery pack:

Cells are assumed to be spaced apart, allowing for fluid flow between them.

Radiative heat losses are disregarded in comparison to those transferred by convection inside the battery pack. Indeed, radiant energy constitutes only a minimal portion of the energy exchanged during cell charging and discharging.

The conductive flow through the foils (metal lamellae) connecting individual cells in series within the battery pack is also neglected.

Incoming air is blown at room temperature, and its flow is evenly distributed among the cells. Heat propagation between cells occurs from left to right and from bottom to top, following the air flow. Consequently, the convective exchange coefficient remains consistent throughout the battery pack.

Heat transfer between cells was analyzed in various scenarios based on each cell's position within the battery pack. These scenarios include:

The cell in the lower-left corner is at the temperature of the incoming air at the beginning of the simulation. The temperatures of other cells are then calculated based on the temperature of the air, the airflow, and the temperature of this first cell.

Cells in the first lower row transfer heat through convection and then conduct in the air to the adjacent cells in the upper row. Because of the proximity of the cells and the low airflow, the convective transfer is neglected.

Cells in the first column on the left transfer heat through convection to the neighboring cells in the next column on the right.

Various convective heat exchange patterns between cells were considered [12]. Cells are arranged in rows in parallel and series. The model extracts the temperature of the first layer calculated by the cell calculation block as a vector. This vector is then put into the cell temperature calculation block to initialize the core, surface, and air temperatures of the cells. Groups of surface, core, and air temperatures are stored in matrices, which size is determined by the number of cells in parallel and in series. This number is set in the initialization script of the simulation. Cells in the vertical direction "i" are in series, while cells in the horizontal direction "j" are in parallel. The temperature calculation method is directly inspired from the finite difference method applied to a transient two-

dimensional thermal problem.

Heat transfers from cells located in two adjacent vertical rows are described by Eq. (2):

$$h_{conv} \cdot S \cdot (T_s(i, j) - T_{air}(i, j - 1)) - \lambda \cdot h_{conv} \cdot S \cdot (T_s(i, j) - T_{air}(i, j)) - \frac{\lambda}{e} \cdot (T_c(i, j) - T_s(i, j)) = 0 \quad (2)$$

Where S denotes the exchange surface between the cell and the ambient fluid (m^2), e is the cell thickness, h_{conv} is the convective exchange coefficient between the cell surface and the ambient air ($W/(m^2.K)$), λ is the thermal conductivity of the cell ($W/(m.K)$), $T_s(i, j)$ is the temperature of the surface of the cell located on the row i and column j , $T_{air}(i, j-1)$ denotes the temperature of the air at the row i and column $(j-1)$, $T_{air}(i, j)$ is the temperature of the air at the row i and column j and $T_c(i, j)$ is the temperature of the core of the cell located at the row i and column j .

Figure 4 illustrates the equivalent circuit used to model the horizontal heat transfers between two adjacent cells. It represents the calculus of the temperature of the cell located on the right adjacent vertical row.

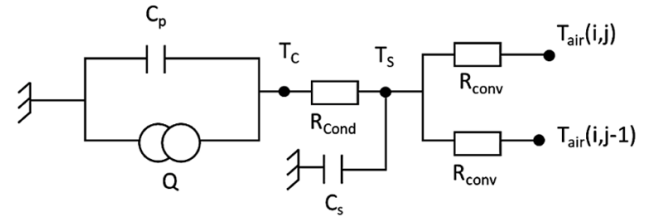


Figure 4. Equivalent circuit represents the horizontal heat transfer between two adjacent cells.

For cells located in the first vertical row, the exchanged thermal power balance between two consecutive cells is expressed by Eq. (3).

For $j = 1$:

$$\dot{m}_{air} \cdot C_{p,air} \cdot (T_{air}(i+1, j) - T_{air}(i, j)) = h_{conv} \cdot S \cdot (T_s(i, j) - T_{air}(i, j)) \quad (3)$$

Where \dot{m}_{air} denotes the air mass flow rate between the cells (kg/s), $C_{p,air}$ represents the air calorific capacity ($J/(kg.K)$), $T_{air}(i+1, j)$ is the air temperature at the row $i+1$ and column j , $T_{air}(i, j)$ is the air

temperature at the row i and column j , h_{conv} represents the convective exchange coefficient between the cell surface and the ambient air ($W/(m^2.K)$), S is the exchange surface between the cell and the ambient fluid (m^2), $T_s(i,j)$ denotes the temperature of the surface of the cell located on the row i and column j and $T_{air}(i,j)$ is the temperature of the air at the row i and column j .

For cells located in the last vertical row, the exchanged thermal power balance between two consecutive cells is expressed by Eq. (4) :

$$\begin{aligned} \text{For } j = n_p: \\ \dot{m}_{air} \cdot Cp_{air} \cdot (T_{air}(i+1, j) - T_{air}(i, j)) \\ = h_{conv} \cdot S \cdot (T_s(i, j-1) - T_{air}(i, j)) \end{aligned} \quad (4)$$

Where n_p denotes the number of cells in parallel, \dot{m}_{air} is the air mass flow rate between the cells (kg/s), Cp_{air} is the air calorific capacity ($J/(kg.K)$), $T_{air}(i+1, j)$ denotes the air temperature at the row $i+1$ and column j , $T_{air}(i, j)$ is the air temperature at the row i and column j , h_{conv} present the convective exchange coefficient between the cell surface and the ambient air ($W/(m^2.K)$), S is the exchange surface between the cell and the ambient fluid (m^2), $T_s(i, j-1)$ is the temperature of the surface of the cell located on the row i and column $j-1$ and $T_{air}(i, j)$ is the temperature of the air at the row i and column j .

For cells located between the first and the last vertical row, the exchanged thermal power balance between two consecutive cells is expressed by Eq. (5).

$$\begin{aligned} \text{For } j \in (2, n_p - 1): \\ \dot{m}_{air} \cdot Cp_{air} \cdot (T_{air}(i+1, j) - T_{air}(i, j)) \\ = h_{conv} \cdot S \cdot (T_s(i, j-1) - T_{air}(i, j)) \\ + h_{conv} \cdot S \cdot (T_s(i, j) - T_{air}(i, j)) \end{aligned} \quad (5)$$

Where n_p denotes the number of cells in parallel, \dot{m}_{air} is the air mass flow rate between the cells (kg/s), Cp_{air} is the air calorific capacity ($J/(kg.K)$), $T_{air}(i+1, j)$ present the air temperature at the row $i+1$ and column j , $T_{air}(i, j)$ is the air temperature at the row i and column j , h_{conv} correspond to the convective exchange coefficient between the cell surface and the ambient air ($W/(m^2.K)$), S is the exchange surface between the cell and the ambient fluid (m^2), $T_s(i, j)$ present the temperature of the surface of the cell located on the row i and column j and $T_{air}(i, j)$ is the temperature of the air at the row i and column j .

Figure 5 illustrates the process for computing the temperature of cells in the first vertical row. The arrangement of cells and the different heat transfers within the battery pack are illustrated in Figure 6.

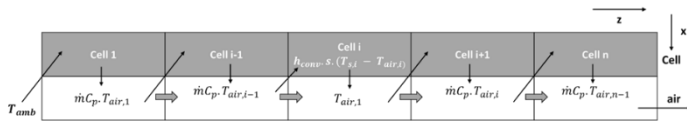


Figure 5. Representation of the heat transfers distribution between the cells of the first vertical row.

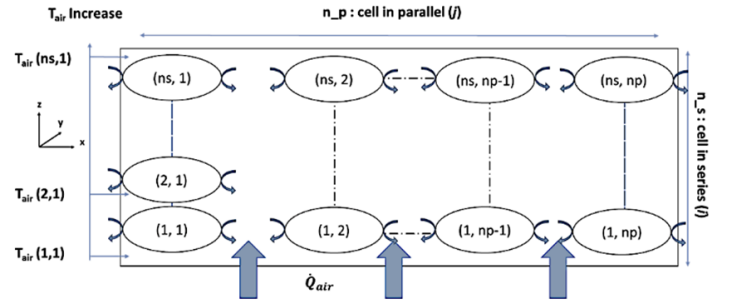


Figure 6. Representation of the heat transfers distribution between the cells of a battery pack.

3. Results and discussion

• Simulation results at the cell level:

Tests were first performed at the cell level to check the relevance of the model using characteristics of cells often used in HEV batteries. The parameters of the cylindrical cell chosen for the tests are detailed in Table 2. A comparison was performed between the results obtained experimentally in D. Allart's thesis work [13] and those derived from the Simulink model for charge and discharge currents, presented in the form of analogous squared signals at the model's input. The results are presented in Figure 7. The profile of the surface and core temperature curve for the Simulink model closely resembles that of Allart's thesis [13]. In our model, the surface temperature reaches its maximum at 42 °C, while a value of 43 °C is reported in the thesis. This difference can be attributed to the fact that the heat capacity of the cell is estimated to be 3 layers in the Simulink model, whereas it is estimated for only one layer in the thesis model. As a result, the mass of each layer differs slightly from that used for the cell in the thesis. Another potential explanation for this temperature difference could be the overestimation of the convection exchange surface between the cell and the ambient air in our model compared to the value provided in the thesis.

Another test was performed with currents obtained from a WLTC driving cycle used as input. The aim was to check if the values of temperature increases obtained for one cell were consistent with the literature [12, 14]. The WLTC on which tests are based is presented in Figure 9.

Table 2. Parameters of an 18650 LFP cylindrical cell used for validation tests.

Geometrical parameters	
Number of layers	3
Thickness (mm)	0.0045
Radius (m)	0.009
Mass (kg)	0.0128
Electrical parameters	
Current intensity (A)	3.6
Internal resistance (Ohm)	0.004
Thermophysical parameters	
Thermal conductivity (W/m.K)	0.65
Heat capacity (J/kg/K)	1280
Convective transfer coefficient ($m^2.K$)	20
Fluid temperature (°C)	20

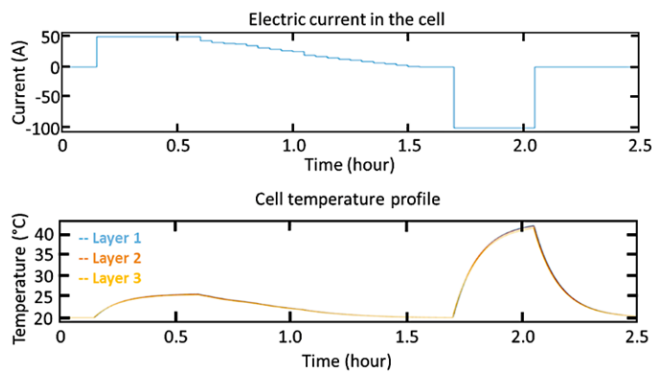


Figure 7. Results obtained by the Simulink model for a 18650 LFP cylindrical cell.

Throughout the vehicle's acceleration phases, the power generated and supplied by the battery rises as the battery discharges. Similarly, the power generated and recovered by the battery increases as its current load escalates during deceleration phases. The curves depicted in Figure 9 illustrate the temperature increase in a cylindrical cell and the fluctuations in current and generated power corresponding to the WLTC cycle used and illustrated in Figure 8.

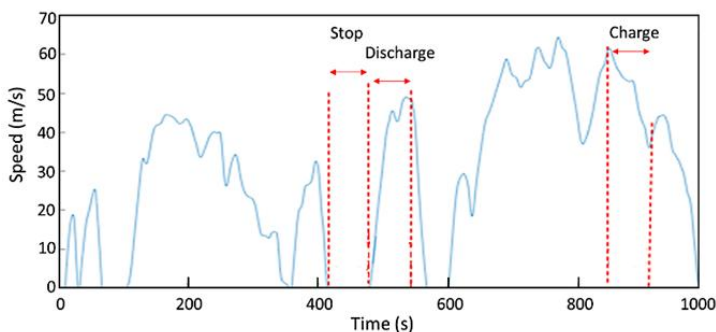


Figure 8. Speed curve of a 1000 second WLTC driving cycle.

The temperature increase remains below 3 °C for a convection coefficient of 10 W/(m²·K) and a power of up to 40 W per cell. These temperature rises are consistent with experimental data documented in the literature for this cell type under similar power and test conditions [13]. Furthermore, it is observed that during vehicle acceleration or deceleration, the cell internal temperature increases because of the current flowing through the layers, heating up the cells. When the vehicle is stopped, with no power required and generated by the battery, the cell temperature decreases due to convection at its surface. The results obtained are consistent and realistic, capturing the physical phenomena experienced by the cells.

The results obtained from the previous test allowed us to visualize the one-dimensional temperature evolution within the various layers of the cell, as shown in Figure 10. The temperature of the first layer, corresponding to the core of the cell, is higher than that of the other layers. This is because the central region of the cell retains heat for a longer duration, requiring successive transfers between the layers before dissipating the accumulated heat through convective flow to the outer layers.

Another test was to compare the results from the Simulink model with those of another model using the "Simscape" library, which incorporates pre-implemented physical and thermal computational functions.

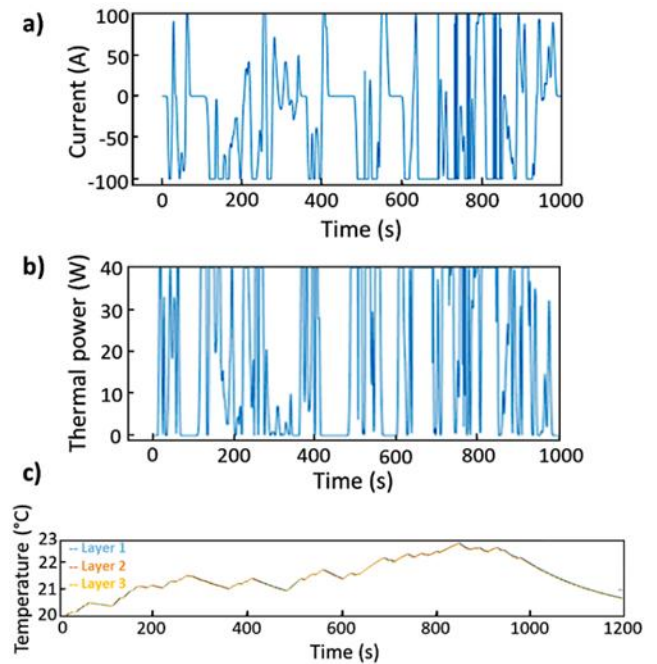


Figure 9. Simulink model results for a WLTC cycle: electric current in the cell (a), thermal power generated in the cell (b) and cell temperature profile (c).

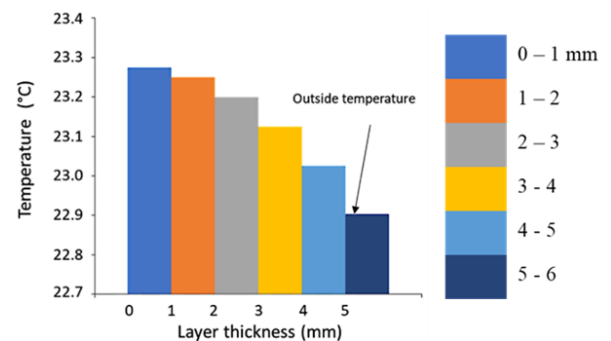


Figure 10. Cell temperature evolution within a cell.

The input conditions and parameters for both models were identical. The objective of this test was to observe the impact of parameters and equations used in the Simulink model to achieve similar results with the Simscape model. The test was conducted at an ambient temperature of 0 °C and a convective flux of 15 W/(m²·K). Initial physical parameters used in both models were the same based on values provided in Table 2. The temperature profiles obtained for the two models are depicted in Figure 11. Similar temperature rises of 2.2 °C and 1.7 °C were observed for the Simulink and the Simscape model of a three-layer cell respectively. The temperature difference between the two models may be attributed to the distinct calculation method used for the convective heat dissipation. The approximations made in the Simulink model, as well as the unknown approximations in the Simscape model, could also account for this temperature difference. The absence of accessible details regarding the approximations made by the Simscape model prevents conclusive remarks on this matter. Both models had identical input conditions, currents, and thermophysical parameters for the cell layers. These tests thus provided an alternative means of validating the

coherence and reliability of the Simulink model.

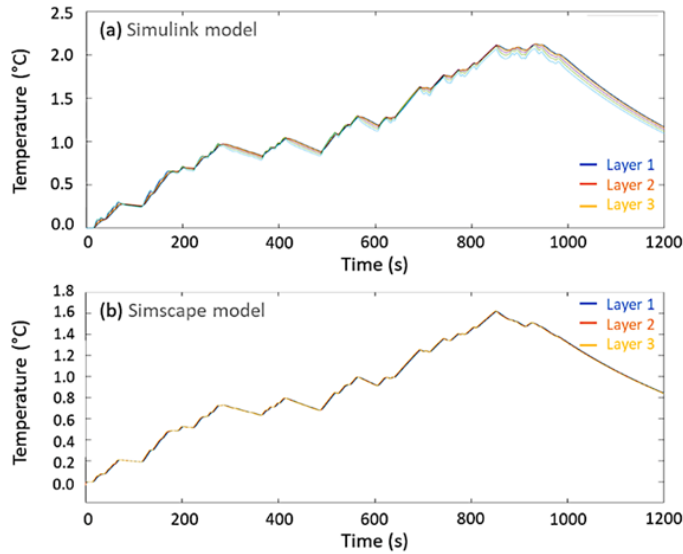


Figure 11. Temperature profiles obtained with the Simulink (a) and the Simscape models (b).

• Simulation results at the battery pack level:

Like for the cell model, validation tests were conducted to ensure the physical coherence of the model's behavior at the battery pack level. These tests primarily focused on examining the core and air temperature profiles of LFP cylindrical cells. The cell temperature values were derived from the temperature calculation carried out for a single cell. Consequently, the core temperature of the initial cell allowed the calculation of the core, surface, and ambient air temperatures for the remaining cells. The parameters used for the validation tests for the battery model are shown in Table 3.

Table 3. Parameters of 18650 LFP cylindrical cell used in the battery pack model for validation tests.

Cell thermophysical parameters	
Number of cells	12
Thermal conductivity (W/m/K)	0.65
Radius (m)	0.009
Mass (kg)	0.0128
Internal resistance (Ohm)	0.004
Air thermophysical parameters	
Air density (kg/m ³)	1.225
Air mass flow (kg/s)	0.001
Heat capacity (J/kg/K)	1004
Convective transfer coefficient (W/m ² .K)	5
Fluid temperature (°C)	20

Figure 13 illustrates the variations in surface and air temperature surrounding the cells in a battery pack comprising four rows in parallel and three rows in series. It can be observed that the air temperature surrounding each cell is marginally lower than the surface temperature of the cells. This discrepancy is attributed to the transient mode during which the dissipated heat flow relies on a temperature difference, resulting in the cell surface being warmer than the air. Consequently, four distinct groups of air temperature, corresponding to the heating of

the air between the four rows of cells in series, can be identified. The model effectively accounts for the heating of the air along the parallel rows. Conversely, cells situated farthest from the air inlet exhibit the highest temperatures, with the air temperature in the first row being at room temperature (20 °C). These outcomes are aligned with physical realities and are consistent with similar experimental models documented in the literature [12, 14-15], thus reflecting that the model is functional.

4. Conclusions

In this paper, the method used to conceive an accurate lithium-ion battery model is provided. This model comprises a simulation of the heat generated within a single battery cell, each cell being represented by a three-layer stacking, as well as the heat transfers occurring between the cells contained in a battery pack subjected to multiple consecutive charge and discharge cycles. Using heat transfer equations and equivalent circuit models, the thermal behaviour of a battery pack and each of its individual cells is modelled accurately. Simulations were carried out and compared to experimental data available in the literature. The results obtained from the model have shown good correlation with those data. The model built in this work accurately simulates the temperature evolution within an individual cell and the heat transfers in a battery pack. At the cell level, the heat generation modelled was very close to the one illustrated in the literature, both following a single charge-discharge cycle and the different charge-discharge cycles generated by a WLTC standardized driving cycle. The evolution of the temperature of the cell, from the core to the surface, was consistent with experimental observations. The comparison between the Simulink model built in this work and a Simscape model built from pre-implemented physical and thermal computational functions was another proof of the relevancy and accuracy of the model. At the battery pack level, the method heat transfers between the cells, showing consistent heat propagation between the different rows of the pack in series and in parallel. To improve the model further, several works will be carried out in the future such as implementing the failure cases and their consequent thermal runways, considering the thermal losses by radiations, or comparing the simulation results with experimental data for other cell chemistries (NMC, NCA, ...).

An additional validation step involved comparing the results obtained from the Simulink model with those generated by an alternative model built using the Simscape library, which includes pre-configured physical and thermal computation components.

In the end, this model will be implemented in a complete battery simulation platform aiming to accurately model the electrical, thermal, and ageing behavior of a battery.

Acknowledgment

This work was carried out at Altran Prototypes Automobiles (APA) as a part of the Intelligence & Innovation Powertrain (IPWT) project within the Capgemini Engineering Research and Innovation Department. The authors would like to thank Dr. Mohand-Ouyahia BOUSSEKSOU and Thomas Lozac'h for their contributions to the work.

Conflict of Interest Statement

All authors have given approval to the final version of the manuscript. The authors declare that there is no conflict of interest in the study.

CRediT Author Statement

Racha Bayzou: Writing original draft - review & editing & validation.

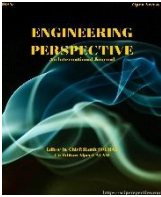
Adrien Soloy: Writing original draft & editing.

Thomas Bartoli: Writing original draft, Data collection; Simulation & validation.







Fatima Haidar: Writing original draft & editing.

References

1. Tsolakakis, A., Bogarra, M., & Herreros, J. (2017). Road vehicle technologies and fuels. In *Environmental Impacts of Road Vehicles: Past, Present and Future* (pp. 1–24). Royal Society of Chemistry. <https://doi.org/10.1039/9781788010221-00001>
2. Ziegler, M. S., & Trancik, J. E. (2021). Re-examining rates of lithium-ion battery technology improvement and cost decline. *Energy & Environmental Science*, 14(4), 1635–1651. <https://doi.org/10.1039/D0EE02681F>
3. Ziegler, M. S., Song, J., & Trancik, J. E. (2021). Determinants of lithium-ion battery technology cost decline. *Energy & Environmental Science*, 14(12), 6074–6091. <https://doi.org/10.1039/D1EE01313K>
4. Łukasz, B., Rybakowska, I., Krakowiak, A., Gregorczyk, M., & Waldman, W. (2023). Lithium batteries safety, wider perspective. *International Journal of Occupational Medicine and Environmental Health*, 36(1), 3–20. <https://doi.org/10.13075/ijomeh.1896.01995>
5. Tran, M. K., DaCosta, A., Mevawalla, A., Panchal, S., & Fowler, M. (2021). Comparative study of equivalent circuit models performance in four common lithium-ion batteries: LFP, NMC, LMO, NCA. *Batteries*, 7(3), 51. <https://doi.org/10.3390/batteries7030051>
6. Lèbre, É., Stringer, M., Svobodova, K., Owen, J. R., Kemp, D., Côte, C., Arratia-Solar, A., & Valenta, R. K. (2020). The social and environmental complexities of extracting energy transition metals. *Nature Communications*, 11, 4823. <https://doi.org/10.1038/s41467-020-18661-9>
7. Soloy, A., Bartoli, T., & Haidar, F. (2023). Modelling and fault diagnosis of lithium-ion battery for electric powertrain. *International Journal of Automotive Science and Technology*, 7(3), 234–247. <https://doi.org/10.30939/ijastech..1295130>
8. Haidar, F., Arora, D., Soloy, A., & Bartoli, T. (2024). Membrane Fuel Cell Degradation and its Counter Strategies: Flooding/drying, Cold Start and Carbon Monoxide Poisoning. *International Journal of Automotive Science and Technology*, 8(1), 96–109. <https://doi.org/10.30939/ijastech..1389241>
9. Blondel, P. (2019). *Estimation de l'état interne d'une batterie lithium-ion à l'aide d'un modèle électrochimique* (Doctoral dissertation, Université de Lorraine). <https://hal.univ-lorraine.fr/tel-02096451>
10. Camas-Náfate, M., Coronado-Mendoza, A., Vega-Gómez, C. J., & Espinosa-Moreno, F. (2022). Modeling and Simulation of a Commercial Lithium-Ion Battery with Charge Cycle Predictions. *Sustainability*, 14(21), 14035. <https://doi.org/10.3390/su142114035>
11. Neverova, N., Wolf, C., Lacey, G., Fridman, L., Chandra, D., Barbello, B., & Taylor, G. (2016). Learning human identity from motion patterns. *IEEE Access*, 4, 1810–1820. <https://doi.org/10.1109/ACCESS.2016.2633260>
12. Y. Jannot, *Theory and practice of thermal metrology*, Nancy, France: LEMTA, University of Lorraine, 2011.
13. Allart, D. (2018). Electrothermal management and modeling of lithium-ion batteries [Doctoral dissertation, University of Caen Normandy].
14. Hémery, C.-V. (2014). Study of thermal phenomena in Li-ion batteries [Doctoral dissertation, Université Grenoble Alpes].
15. Guingane, T. T., Bonkougou, D., Korsaga, E., Simporé, D., Ouedraogo, S., Koalaga, Z., & Zougmore, F. (2023). Evaluation of the performance of lithium-ion accumulators for photovoltaic energy storage. *Energy and Power Engineering*, 15, 517–526. <https://doi.org/10.4236/epe.2023.1512029>



Analysis of the Seismic Vulnerability of a 3-Story Building, Using Typical Structural Sizing Methods Used In Mozambique

Edson da Graça M. Cumbe^{1,2,3} , Ângelo António Pascoal^{2,3} , Valdemar Fulano^{2,3}, Domingos do Rosário N. João¹ , Philemon Niyogakiza¹ , Marc Nshimiyimana¹ , Yenezer Genene Haile¹ 

¹ School of Civil Engineering, Southeast University, Nanjing, 210096, China

² Faculdade de engenharias, arquitetura e planeamento físico, Universidade Wutivi (UniTiva). Mozambique

³ Civil Engineering research team, S-Soiltech Consultoria & Services,Lda, Maputo-Mozambique

ABSTRACT

This study examines the seismic vulnerability of reinforced concrete structures in Mozambique, focusing on the effects of seismic action on structural performance and safety. Due to a lack of seismic-specific regulations in Mozambique, many structures are built without considering earthquake resilience. This research evaluates a reinforced concrete building's response to seismic forces using modal analysis by response spectrum, guided by Eurocode 8 standards. The study begins with an overview of Mozambique's seismic history, geological features, and high-risk regions. It also explores structural design practices in the context of Mozambique's limited regulatory framework (REBAP/RSA). Using Robot Structural Analysis Professional software (2020), we conduct a modal analysis to assess structural behavior beyond the elastic range. Our results indicate maximum displacements of 1.7–1.9 cm and basal shear forces of 1,423–1,282 kN in the X and Y directions, respectively. Floor drift ranges from 0.28 to 0.83, with modal data showing that the first mode, dominated by torsion (86.06%), compromises seismic resilience. The second mode exhibits a translation in the X direction with a modal participation of 96.83%, while the third mode shows a translation in the Y direction with a modal participation of 98.74%. These findings imply the structure lacks adequate torsional resistance, potentially endangering its seismic integrity. Future research should explore model variations and analyze structural responses on different types of soil. Investigating optimized building designs to meet seismic demands in Mozambique and globally could improve safety in earthquake-prone areas.

Keywords: Linear analysis; Seismic analysis; Dynamics analysis.

History

Received: 07.09.2024

Revised : 09.02.2025

Accepted: 08.05.2025

Author Contacts : edsondagracam.c@outlook.com* pascoalangelo4@gmail.com

Cite this paper: Cumbe, E. da G., Pascoal, A. A., Fulano, V., João, D. do R. N., Niyogakiza, P., Siteo, C. M. A., Nshimiyimana M., Haile, Y. G., (2025). Analysis of the Seismic Vulnerability of a 3-Story Building, Using Typical Structural Sizing Methods Used In Mozambique. Engineering Perspective, 5 (2), 68-84. <http://dx.doi.org/10.29228/eng.pers.78239>

*Corresponding Author

1. Introduction

1.1. Background

Mozambique has experienced over 256 earthquakes with magnitudes exceeding 2.5 since 1973. Active seismicity across Mozambique, particularly in the central and northern regions seismic events have caused considerable damage, including the destruction of approximately 300 residential units. The most significant earthquake happened on February 22, 2006, with a magnitude of 7.0 on the Richter's scale, which caused 5 deaths, 28 injuries, destruction of more than 280 houses, and more damages. This earthquake

underscored the vulnerability of existing structures, 160 shops, and five schools in Espungabera, Beira, and Chimoio.

To address these challenges, civil engineering professionals in Mozambique often adopt international standards for structural design to quantify the effects of seismic activity. The most commonly used standard is Eurocode 8, which establishes general guidelines for designing earthquake-resistant structures, including performance requirements, compliance criteria, and safety verification for limit states. Eurocode 8 also covers geotechnical factors, such as ground conditions and seismic action, acknowledging that the interaction between soil and structure is fundamental to a structure's seismic performance. Understanding

soil properties, including parameters for resistance, stiffness, and damping, is therefore essential. This study includes parametric analysis, a historical overview of seismic activity in Mozambique, and geological characterization, aiming to identify proximity to active faults and determine ground type to define seismic action parameters accurately

1.2. Seismic Analysis

1.2.1. Modal analysis by response spectrum

This analysis method is applicable when a structure's geometry does not satisfy the requirements of the lateral force analysis method. It enables seismic analysis of structures with linear behaviour, providing insights into time-dependent responses, particularly the maximum response values. Therefore, all responses from vibration modes that significantly impact the overall structural response must be considered. A mode's contribution is considered significant if the sum of its effective modal masses exceeds 90% of the total mass of the structure and each modal mass is greater than 5% of the total mass. If these conditions are not met, the required number of vibration modes can be determined using the following formulas in Eq. (1) and Eq. (2):

$$k \geq 3 \times \sqrt{n} \quad (1)$$

$$T_k \leq 0.20s \quad (2)$$

Where:

n – represents the number of floors above the foundation;

k – represents the number of modes considered;

T_k – represents the period of mode k .

According to [1], two vibrations are considered independent, while combining modal responses, if the period of the subsequent mode is equal to or less than 90% of the preceding mode's period. If this condition is unmet, a more complex approach, such as the complete quadratic combination (CQC), should be applied.

In cases where a spatial analysis model is adopted, the effects of accidental torsion must also be considered, as they introduce torque moments within the structure. Eurocode 8 (EC8) recommends calculating these moments are calculated using Eq. (3):

$$M_{ai} = e_{ai} \times F_i \quad (3)$$

Where:

M_{ai} – represents the torque moment of the vertical axis applied to the floor i ;

and e_{ai} – represents the accidental eccentricity of the mass on the floor i ;

F_i – represents the horizontal force applied to floor i , in all directions.

The M_{ai} value must be defined taking into account both signs, positive and negative, in order to properly characterize the effect of the eccentricity of the masses on the structure. The seismic combination should be considered using the following Eq. (4) and Eq. (5):

$$E_{EDX} \text{ "+" } 0.30 \times E_{EDY} \quad (4)$$

$$E_{EDX} \times 0.30 \text{ "+" } E_{EDY} \quad (5)$$

Where:

E_{EDX} – represents the stresses resulting from the application of seismic action as a function of the horizontal x-axis of the structure;

E_{EDY} – represents the stresses resulting from the application of

seismic action as a function of the orthogonal horizontal y-axis of the structure.

1.3. Mozambican Seismic Context

According to [2], concerns about seismic risk in Mozambique were quite low, until the earthquakes of February 2006 which accentuated the reality of the risk. Although the prioritization of seismic risk assessment in Mozambique remains open to debate amidst various competing issues, it would be imprudent for professionals in the construction industry to continue designing and building structures without accounting for earthquake resilience.

1.3.1. Regions Prone to Seismic Events in Mozambique

Seismically active areas in Mozambique are located primarily along the African Rift Valley and the Mozambique Channel. The Rift Valley divides near Lake Victoria, located between Kenya, Tanzania, and Uganda, forming two branches: the Western branch, which includes Lakes Tanganyika and Niassa and terminates in central Mozambique, and the Eastern branch, which extends along Kenya and ends in southern Tanzania. The difference in separation speeds within the Rift partly explains why seismic activity in Mozambique's southern Rift areas is less intense and frequent than in the northern regions. However, USGS data indicates that Mozambique has experienced consistent seismic activity over the past 33 years, with most of Southern Africa's seismic activity associated with the East African Rift system.

It is also important to note that cities like Maputo and Beira face an added risk from tidal waves, or tsunamis, which may result from seismic or underwater disturbances as presented in Fig. 1. Provinces within this zone should therefore be prepared for these additional potential hazards [3].

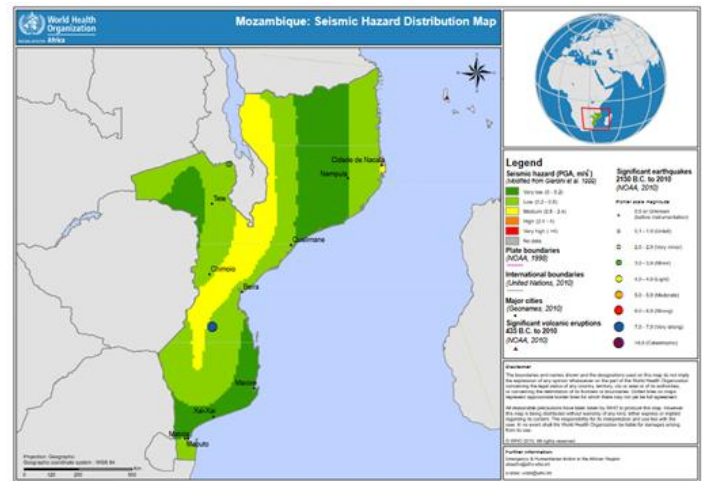


Fig 1. Seismic risk map of Mozambique as per WHO. Dark green: very low risk ($0 - 0.2 \text{ m/s}^2$), light green: low risk ($0.2 - 0.8 \text{ m/s}^2$), yellow: medium risk ($0.8 - 2.4 \text{ m/s}^2$). The blue circle represents the occurrence of an earthquake on a scale of 7.0 to 7.9 MW (Source: adapted from the WHO by the Author, 2024)

1.3. Historical Context of Mozambican Seismic Events

Before 1973, three major events had been recorded. The first was on May 10, 1951, with a magnitude of 6.0 and an epicentre approximately 100 km from Beira. The second and third occurred on July 20 and September 20, 1957, respectively, around 200 km

from Chimoio and Beira; both recorded at the JOH station in Johannesburg with a magnitude of 6.0 [3].

Since 1973, data from the US Geological Survey [4] show that around 256 earthquakes with magnitudes greater than 2.5 have occurred throughout Mozambique. Notably, over 87.5% of these had magnitudes above 4.0, with at least 25 earthquakes reaching 5.0 or higher—generally considered the minimum on the Richter scale for plate movements capable of causing structural damage. The majority of seismic activity in Mozambique is classified as shallow, with 210 recorded earthquakes originating at depths less than 10 km, while only 17.97% of events had foci deeper than 33.3 km. Most of these earthquakes were attributed to normal or strike-slip faults as illustrated in Fig. 2. Moreover, according to the [4], the largest earthquake recorded in the Rift Valley since 1900 reached a magnitude of 7.0, with an epicentre in the Machaze district of Manica province at an approximate depth of 10 km.

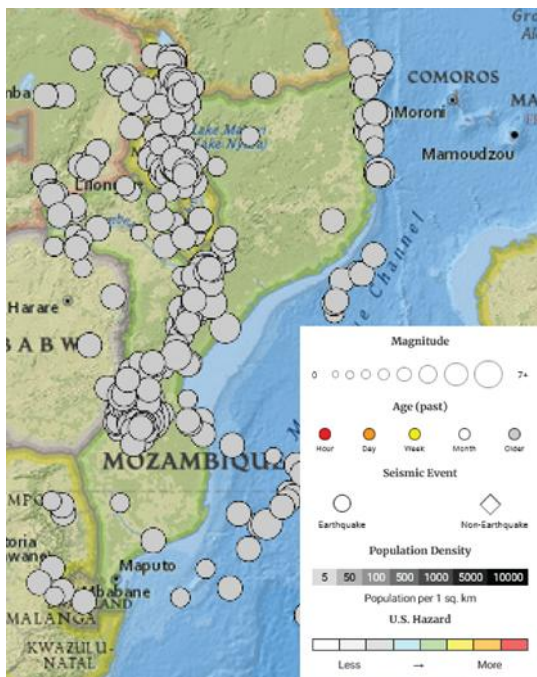


Fig 2. Distribution of seismic activity and representation of epicenters in Mozambican territory, between 1973 and February 2024 (Source: adapted from the USGS by the Author, 2024)

Based on data provided by [4], there has been an increase in seismic activity in the central area of Mozambique since February 2006. This phenomenon has been so frequent that approximately 37.5% of the earthquakes recorded by the USGS since 1973 were observed throughout 2006. Most of the epicentres of these seismic phenomena are located in the Machaze district, in the province of Manica.

• Largest Earthquake Occurred in Mozambique

The largest earthquake recorded in Mozambique occurred on February 22, 2006, in Machaze, Manica province, with a magnitude of 7.0 as shown in Fig. 3. According to [3], this earthquake damaged at least 160 buildings in Espungabera, Beira, and Chimoio, as well as the water supply system in Chitobe. Approximately 300 homes, 8 shops, and 5 schools were affected, along with the degradation of the Inhambane and Maxixe jetties, necessitating emergency intervention. [2] noted that the Machaze earthquake to have been caused by the rupture

of a previously unidentified fault, which presumably might have been an ancient, slow-moving fault or a new structure associated with the southern propagation of the Rift.

The occurrence of a high-magnitude earthquake in an unexpected location underscores the need for thorough seismic vulnerability assessments in Mozambique, as there may be additional, unidentified faults near critical infrastructure. Considering these factors is essential during the structural design phase to account for potential earthquake impacts across the country.

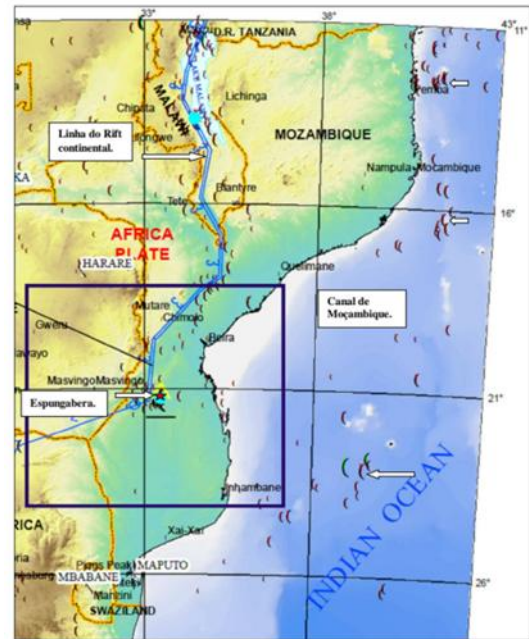


Fig 3. Machaze Earthquake Geographical Location (Source: adapted from the USGS by Author, 2024)

1.4. Mozambican Geological Context

Mozambique is located on the eastern margin of the African Plate, at the southern end of the East African Rift, which delimits the two parts of the African plate that separates it, the Nubian Plate and the Somali Plate, and extends from the Gulf of Aden in the north to the south of Mozambique, for more than 3,000 km [5].

[6] estimated that the Eastern branch of the Rift extends southwards to the Southwest Indian Ridge and that the degree of separation of the Rift is estimated at around 8.3 ± 1.9 mm/year in the Gulf of Aden region and 3.6 ± 0.5 mm/year in the intersection zone of the Eastern branch of the Rift with the ridge, due to persistent seismicity along the Mozambique Channel as illustrated in Fig. 4. Such extensions along the Rift began around 45 million years ago. The first faults around emerged 30 Ma ago in Ethiopia and propagated southwards, with the first faults at the southern end of the Western branch of the Rift emerging around 10 Ma ago [3].

The Rift is moderately developed in the North and Center of the country, where Lakes Niassa and Chirua are located. [2] describes the geology of Mozambique in two-thirds of the country's surface, consisting of crystalline rocks older than 570 Ma, Precambrian terrains, in which tectonic elements resulting from collision processes between plates predominate.

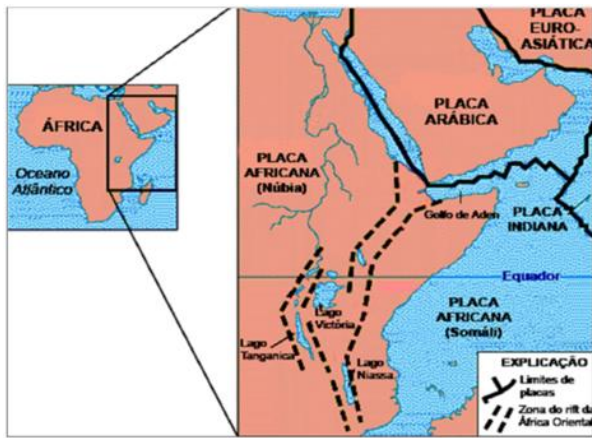


Fig 4. The complex of tectonic faults in East Africa. (Source: adapted from Fonseca, 2010)

This is shown by the occurrence of plateaus configured mainly in the Central and Northern regions of the country, in detail, the plateaus of Niassa, Mueda, Chimoio, and Angónia, as well as the main mountainous formations consisting predominantly of Chimanimani Massif, Maniamba Mountain Range, and the Chire-Namuli Formations. [2], also states that “the remaining surface is made up of sedimentary rocks less than 570 Ma old, Phanerozoic terrains, in which tectonic elements resulting from the opening of the Indian Ocean, associated with the break-up of the supercontinent Gondwana, and tectonic elements resulting from the advance of the Rift are found”.

1.5. Mozambique Seismic Monitoring Infrastructure

Until the 12th of February 2024, Mozambique did not have an independent seismic data analysis and processing centre. Only after the inauguration of the Geology laboratory in the KaMubukuana Municipal District in Maputo City did Mozambique become capable of identifying earthquakes in real time and accurately and efficiently determining the coordinates of earthquake epicentres. This is why seismic event data was made available on the USGS website, which was the fundamental source of data on the date of occurrence, location, magnitude, duration, and depth of earthquakes in Mozambique. It should be noted that this research only includes information on events from 1973 onwards.

1.6. Review of National Regulations

The fact that seismic risk is partially reduced in Mozambican territory the various priorities that occurred in the country during the years of civil war and the presence of other more devastating natural disasters, culminated in the lack of specific regulations for seismic dimensioning in Mozambique.

1.6.1. Limitations of the Existing Regulations

According to the information proclaimed by the Ministry of Public Works and Housing (MOPH) of the Republic of Mozambique cited by [7], “the regulation in force for the dimensioning of reinforced concrete structures is the Regulation for Reinforced and Prestressed Concrete Structures (REBAP, 1983), and for the quantification of static actions it is the Regulation for Safety and Actions for Building and Bridge Structures (RSA, 1983)”. It should be noted that the referenced regulations are full versions of the Portuguese regulations, and no adaptation has been made,

especially for the quantification of actions for the Mozambican context. Although the REBAP presents implicit construction provisions that consider the effects of seismic action, the quantification of this action, as set out in the RSA for Portugal, has been disregarded in structural design in Mozambique.

According to [8], the development of the RSA and REBAP has been in effect for some time now, which increases the need for a review and respective update. Furthermore, although these regulations present some concepts similar to EC8, defined for the improved ductility class, they do not make them applicable conditions in practice. Because these regulations advocate a design in which the structure presents a linear behavior that aims to resist seismic action fundamentally through the resistant capacity of the structural elements in an elastic regime.

EC8 suggests a new philosophy called “Capacity Design”, which allows for non-linear analyses to be carried out, both static (pushover) and dynamic. This type of analysis allows for a more realistic assessment of the behavior of structures, representing their response when subjected to seismic actions more reliably. Although the results of the survey conducted for this research do not represent the universe of civil engineering professionals in Mozambique, some consider that the use of RSA and REBAP are essentially conservative in nature, since they lead to the oversizing of structures, which may provide greater lateral resistance when subjected to seismic excitations.

1.6.2. Differences Between the Existing Regulation and Eurocode 8

According to [8] aspect that denotes the need for a review of the RSA, “is the fact that it does not refer to any verification associated with the limitation of damages, one of the major differences between the two regulations, thus highlighting the importance that EC8 gives to the limitation of economic losses”. It is also worth noting that in the RSA, seismic action is considered a variable action, and therefore has a probability of exceeding 5% in 50 years. Therefore, we are faced with a disparity between a return period of 475 years defined in EC8 and the 975 years established in the RSA. Concerning seismic zoning, enormous changes arise in EC8, compared to that established in the RSA, decimating the lack of coherence of the RSA, whose zoning is unique and developed according to distant seismic action, since, depending on whether distant seismic action or close seismic action is considered, there will be different epicentre positions.

Concerning the types of ground conditions, it is also worth noting the greater rigour on the part of EC8, which considers five types of ground conditions, unlike the RSA, which establishes three types of ground conditions. The aim is therefore to achieve a more defined and coherent classification, which is consistent with the values defined in the response spectra, which show considerable differences in spectral acceleration depending on the type of soil in question, thus justifying the need for a more cautious and demanding discretization of the different types of terrain. Therefore, regarding the representation of seismic action, both present two types of seismic action, in detail, the moderate magnitude earthquake at a small focal distance and the greater magnitude earthquake at a greater focal distance. Regarding ductility classes, a similar scenario is noted between structures with the low ductility class in EC8 and the Normal Ductility structures recommended in REBAP. “As for

the Medium and High ductility classes of EC8, there is a significant difference to REBAP in that it only presents an additional ductility class called Improved Ductility. Therefore, there is no direct relationship between classes, however, Improved Ductility structures are similar to Medium Ductility structures (MCD)” [8].

Given these and other aspects, and so that the effect of seismic action is precisely defined and quantified in the best possible way, Eurocode 8 was drawn up, which emerges as a European regulatory standard for structural dimensioning in the face of seismic action, and which replaces part of the regulations relating to seismic action that apply to Portugal, namely RSA and REBAP, which, having been drawn up more than thirty-seven years ago, are now outdated and have some omissions that need to be filled.

1.6.3. Safety Verification of Structural Elements based on EC8

EC8 and EC2 provide important rules for verifying safety, relating to beams and columns. In this context, an approach is made to the geometric constraints, the quantification of sizing actions and the verification of the ultimate limit state.

2. Materials and modeling

2.1. Characterization of the Building

The building considered in this research is intended for institutional use as shown in Fig. 5. It consists of 3 floors with a ceiling height of 3.00 m, in a reinforced concrete frame of footings, piles, rectangular pillars of (0.20x0.80) m², (0.20x1.00) m² and circular ones with a radius of 0.30 m and 0.35 m, beams of (0.20x0.50) m², (0.20x0.60) m² and (0.20x0.70) m² and slabs with a thickness of 20 cm and 22 cm. All floors are intended to serve the offices and services related to UNICEF activities. The building has a total area of 818.00 m², distributed by floor according to the Table



1. Fig 5. Main facade of the building under study (Source: adapted from ArchiCad 24.0.0 INT Component by Author, 2024)

Table 1. Description of the building areas (Source: adapted from project by Author, 2024)

Floor	Gross Area (m ²)	Height (m)	Function
Ground floor	261.80	3.00	Office
1st Floor	277.55	3.00	Office
2nd floor	278.65	3.00	Office
Terrace	108.75		Warehouse
Total	926.75	9.00	

The data in Table 1 were obtained from the architectonic project of the building, where the area of each individual floor was calculated due to the building's varying geometric forms across different floor. Since it is a private building, we must protect the interests of the owners. Therefore, readers who require detailed access to the floor plans should contact the authors.

2.2. Geographical Location

The building under study, namely the UNICEF Offices, is located in Maputo City, at Avenida do Zimbabwe, No. 1422/1440, Sommerschild Burgh, Plot No. 141B/399 in the District of Sommerschild, Kampfumo, on a regular plot of land with plan dimensions of 18x78, and with the following coordinates (Lat: -25.954963, Long: 32.59 4350) as presented in Fig. 6.



Fig 6. Main facade of the building under study (Source: adapted from ArchiCad 24.0.0 INT Component by Author, 2024)

2.3. Structural Materials

In order to ensure the building's resistance to seismic action in plastic regimes, the structure is composed of reinforced concrete, resistance class C25/30, and A400 NR SD steel as indicated in Table 2.

Table 2. Characteristics of the concrete and steel adopted

Concrete C25/30	Steel A400 NR SD
$f_{ck} = 25.0$ MPa	$f_{yk} = 400$ MPa
$f_{cd} = 16.7$ MPa	$f_{vd} = 348$ MPa
$f_{ctm} = 2.6$ MPa	$E_s = 200$ GPa
$E_{cm} = 31.0$ GPa	$\gamma_s = 78.5$ kN/m ³
$\gamma_c = 25.0$ kN/m ³	

2.4. Geotechnical Conditions

Based on the variability like the soil, a geotechnical assessment carried out by [9] indicates that the building has deep foundations consisting of bored concrete piles with a diameter of 0.60 m and a length of 18 m and 20 m to take into account the expected settlements and the bearing capacity of the soil. Due to the low bearing resistance of the soil, the length of the pile was dimensioned considering the friction resistance, limited to 75 kPa. The transition between the piles and the pillars is made by concrete blocks with a height of 0.80 m, joined by earth beams with sections ranging from (0.35x0.80) m² to (0.30x0.60) m².

2.5. Acting Actions

An action represents any agent capable of producing significant states of tension or deformation in any structural element (Testino, 2023) are presented in Table 3.

2.5.1. Permanent actions

Table 3 summarizes the permanent actions considered in the structural analysis, including the self-weight of materials such as reinforced concrete and steel, as well as additional loads from slab coverings and masonry walls.

Table 3. Quantification of permanent actions (Source: adapted by Author, 2024)

Permanent Actions	Load
DL Reinforced Concrete	25.0 kN/m ³
DL Steel	78.5 kN/m ³
SIL Slab Covering (Ground floor, 1st floor)	1.2 kN/m ²
SIL Slab Covering (2 nd floor)	2.0 kN/m ²
SIL Slab Covering (Terrace)	1.5 kN/m ²
SIL Internal masonry wall	1.5 kN/m ²
SIL External masonry wall	6.4 kN/m ²

2.5.2. Variable Actions

The building belongs to categories B and C5, relating to the office and warehouse areas, with the presence of a non-accessible roof of category H as illustrated in Table 4.

Table 4. Values of overloads and combination coefficients (Source: adapted from EC1 and EN 1990 by Author, 2024)

Category of areas	Category	q _k (kN/m ²)	Coefficients		
			Ψ ₀	Ψ ₁	Ψ ₂
Floors	B	3.0	0.7	0.5	0.3
	C5	5.0	0.7	0.7	0.6
Non-accessible roof	H	1.0	0	0	0

Where:

q_k - Value of uniformly distributed overload;

Ψ₀, Ψ₁, Ψ₂ - Combination coefficients.

2.5.3. Thermal Actions

According to EC2, it is not necessary to consider the effects of thermal action, since the building's dimensions in the plan are less than 30 m.

2.5.4. Wind Action (WD)

Based on EC1, the parameters adopted to quantify the effects of wind action are as given in Table 5:

Table 5. Parameters adopted to quantify wind action according to EC1, 1991

Zone Classification	Zone B	v _b = 30 m/s
Terrain Category	Type II	z ₀ = 0.05 m; z _{min} = 3.0m
Peak dynamic pressure q _p (z)	q _p (z) = 1.23 kN / m ²	

In any case, it was found that wind action is less conditioning when compared to seismic action.

2.5.5. Seismic Action (SE)

To characterize the seismic action in the analysis of the building under study, the fundamental principles of EC8 were considered. As such, the definition of seismic action is based on acceleration response spectra, which reveal the seismic movement on the ground

surface, having two quantities, vertical component and horizontal component. However, for this project, only the horizontal seismic action was considered. While designing seismic action, a parametric study of the site must be carried out, with a view to defining the characterization of the seismic zone under study, the typology of the terrain where the structure is located as shown in Table 9, the importance class of the structure as given in Table 7, and the acceleration on the surface [9] as presented in Table 8.

2.5.5.1. Characterization of the Seismic Zone

According to the [11], the study site is located in a low seismic risk zone, with earthquakes that cause surface acceleration of up to: PGA < 0.8 m/s² as indicated in Table 6.

Table 6. The reference value of maximum acceleration

Region	Seismic Action	agR (m/s ²)
Maputo	Type 1	0.8
	Type 2	0.8

2.5.5.2. Terrain Type

The building under study is considered to be located on a Type D terrain, described as a “deposit of non-cohesive soils of low to medium compactness, with or without some strata of soft cohesive soils, or of predominantly cohesive soils of soft to hard consistency” [12].

2.5.5.3. Importance Class

Table 7 presents the importance coefficients (γ₁) used for seismic analysis, based on EC8 guidelines. For Importance Class II buildings, a value of 1.00 is applied for both interplate and intraplate seismic actions.

Table 7. Importance coefficients γ₁ (Source: adapted from EC8 by the author, 2024).

Importance Class	Seismic Action Type 1 (Interplate)	Seismic Action Type 2 (Intraplate)	
II	1.00	1.00	1.00

2.5.5.4. Surface Acceleration

Having defined the reference value of the maximum acceleration and the importance coefficient, it becomes possible to define the value of the surface acceleration through the following expression in Eq. (6):

$$A_g = \gamma_1 \times A_{gR} \quad (6)$$

Where:

A_g – calculation value of the surface acceleration;

γ₁ – importance coefficient;

A_{gR} – represents the reference value of the maximum acceleration of the ground.

Table 8. Surface acceleration values (Source: adapted from EC8 by the Author, 2024).

Region	Seismic Action	AgR (m/s ²)	γ ₁	Ag (m/s ²)
Maputo	Type 1	0.8	1.0	0.8
	Type 2	0.8	1.0	0.8

2.5.5.5. Soil Coefficient

Assuming that the surface acceleration value is Ag ≤ 1 m/s², the

soil coefficient is defined based on the following expression in Eq. (7):

$$S = S_{max} \quad (7)$$

2.5.5.6. Other Parameters for Characterizing Seismic Action

Table 9 shows the values of key parameters for the elastic response spectrum on terrain type D, based on EC8. The parameters vary depending on whether the seismic action is Type I (interplate) or Type II (intraplate), with notable differences in the period values.

Table 9. Values of the remaining parameters of the elastic response spectrum for action Type I and II seismic (Source: adapted from EC8 by the Author, 2024)

Terrain Type	S	T _B (s)	T _C (s)	T _D (s)
	max			
D (Type I Earthquake)	2.0	0.1	0.8	2.0
D (Type II Earthquake)	2.0	0.1	0.3	2.0

2.5.5.7. Horizontal Elastic Response Spectrum of Acceleration

With the characterization factors of the seismic action obtained, the horizontal elastic response spectrum of acceleration $S_e(T)$ was defined, which represents the horizontal seismic action of the ground movement as shown in Fig. 7 and Fig. 8. This spectrum is determined by [12] according to the following expression Eq. (8):

$$T_c \leq T \leq T_D : S_e(T) = A_g \times S \times \eta \times 2,5 \times \left[\frac{T_c}{T} \right] \quad (8)$$

Where:

$S_e(T)$ – elastic response spectrum;

T – vibration period of a linear system with one degree of freedom;

A_g – design value of the acceleration at the surface;

T_B – represents the value of the lower limit of the spectral acceleration period;

T_C – represents the value of the upper limit of the spectral acceleration period;

T_D – value that defines the beginning of the branch displacement in the response spectrum;

S – represents the soil coefficient;

η – represents the damping correction coefficient, with the reference value $\eta = 1$ for 5% viscous damping.

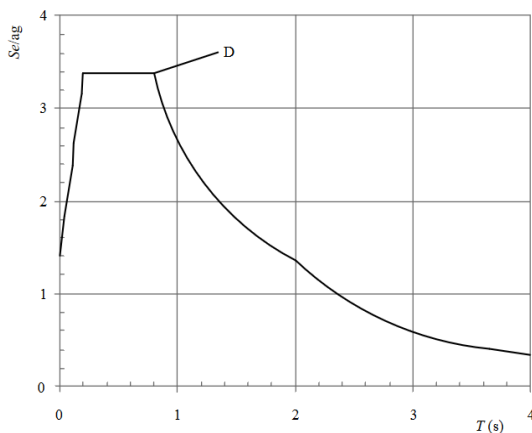


Fig 7. Type I elastic response spectrum recommended for type D ground with 5% damping (Source: adapted from EC8 by the Author, 2024)

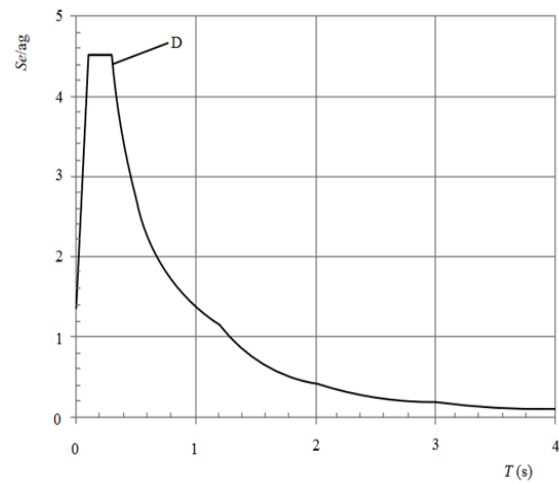


Fig 8. Type II elastic response spectrum recommended for type D ground with 5% damping (Source: adapted from EC8 by the Author, 2024)

2.6. Action Combinations

The study of action combinations is carried out to study the most unfavourable effects that the structure may be subjected to. These combinations are analyzed for Service Limit States (SLS) and Ultimate Limit States (ULS) are presented in Table 10 and Table 11.

Table 10. Project Action Combinations (Source: adapted by Author, 2024)

Case	Analysis Type	Combination
1	ULS	$1.35 \times (DL + SIL) + 1.5 \times LL$
2	SLS	$1.00 \times (DL + SIL) + 1.0 \times LL$
3	Seismic	$1.00 \times (SEX + SEY)$
4	Seismic X	$1.00 \times (DL + SIL) + 1.0 \times LL + 1.0 \times SEX$
5	Seismic Y	$1.00 \times (DL + SIL) + 1.0 \times LL + 1.0 \times SEY$
6	$E_{EDX} \text{ "+" } 0.30 \times E_{EDY}$	$1.00 \times SEX + 0.30 \times SEY$
7	$E_{EDX} \times 0.30 \text{ "+" } E_{EDY}$	$0.30 \times SEX + 1.00 \times SEY$

2.6.1. Partial's Coefficients Security (γ) and coefficients combination (ψ)

Table 11. Partial Coefficients security and adopted coefficients combination (Source: adapted of EC0 by Author, 2024)

Action		Partial's Coefficients (γ)		Coefficients (ψ)		
		Favourable	Unfavorable	Ψ_0	Ψ_1	Ψ_2
Permanent Actions	DL	1.35	1.00	-	-	-
	SIL	1.35	1.00	-	-	-
	LL	1.50	0.00	-	-	-
Variable Actions	TL	1.50	0.00	0.6	0.5	0.0
	IF	1.00	0.00	-	-	-
	WD	1.50	0.00	0.6	0.2	0.0

2.7. Effect of Seismic Action, Modeling and Structural Analysis

To ensure that the objective of the earthquake-resistant design based on EC8 is achieved, two levels of seismic verification arise, namely, the requirement of non-collapse and the requirement of damage limitation. These requirements are fundamental for the

structure to have good seismic performance. The complexity of manually calculating structural elements, to obtain a dynamic and elastic structural analysis, demands the use of an automatic calculation tool. Therefore, to carry out this analysis, AutoDesk Robot Structural Analysis Professional 2020 was used, in which all the structural and geometric characteristics of the building were defined, including the acting actions. Based on the created model, a structural analysis was carried out using the appropriate analysis method prescribed by EC8, namely the modal analysis by response spectrum about the consideration of the effect of seismic action.

2.7.1. Effects of Seismic Action

In order to analyze the effects of seismic action on the building under study, the structural characterization of the building was carried out and the regularities in plan and height were checked, with emphasis on the ductility class and the value of the behavior coefficient, to obtain the response spectrum for calculation based on EC8.

2.7.2. Structural Characterization of the Building

Based on the geographical location of the building under study and a preliminary description of the geometric dimensions of the structural elements, a structural characterization was carried out, considering that the building was designed based on the basic principles of EC8, proving useful for ensuring the fundamental requirements of non-occurrence of collapse and damage limitation. From this perspective, the building incorporates the solution of uncoupled reinforced concrete walls that start from the foundations and extend to the terrace, which is characterized by the presence of beams, pillars and walls that support the gravitational loads coming from the solid slab floors.

2.7.2.1. Regularity in Plan

The building's plan shows that the structure, although it appears to be regular in plan, meets the slenderness criterion, in which in the largest direction, the structure is 18.00 m and in the smallest, it is 14.80 m, which results in a slenderness of 1.22, which is less than the 4 recommended in EC8. And, because it has a compact plan, with setbacks that do not affect the rigidity of the floor in the plan. This is not because it does not present symmetry in relation to all dimensions of the building x and y, thus compromising the verification of the regularity criterion in the plan is given as Eq. (9).

$$\lambda = \frac{L_{max}}{L_{min}} = \frac{18,00 \text{ m}}{15,20 \text{ m}} = 1,18 \leq 4 \quad (9)$$

Where:

L_{max} – largest dimension in plan of the building;

L_{min} – smallest dimension in plan of the building.

2.7.2.2. Regularity in Height

In accordance with EC8, the following checks were carried out for the building under study:

- ✓ The lateral load-bearing systems, in particular the frames and the core (stairwell), are not interrupted from the foundations to the top of the building;

- ✓ The lateral stiffness and mass of each floor show a gradual reduction, with no sudden variations, from the base to the terrace of the building structure;
- ✓ The building does not have set-back floors, so the conditions relating to this type of situation are not required to be checked.

As such, it can be concluded that the building under study is regular in height.

2.7.3. Behavior Coefficient

The behavior coefficient (q) is a parameter used to perform calculations with the aim of reducing the forces obtained in a linear analysis, representing an approximation of the ratio between the seismic forces, in which the structure is in an elastic response regime, with 5 % damping, and the seismic force, with non-linear behavior where showed in Table 12. It should be noted that the behavior coefficient is associated with the material and depends on the regularity in height and plan, the ductility class and the structural system is calculated sing Eq. (10).

$$q = q_0 \times k_w \geq 1,5 \quad (10)$$

Where:

q_0 – basic value of the behavior coefficient;

k_w – coefficient that reflects the predominant failure mode in structural wall systems.

Table 12. Value of the behavior coefficient in a regular system in height
(Source: adapted from EC8 by the Author, 2024)

Structural Type	DCM
Uncoupled wall system	3.0

2.7.3.1. Calculation Response Spectra based on EC8

After calculating the behavior coefficient “ q ”, a reduced response spectrum was defined in relation to the elastic response spectrum as given by Eq. (11). This reduction allows the evaluation of the energy dissipation capacity of the structure as illustrated in Fig. 9 and Fig.10.

$$T_c \leq T \leq T_D; \geq \beta \times A_g : S_d(T) = A_g \times S \times 2,5 \times \left[\frac{T_c}{T} \right] \quad (11)$$

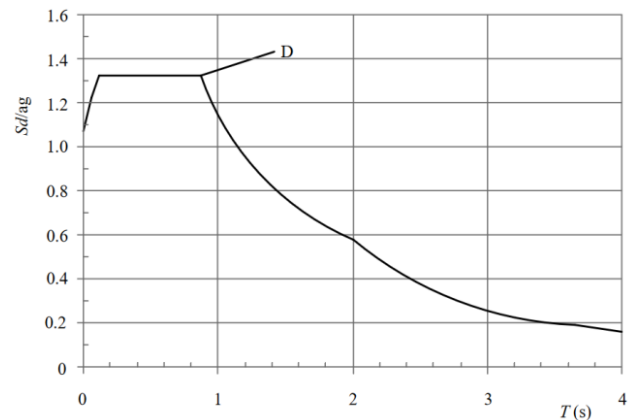


Fig 9. The response spectrum of calculation for Type I seismic action by the behavioral coefficient, $q = 3.0$ (Source: adapted from MATLAB by the Author, 2024)

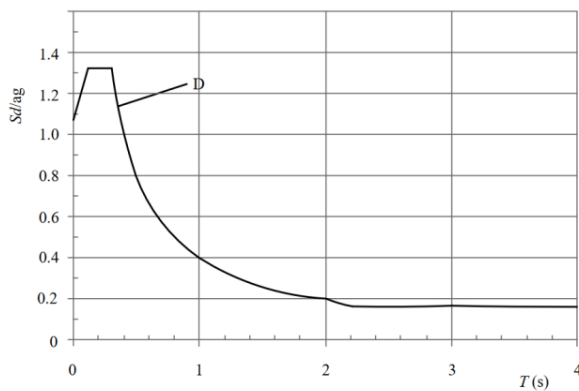


Fig 10. The response spectrum of calculation for Type II seismic action by the behavioral coefficient, $q = 3.0$ (Source: adapted from MATLAB by the Author, 2024)

2.7.4. Structural Modeling

To model the structure of the building under study, the AutoDesk Robot Structural Analysis Professional software, version 2020, was used, defining the geometric characteristics, the materials in relation to the structural elements and the actions subjected to the structure with the respective calculation combinations.

2.7.4.1. Modeling Methodology

Based on the structural characterization of the building and the classification of the structural system, the building under study sought to follow this process of modelling the different structural elements and the acting actions, making simplifications possible. Therefore, to obtain the structural model of the building and determine the forces to which it is subject, the modelling was carried out according to the following methodology:

- ✓ Definition of the geometry as illustrated in Fig. 11;
- ✓ Definition of the materials and structural elements;
- ✓ Definition of the loads and combination of the actions.

2.7.4.2. Definition of Geometry

In Robot Structural Analysis Professional 2020, the design of the structure's geometry is carried out by defining a structural mesh consisting of a three-dimensional grid, made in accordance with the positioning of the structural elements and their respective midlines (structural axes) as presented in Fig. 12. It should be noted that this project is of an existing structure, in which measurements were carried out to obtain a more realistic representation of what exists on the ground, and at the same time the safety terms of the ULS and SLS conditions defined by Eurocodes were followed.

2.7.4.3. Definition of Materials and Structural Elements

To design the structural model in the calculation software, it was essential to define the materials and cross-sections of the respective structural elements. The materials were defined based on the characteristics described a priori for the structural materials.

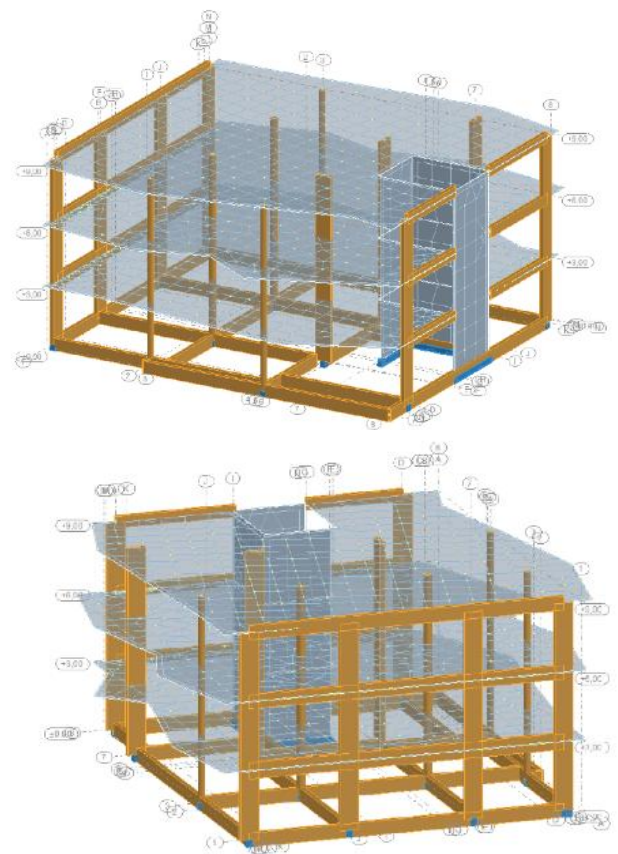


Fig 11.3 D model of the structure in Robot Structural Analysis
Professional 2020: Main elevation and Rear elevation, respectively
(Source: adapted from Robot by the Author, 2024)

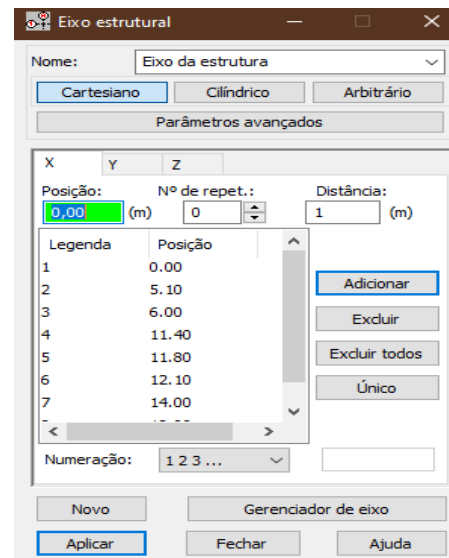


Fig 12. Definition of the structural axis (Source: adapted from Robot by the Author, 2024)

Regarding the elements, two types of structural elements were defined:

- ✓ Bar elements (Frame), which represent the 2-node finite elements;
- ✓ Shell elements (Shell), which represent the 4-node finite elements.

2.7.4.3.1. Columns and beams

The columns and beams were introduced with the help of axes, to guarantee the accuracy of the definition of their coordinates, and were defined in the model as bar elements (Frame) as shown in Fig. 13. Following EC8, and to account for the effect of cracking, the elastic stiffness to bending and shear force was reduced by 50% in both directions of the reinforced concrete bar elements. Regarding the modelling of the beams, their axis was positioned to coincide with the floor level.

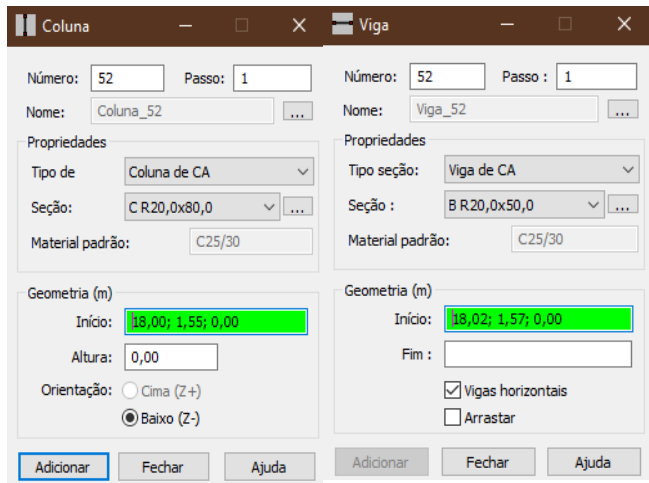


Fig 13. Definition of the columns and beams, respectively (Source: adapted from Robot by the Author, 2024)

2.7.4.3.2. Slabs

The slabs were modelled as shell elements using the Floor option, which allows the representation of homogeneous slabs, taking into account the effects of cross-sectional deformation as presented in Fig. 14. To obtain more accurate results, the slabs were discretized by converting the architectural project into a Robot, to trace the slab contours and also respect the rigid diaphragm condition on the floors.

2.7.4.3.3. Stairs

The stairs were not incorporated into the modelling of the structure of the building under study. To quantify the actions obtained by the existence of the stairs, a gravity shear load of 2.5 kN /m was defined on each floor and the stair core walls.

2.7.4.3.4. Staircase core walls

All the walls of the staircase core were modelled from the shell elements as Illustrated in Fig. 15.

2.7.4.3.5. Definition of Loads and Combination of Actions

The self-weight of the structural elements is considered automatically in Robot Structural Analysis Professional (2020). Meanwhile, the loads of the non-structural elements and the overloads were introduced into the model as surface and linear loads uniformly distributed on the slabs and beams, as applicable, and were defined based on the action table presented above.

To quantify the effect of the seismic action, the calculated response spectra ($S_d(T)$) were inserted into the model according

to EC8 for the two seismic actions related to the Mozambican territory as presented in Fig. 16.

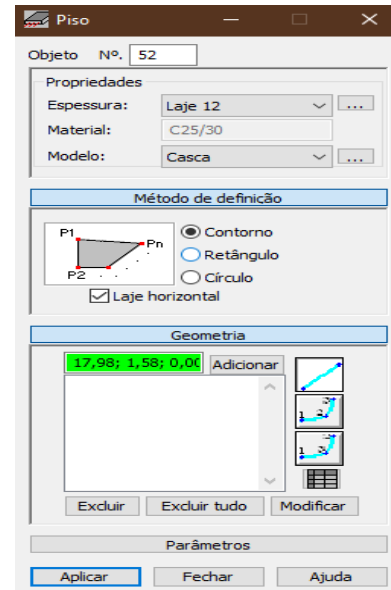


Fig 14. Definition of slabs (Source: adapted from Robot by the Author, 2024)

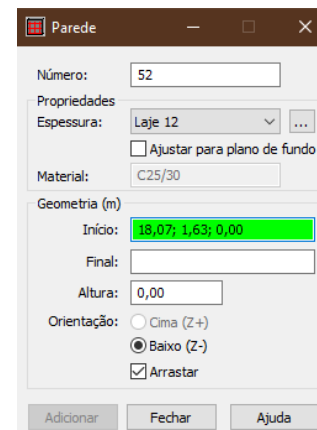


Fig 15. Definition of the walls

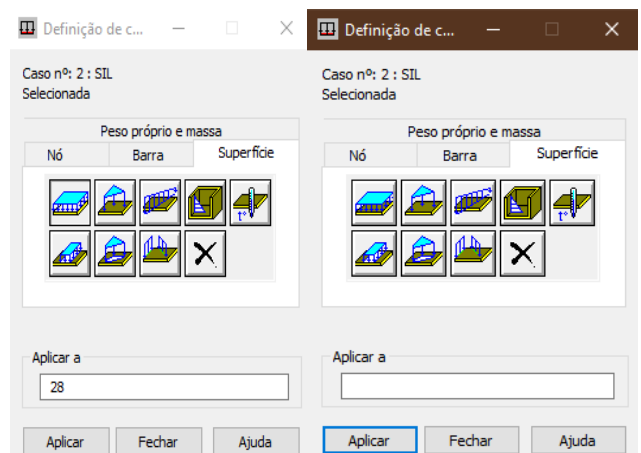


Fig 16. Definition of loads and types of loads

2.7.4.4. Simplifications adopted

The modelling of the building under study addresses three specificities that stand out: the modelling with equivalent sections of the structural elements, the disregard of the soil/structure interaction as illustrated in Fig. 17, since a perfect embedment of the supports at the base is considered, and the modelling of a rigid diaphragm at the level of the floors.

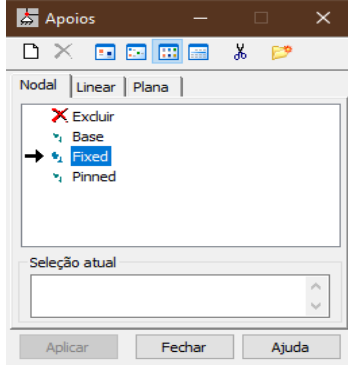


Fig 17. Definition of the embedded supports

2.7.5. Structural analysis

The analysis of the demands is carried out through a 3D spatial calculation, using matrix stiffness methods, considering all the elements that define the structure: columns, walls, beams and slabs. In short, the structure is discretized into bar-type elements, bar mesh and nodes, subject to the action of vertical and horizontal loads. The models are of flat lattice structures, arranged in a rectangular grid that allows the following hypotheses:

- ✓ The structure's behavior is geometrically and physically linear, corroborating the principle of superposition of effects;
- ✓ The floors establish non-deformable diaphragms in their plane;
- ✓ The horizontal forces, which result from the dynamic analysis of the three-dimensional structure, are based on a uniform distribution of the mass across the entire surface of the floors, and act at the level of each floor.
- ✓ The static calculation is performed by solving the following system of linear equations as Eq. (12):

$$[K] \times \{U\} = \{R\} \quad (12)$$

Where:

$[K]$ – represents the stiffness matrix;

$\{U\}$ – represents the displacement vector;

$\{R\}$ – represents the load vector.

- ✓ The dynamic analysis is performed by solving the following dynamic equilibrium system of equations, which relates the movement of the ground to the response of the structure is calculated using Eq. (13):

$$M\ddot{u} + C\dot{u} + Ku = M\ddot{u}_g \quad (13)$$

Where:

M – represents the mass matrix;

C – represents the damping matrix;

K – represents the stiffness matrix;

\ddot{u}_g – represents the ground acceleration;

\ddot{u} , \dot{u} and u – represent the acceleration, velocity and displacement of the structure, respectively.

2.7.5.1. Limit State of Cracking

For the situations in which it is intended to verify the cracking limit state, the following methodology is followed. According to [13], the cracking limit state is considered satisfied if the characteristic value of the crack width ω_k , at the level of the most tensioned reinforcement, does not exceed the value of 0.40mm for structural elements with exposure class XC1 and 0.30mm for structural elements belonging to other exposure classes. The characteristic opening crack value, ω_k , is calculated by using the following expression Eq. (14) defined by Eq.(15), Eq.(16), Eq. (17), Eq. (18) and Eq. (19):

$$\omega_k = s_{r,max}(\epsilon_{sm} - \epsilon_{cm}) \quad (14)$$

Where:

$$s_{r,max} = k_3 c + k_1 k_2 k_4 \sigma / \rho_{p,eff} \quad (15)$$

$$\epsilon_{sm} - \epsilon_{cm} = \sigma_s - k_t \times f_{ct,eff} / \rho_{p,eff} \times (1 + \alpha_e \times \rho_{p,eff}) / E_s \geq 0.60 \times \sigma_s / E_s \quad (16)$$

$$\alpha_e = E_s / E_{cm} \quad (17)$$

$$\rho_{p,eff} = A_s / A_{c,eff} \quad (18)$$

c – longitudinal reinforcement cover;

$k_1 = 0.8$ for high bond bars;

$k_2 = 0.5$ for bending or $= 1.0$ for pure tension; for eccentric tension

$$k_2 = (\epsilon_1 + \epsilon_2) / (2\epsilon_1); \quad (19)$$

$k_3 = 3.4$;

$k_4 = 0.425$

2.7.5.2. Limit State of Deformation

The verification of the limit state of deformation is carried out following the Eurocode 2 standard, which specifies that in most structures the deformation for the quasi-permanent combination of actions must be limited to $L/250$. However, whenever the deformation induced by a certain element of the structure can cause damage to fragile elements, such as masonry walls or coatings, the deformation after the execution of the element or finishing in question must be limited to $L/500$.

The long-term deformation can be estimated using the following expression Eq. (20):

$$a^\infty = a_c(qp) \times (1 + \phi) \quad (20)$$

Where:

$a_c(qp)$ = elastic deformation due to the quasi-permanent combination;

ϕ = creep coefficient (adopted value = 2.00).

So, the value of long-term deformation (mm) for all floors is $9\text{mm} \leq L/500 = 6.40/500 \approx 13\text{mm}$.

2.7.5.3. Classification of the structural system

The classification of the structural system was carried out following EC8, considering the uncoupled wall system, with the

ductility class DCM, since the resistance to basal shear stress is ensured by most of the columns, which end up being considered as walls, since the following condition is verified $h \geq 4b$, and is also guaranteed by the core of the stairs, which is also considered a wall system. The structure of the building under study does not have beams coupling the structural walls, to ensure the lateral resistance of the building through its deformation capacity and a potential for shear rupture, which culminates in the classification of the uncoupled wall system as given by Eq. (21).

$$\begin{aligned} h &\geq 4b \\ 80 \text{ cm} &\geq 4 \times 20 \text{ cm} \end{aligned} \quad (21)$$

Where:

h - represents the length of the column;

b - represents the width of the column.

2.7.5.4. Modal Analysis by Response Spectrum

To carry out the analysis of the structural seismic vulnerability of the building under study, a modal analysis by spectrum was carried out, which makes it possible to obtain the vibration modes of the structure and their respective periods and related frequencies. The period related to each vibration mode gives us the time that the structure takes to perform a complete oscillation, while the frequency shows us the number of complete oscillations performed per second during the occurrence of an earthquake. From the modal analysis by spectrum, the mass participation factors were determined in each direction and for each vibration mode, thus making it possible to analyze the effects of each of the modes on the global response of the structure of the building under study are calculated using Eq. (22) and Eq. (23). Minimum number of modes:

$$k \geq 3 \times \sqrt{n} = 3 \times \sqrt{4} = \quad (22)$$

Vibration period of the last mode:

$$T_k \leq 0.20s \quad (23)$$

2.7.5.5. Horizontal seismic forces

The previously defined and represented calculation response spectrum was inserted into Robot Structural Analysis Professional (2020). After applying the response spectra in the respective directions, the value of the basal shear forces acting on the base of the structure in response to the displacements caused by the seismic action was obtained.

“These forces depend, in addition to the earthquake and the components that characterize it in the response spectra, on the masses above the ground, that is, on the gravitational forces that vibrate and also on the fundamental frequency of the building” [3].

2.7.5.6. Accidental Torsion Effects

Through the accidental effects of torsion, it becomes possible to quantify the uncertainty in the location of the masses throughout the useful life of the structure and the spatial variation of the seismic movement. The accidental eccentricity of the center of mass in each floor i can be calculated, which according to EC8 will be displaced by approximately 5% in each direction about its nominal position, according to the following formula in Eq. (24), Eq. (25) and Eq. (26):

$$e_{ai} = \pm 0,05 \times L_i \quad (24)$$

$$e_{ax} = \pm 0,05 \times L_x = \pm 0,05 \times 18 \text{ m} = 0.90 \text{ m} \quad (25)$$

$$e_{ay} = \pm 0,05 \times L_y = \pm 0,05 \times 15.2 \text{ m} = 0.76 \text{ m} \quad (26)$$

Where:

e_{ai} —represents the accidental eccentricity of the mass of floor i ;
 L_i — represents the dimension of the floor in the direction perpendicular to the direction of the seismic action.

Based on EC8, the accidental effects of torsion are defined as the envelope of the effects resulting from the application of static loads composed of sets of torsional moments, around the vertical axis z , subjected to each floor i . From the following expression, the torsional moments can be calculated in both directions X and Y using Eq. (27), Eq. (28) and Eq. (29):

$$M_{ai} = e_{ai} \times F_i \quad (27)$$

$$M_{ax} = 0.90 \text{ m} \times 1423 \text{ kN} = 1280,7 \text{ kNm} \quad (28)$$

$$M_{ay} = 0.76 \text{ m} \times 1282 \text{ kN} = 974,32 \text{ kNm} \quad (29)$$

Where:

M_{ai} — represents the torsional moment of the vertical axis z , applied to the floor i , in kNm;

e_{ai} —represents the accidental eccentricity of the mass of floor i , for all directions X and Y considered, in meters;

F_i — represents the horizontal force acting on the floor i , determined for the X and Y directions, in kN.

2.7.5.7. Calculation of Maximum Displacements of the Structure

With the help of the automatic calculation program, Robot Structural Analysis Professional (2020), the maximum displacements of the structure in the x and y directions were calculated, considering that the structure is subjected to complete quadratic combinations of modal displacements to obtain the final value of seismic actions. Thus, the displacements are obtained from the following equation Eq. (30):

$$U_{Final} = U_{projecto} \times q \quad (30)$$

Where:

U_{Final} — represents the final displacement of the structure in the linear analysis;

$U_{projecto}$ — represents the displacement obtained from the linear analysis from the application of the calculation response spectrum.

2.7.5.8. Calculation of Relative Displacements between Floors (Drift)

The evaluation of the relative displacements between floors is carried out directly in Robot Structural Analysis Professional (2020). Damage limitation control is carried out following EC8, which defines that for buildings with non-structural elements made of fragile materials fixed to the structure, the displacement between floors (d_r) must be limited to using Eq. (31):

$$d_r = 0.005 \frac{h}{v} \quad (31)$$

Where:

h — represents the height between floors;

v – represents the reduction coefficient equal to 0.40 for type I earthquakes and 0.55 for type II earthquakes.

2.7.5.9. Second-Order Effects

Second-order effects, when compared with first-order effects resulting from the actions and geometric irregularities of the structure, represent the additional effects resulting from the deformation of the structure. Therefore, it is imperative to check the value of the sensitivity coefficient to relative displacement between floors (θ), and based on EC8, second-order effects are not considered if the following condition given in Eq. (32) is met on all floors:

$$\theta = \frac{P_{tot} \times d_r}{V_{tot} \times h} \leq 0,10 \quad (32)$$

Where:

θ – represents the sensitivity coefficient to relative displacement between floors;

P_{tot} – represents the total gravity load from all floors above the floor considered, including this one, in the seismic design situation;

d_r – represents the design value of the relative displacement between floors, analyzed as the difference between the average lateral displacements at the top and bottom of the floor considered;

V_{tot} – represents the total seismic shear force on the floor under analysis;

h – represents the height between floors.

For situations where the sensitivity coefficient to relative displacement between floors (θ) is less than or equal to 0.10, second-order effects do not need to be considered. If the value of the coefficient θ is between 0.10 and 0.20, the seismic forces should be increased by a factor equal to $1/(1-\theta)$, and in no case should the value of the coefficient θ be greater than 0.30.

3. Results and discussions

3.1. Linear Analysis Results

The tables of the mass values considered in the definition of the dynamic characteristics of the structure, such as the periods, frequencies, modal participation values and the due percentage of mass contribution for each mode are presented in Table 13.

Regarding the first three vibration modes as illustrated in Fig. 18 and Fig. 20, it can be seen that the 1st Mode has the largest modal share (as shown in Fig. 18), which is related to torsion at 86.06%, while the 2nd mode presented in Fig. 19 has a translation in the X direction at 96.83% and the 3rd Mode as illustrated in Fig. 20 with a translation in the Y direction at 98.74%. The periods of 1st, 2nd and 3rd modes of vibration are 1.10, 1.05 and 0.81, respectively. It is worth remembering that these data are calculated from the response spectra proposed by Eurocode 8 combined with the ground accelerations proposed by the World Health Organization for Mozambique. With this, it was possible through the Robot to calculate the frequencies, periods and modal participation values of the structure, thus allowing us to understand that this structure is more influenced by the type II earthquake, as it presents high frequencies.

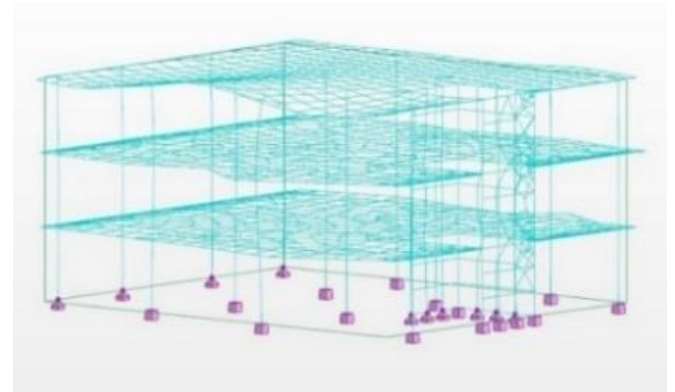
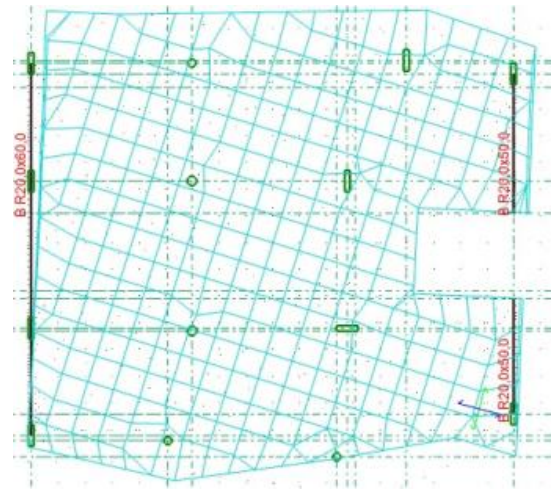


Fig 18. 1st vibration mode of the structure (Source: adapted from Robot by the Author,2024)

3.2. Maximum Displacements of the Structure

The results of the modal analysis below show that the maximum displacements are between 1.7 and 1.9 centimetres as indicated in Table 14. It is worth noting that the maximum displacements are calculated in each direction.

Table 14. Values of maximum displacement of the structure under study (Source: adapted from Robot by the Author, 2024)

Maximum displacements (cm)						
Case	X Direction			Y Direction		
	q	U_{proj}	U_{Fin}	q	U_{proj}	U_{Fin}
1	3.0	0.10	0.30	3.0	0.10	0.30
2	3.0	0.33	1.00	3.0	0.33	1.00
3	3.0	0.40	1.20	3.0	0.40	1.20
4	3.0	0.13	0.40	3.0	0.13	0.40
5	3.0	0.40	1.20	3.0	0.57	1.70
6	3.0	0.23	0.70	3.0	0.33	1.00
7	3.0	0.43	1.30	3.0	0.63	1.90

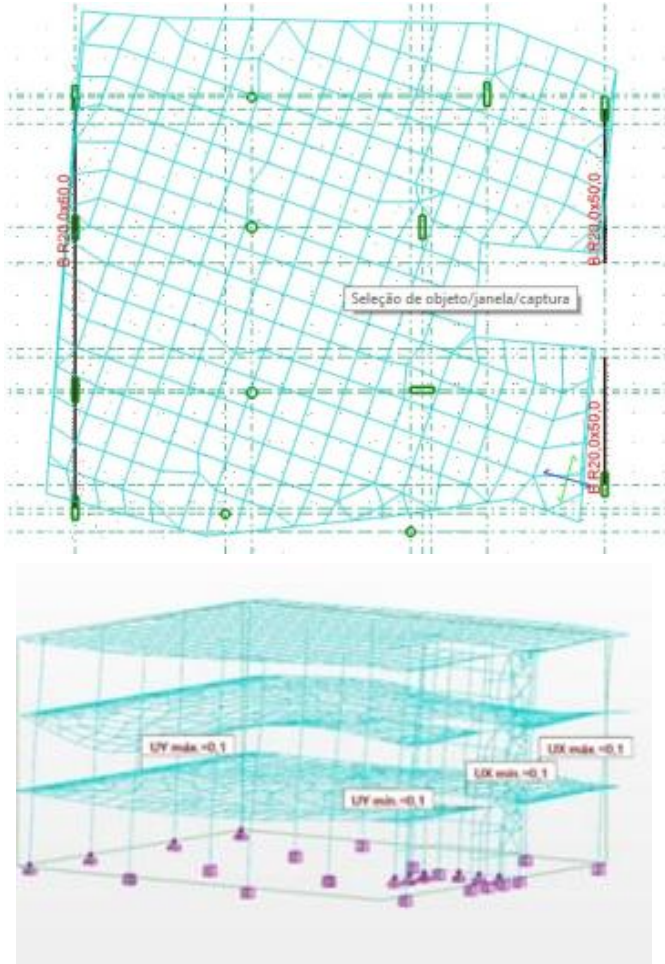


Fig 19. 2nd vibration mode of the structure (Source: adapted from Robot by the Author, 2024)

3.3. Basal Shear of the Structure

To assess the basal cut values, the seismic combinations were analyzed in each direction, to verify the basal cut values by spectral acceleration in all directions. It should be noted that the period used to calculate the shear force at the base was 0.81s, which corresponds to the 3rd vibration mode of the structure, since this of the three modes considered presents the most unfavorable frequency, thus constituting the perfect simulation for calculating the basal shear force as presented in Table 15.

Table 15. Basal shear force values (Source: adapted from Robot by the Author, 2024)

Shear base	Basal shear force (kN)	Seismic coefficient (β)
X Direction earthquake	1,423.00	0.127
Y Direction earthquake	1,282.00	0.115

3.4. Relative Displacements between Floors (Drift) of the Structure

Regarding the relative displacements between floors of the structure in the X and Y directions, these were calculated to comply with the criteria prescribed in regulation EC8, for the control of the limitation of the damage presented in Table 16. It should be noted that this was calculated considering the

earthquake with the shortest return period, that is, the conditioning earthquake.

Table 16. Drift between floors of the structure (Source: adapted from Robot by the Author, 2024)

Floor	Relative displacements (cm)					
	X Direction			Y Direction		
	v	h	d_r	v	h	d_r
Ground floor	0.55	3.05	0.28	0.55	3.05	0.28
1st Floor	0.55	6.10	0.55	0.55	6.10	0.55
2nd Floor	0.55	9.15	0.83	0.55	9.15	0.83

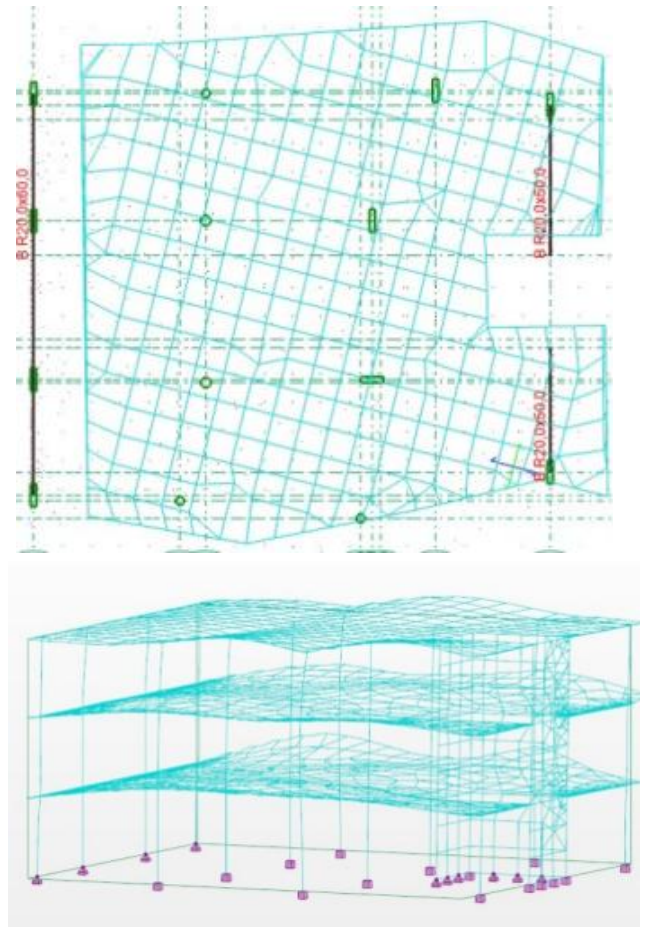


Fig 20. 3rd vibration mode of the structure (Source: adapted from Robot by the Author, 2024)

3.5. Second Order Effects

There is no need to check for second-order effects in the structure since the sensitivity coefficient to relative displacement between floors (θ) is less than or equal to 0.10.

3.6. Earthquake Conditioning

The structure under study is rigid and has a small number of floors and, as verified, the structure has high frequencies and low periods, which causes the structure to vibrate faster. Because of this, the structure tends to be more conditioned by type II earthquakes, also known as near-earthquakes, since they predominantly have higher frequencies.

Table 13. Frequencies, Modal Periods and Modal Participation Factors of the Structure under Study

Case/Mode	Frequency (Hz)	Period(s)	RUX (%)	RUY (%)	CUX (%)	CUY (%)	Total mass Ux (t)	Total mass Uy (t)
40/1	0.91	1.10	86.06	5.50	86.06	5.50	1117.28	1117.28
40/2	0.95	1.05	96.83	75.63	10.77	70.13	1117.28	1117.28
40/3	1.23	0.81	98.27	98.74	1.44	23.12	1117.28	1117.28
40/4	4.25	0.24	99.37	98.95	1.10	0.20	1117.28	1117.28
40/5	4.55	0.22	99.81	99.74	0.44	0.79	1117.28	1117.28
40/6	6.26	0.16	99.85	99.92	0.03	0.18	1117.28	1117.28

Where:

CUX – represents the modal participation of the structure's rotation in the x direction;

CUY – represents the modal participation of the structure's rotation in the y direction.

RUX – represents the modal participation of translation of the structure in the x direction;

RUY – represents the modal participation of translation of the structure in the y direction

Therefore, when the fundamental frequency of the building tends to equal the frequency of the earthquake, a phenomenon called resonance occurs, where the vibrations amplify the effect of the earthquake on the structure.

3.7. Evaluation of Results

After performing the structural seismic analysis of the building under study, it was found that it meets the EC8 criteria, regarding the minimum number of modes considered in the analysis ($k = 6 \geq k_{min} = 6$) and the vibration period of the last mode, which is less than ($T_6 = 0.16s \leq 0.20s$), therefore the modal analysis can be considered valid, and the modes considered present a significant contribution since the sum of the effective modal masses is greater than 90% of the global mass of the structure and all modal masses are greater than 5% of the structure.

Furthermore, this structural system can be defined as non-resistant, that is, not stable, although it is not subject to drastic translational deformations in x and y, and torsion. As stated, the first three modes were crucially evaluated because they are decisive in characterizing the deformation mode of the structure under study. After this analysis, it was found that the structure does not respond satisfactorily to the displacements imposed by the action of earthquakes. Due to the torsion effect observed in the first vibration mode, the first two vibration modes must be characterized by a translational movement, thus compromising the structural seismic resistance of the building under study.

The translation in x observed in the 2nd vibration mode is also, in a certain way, crucial to the seismic response of the building, due to the unfavourable arrangement of the walls, since 90% of them are arranged in the same direction, which means that the structure is favourable to the translational movements in Y observed in the third vibration mode. Faced with this dilemma, in this case, the translation in X, an in-situ solution is occasionally found, which is the existence of neighbouring infrastructures protecting the structure against seismic action in this direction.

4. Conclusions

- The primary purpose of this study was to conduct a comprehensive seismic analysis of a three-story reinforced concrete building to assess its vulnerability and structural integrity under earthquake conditions, ensuring safety and resilience in seismically active regions.

- The building displayed high frequencies and low periods across vibration modes, indicating a tendency for rapid vibration under seismic action. It was found to be more influenced by Type II (high-frequency) earthquakes, which led to torsional displacement in the 1st mode (86.06%) and translational displacements in the X (96.83%) and Y directions (98.74%) for the 2nd and 3rd modes, respectively.
- While the building met basic EC8 criteria for seismic analysis (i.e., six vibration modes considered and a final mode period of 0.16s), several structural vulnerabilities were observed. Wall orientations contributed to heightened translational movements, especially in the X direction (90% of walls oriented along X). Torsion was dominant in the 1st mode, indicating a need for adjustments to improve seismic resilience in similar structures.
- The Maximum displacements were between 1.7 cm and 1.9 cm in the X and Y directions, underscoring areas of concern under seismic forces. The basal shear force reached 1,423 kN in the X direction and 1,282 kN in the Y direction, with a seismic coefficient of 0.127 and 0.115, respectively, which aligns with the most critical seismic mode at a period of 0.81s.

Recommendations and Future Prospects:

- Given Mozambique's seismic risk areas, especially in Maputo, Beira, and Rift Valley provinces (Niassa, Sofala, Manica, Tete, Inhambane, and Gaza), there is a dire need for Localized Seismic Standards to allow structures to better withstand regional seismic events based on accurate local data. Development of national standards could address specific site conditions, while parametric studies would help correlate local seismic characteristics with those in other standards like Eurocode 8.
- For new buildings in seismically active regions, recommendations include a diverse wall arrangement to distribute seismic forces evenly, incorporation of cross-walls to enhance stiffness and stability, use of advanced modeling techniques and nonlinear analysis for detailed structural behavior assessment, implementation of deep foundations and consideration of soil-structure interaction, and regular structural inspections and seismic retrofitting as necessary. These measures aim to improve the seismic resilience of new constructions and ensure their safety and integrity.

- Establishing a national seismic observatory could provide Mozambique with independent seismic data collection, promote research into localized seismic design approaches and minimize losses.
- Future research should consider the assessment of structural responses across different building geometries and soil types to establish best practices. Furthermore, the evaluation of the effectiveness of traditional construction practices concerning seismic resistance in Mozambique, as well as the investigation of the relationship between disorderly urban development and seismic vulnerability should also be explored.

Acknowledgement

This study was supported by Faculdade de engenharias, arquitectura e planeamento físico, Universidade Wutivi (UniTiva).

Conflict of Interest Statement

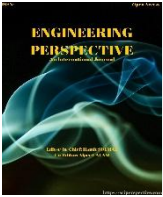
The authors declare that there is no conflict of interest in the study.

Credit Author Statement

Edson da Graça M. Cumbe: Conceptualization, Methodology, Visualization, Writing - original draft, Writing - Review & Editing.
Angelo A. Pascoal: Conceptualization, Methodology, Visualization, Writing - original draft, Writing - Review & Editing.
Valdemar Fulano: Supervision, Methodology
Philemon Niyogakiza: Writing - Review & Editing.
Marc Nshimiyimana: Review & Editing.
Domingos do Rosário N. João: Review & Editing.
Yenezzer Genene Haile: Review & Editing

References

1. Silva, J. P. (2010). Avaliação do comportamento sísmico de edifícios de betão armado dimensionados pelo EC 8. Porto: Universidade de Porto.
2. Sousa, P. J. A. (2006). Avaliação de perigosidade sísmica e segurança estrutural em Moçambique: os casos da Beira e do Chimoio. Porto: Universidade de Porto.
3. Fonseca, E. (2010). Avaliação de Risco Sísmico e Planeamento de Emergência em Moçambique. Niterói: Universidade Federal Fluminense.
4. Amaral, D. d. (2014). Dimensionamento de um Edifício em Betão Armado. Viseu: Instituto Superior de Viseu.
5. WHO. (2024). World Health Organization. Retrieved from WHO: <https://www.who.int>
6. USGS. (2024). United States Geological Survey. Retrieved from USGS: <https://www.earthquake.usgs.gov>
7. Testino, G. (2023). Análise Sísmica e Modelação de Edifícios de Betão Armado de acordo com a Regulamentação Portuguesa e Italiana. Lisboa: Instituto Superior de Engenharia de Lisboa.
8. Samboco, V. (2010). Sismicidade De Moçambique. Brasília: Direcção Nacional de Geologia (DNG).
9. Peña, L. A., & Doz, G. (2012). Análise dos Efeitos Provocados por Abalos Sísmicos em Estruturas Irregulares. Brasília: Universidade de Brasília.
10. Lousa, R. F. (2017). Avaliação da Resistência Sísmica de um Edifício de Betão. Lisboa: Instituto Superior Técnico de Lisboa.
11. Lopes, H. M. (2007). Comparação do Eurocódigo 8 com o RSA/REBAP Dimensionamento Sísmico de Estruturas de Betão Armado. Lisboa: Universidade Técnica de Lisboa.
12. Horner-Johnson, B. C., Gordon, R. G., Cowles, S. M., & Argus, D. F. (2005). The angular velocity of Nubia relative to Somalia and the location of the Nubia—Somalia—Antarctica triple junction. *Geophysical Journal International*, 162(1), 221-238. <https://doi.org/10.1111/j.1365-246X.2005.02608.x>
13. Geocontrole. (2021). Relatório Geotécnico do UNICEF Office - General Arrangement Foundations and Ground Floor Plans. Maputo: ArkTek, Lda.
14. Fragoso, M. R., & Barros, M. J. (2005). Espectros de Resposta de Movimentos Sísmicos. Açores: Universidade dos Açores.
15. Eurocode-8. (2004). Design of Structures for Earthquake Resistance - Part 1. CEN.
16. Eurocode-2. (2004). Design of Concrete Structures. CEN.
17. Eurocode-1. (2002). Actions on Structures - Part 1. CEN.
18. Eurocode-0. (2002). Basis of Structural Design. CEN.
19. Claudino, T. M., & Silva, N. P. (2023). Sismos: Breve Abordagem Teórica sobre sua Ação sobre Estruturas, Controle das Vibrações e Dispositivos de Controle Passivos. Rio Grande: Universidade Federal do Rio Grande (FURG).
20. Bule, H. S. (2023). Revisão do Dimensionamento Estrutural de uma Moradia Unifamiliar em Laulane. Maputo: Universidade Eduardo Mondlane.
21. Baker, J. K. (2015). Introduction to Probabilistic Seismic Hazard Analysis. New York: White Paper Version 2.1.



The Effect of Welding Wire Feed Speed on Weld Bead Penetration, Length and Width in Robotic Gas Metal Arc Welding

Mustafa Yazar¹ , Hilal Kır^{2*} , Şükrü Talaş³ 

¹ R&D Department, Şahinkul Machine and Spare Parts Manufacturing Co. Ltd., Bursa, Türkiye

² Department of Mechanical Engineering, Faculty of Engineering, Bursa Uludağ University, Bursa, Türkiye

³ Department of Metallurgical and Materials Engineering, Faculty of Technology, Afyon Kocatepe University, Afyonkarahisar, Türkiye

ABSTRACT

In this study, the effect of welding wire feed speed on penetration quality in the gas metal arc welding method (GMAW), which is widely used in the automotive industry, was investigated in terms of product safety and quality. In the gas metal arc welding robots used in automotive production, the welding process is carried out through communication between the robot and the gas metal arc welding machine within predetermined parameters. In the study, 3 mm thick 6224 ERD steel was used and overlap welding was applied for experimental analysis. Among the gas metal arc welding parameters, welding current, wire diameter, and gas flow rate were kept constant, while wire feed speed was considered as the only variable. Starting from 2 m/min, the welding wire feed speed was increased by 2 m/min in each test, reaching up to 12 m/min, resulting in a total of 6 different experiments. The test results were evaluated based on metallographic analyses to determine the macro and microstructures of the welds. According to the findings, it was observed that penetration increased as the welding wire feed speed increased. However, it was also determined that beyond a certain optimum value, the increased welding speed had a negative effect on weld bead width and length. Accordingly, the optimum welding wire feed speed was suggested for achieving the appropriate penetration and maintaining weld quality.

Keywords: Robotic arc welding; penetration; welding wire feed speed

History

Received: 28.03.2025

Revised : 08.05.2025

Accepted: 03.06.2025

Author Contacts : mustafa.yazar@sahinkulmakina.com.tr, hilalkir16@gmail.com, stalas@aku.edu.tr

Cite this paper: Yazar, M., Kır, H., Talaş, T., (2025). The Effect of Welding Wire Feed Speed on Weld Bead Penetration, Length and Width in Robotic Gas Metal Arc Welding. Engineering Perspective, 5 (2), 85-89.

<http://dx.doi.org/10.29228/eng.pers.81420>

*Corresponding Author

1. Introduction

The continuous growth of the global population has led to a substantial increase in energy demand [1]. This situation has intensified competition among companies and generated a strong expectation for manufacturing methods that simultaneously offer high quality and low production costs. The utilisation of robots in gas welding has become pervasive to enhance customer satisfaction and ensure product quality. To mitigate human-related errors, gas welding operations are increasingly conducted with a robot serving as the carrier. This method is favoured by manufacturers seeking to produce welds that are free of errors, while maintaining minimal production time and maintaining product quality at a certain level [2-4]. The effect of wire feed speed on weld penetration depth in GMAW welding has been demonstrated to be significant for many types of metallic materials. As the wire feed speed increases, the welding current also increases in the constant voltage weld supply

systems, which in turn increases the heat input and weld penetration depth [5-8]. However, this relationship between wire feed rate and penetration and also weld current may not be linear. At elevated wire feed speeds, the collective travel speed necessary to sustain a stable weld pool can counteract some of the benefits gained from elevated current values. Furthermore, the arc becomes more constricted at higher wire feed speeds, which can marginally reduce penetration due to reduced amount of heat input into the weld pool of which its average temperature between the center and the edge of the weld pool is considerably different; a condition of high cooling rate due to small volume of weld pool [9-12]. Higher wire speeds can result in a more constricted arc, which can slightly reduce penetration and lowering wire speed can be advantageous for specific joints, such as outside corners, to prevent excessive penetration and regulate the weld profile. In addition, it can be concluded that wire feed speed is one of the most significant factors controlling weld penetration in GMAW welding. While increasing wire feed speed does indeed

increase penetration, the relationship is complex and further factors, such as travel speed, must be considered. Adjusting wire feed speed is a key method by which welders can control and optimize weld penetration [13-16, 17]. Wire feed speed is one of the most important factors controlling weld penetration, but its effect is complex and interactive with welding speed. Increasing wire speed leads to increased penetration, but at very high speeds, faster travel becomes necessary, which can counteract this gain. It is therefore essential for welders to adjust both parameters to optimize weld penetration for each specific welding application [5, 18-21].

In this study, the effect of welding wire feed speed on penetration was investigated by overlap welding with 3 mm thick 6224 ERD steel on a gas metal arc welding robot. The weld wire feed rate was chosen between 2 m/min and 12 m/min. Metallographic investigation was carried out for determining the penetration and weld macro and microstructures.

2. Materials and Methods

2.1 Material

2.1.1 6224 ERD steel sheet material, SG2 welding wire and shielding gas

The chemical composition of the 3 mm thick uncoated commercial 6224 ERD steel used in the experiments is shown in Table 1 and its mechanical properties are shown in Table 2.

Table 1. Chemical content of 3 mm 6224 ERD steel sheet (wt. %).

C	P	S	Mn	Al
0,07	0,015	0,015	0,35	0,02

Table 2. Mechanical properties of 3 mm thick 6224 ERD sheet metal

Yield Stress (MPa)	170
Tensile Stress (MPa)	400
Elongation (%)	33

SG2 quality 1 mm welding wire was used as the welding wire and its chemical composition is shown in Table 3 and mechanical properties are shown in Table 4.

Table 3. Chemical composition of SG2 (1 mm) welding wire (wt.%).

C	Si	Mn	P	S
0,06	0,41	1,1	0,012	0,011

Table 4. Mechanical properties of SG2 (1 mm) welding wire.

Yield Stress (MPa)	430
Tensile Stress (MPa)	540
Elongation (%)	28
Temperature (°C)	-29
Impact Toughness (J)	70

Tests were conducted with Manifold 205 mixture gas, which is frequently used in industry as a protective gas. The composition properties of the mixture gas are given in Table 5.

Table 5. Gas mixture content of HB 205 standard shield gas (vol. %).

	Ar	CO ₂	O ₂
HB 205	93	5	2

By keeping the current constant in the gas welding robot and increasing the welding wire feed speed from 2 m/min to 12 m/min, 6 overlap welds were made and the test pieces were prepared for measuring penetration and microstructural examination.

2.2 Overlap welding with gas welding robot

In this study, an ABB brand robot was integrated with a Fronius TransPuls Synergic 4000 brand MIG welding machine for the welding process. SG2 welding wire was used as the welding wire in this study. Figure 1 shows an image of the MIG welding robot machine. Ensuring that the wire feed speed works with the correct parameters will reduce the consumption of consumable materials such as the contact nozzle. After measuring the gas flow, the welding gas flow was not reduced below 10 litres per minute to prevent welding porosity and ensure penetration. Although gas flow, weld current value and surface cleanliness affect the end result, many variables affecting weld quality, only the wire feed speed was changed. During the test, these variables were kept under control. A Tronic Xjl-17 inverted trinocular metallographic microscope was used for penetration and microstructure images. The robotic GMAW welding operation was performed with six test specimens using the values given in Table 6. The current intensity was kept constant, and the wire feed speed was increased to 2 meters per minute on each part.



Figure 1. Welding robot used in this study

Table 6. Test parameters of weld process

Specimen	Current (A)	Wire feed speed (m/min)	Wire Diameter (mm)	Gas Flow Rate (lt/min)
1. test specimen	135	2	1	10
2. test specimen	135	4	1	10
3. test specimen	135	6	1	10
4. test specimen	135	8	1	10
5. test specimen	135	10	1	10
6. test specimen	135	12	1	10

3. Results and Discussions

3.1 Weld bead properties and penetration

The measured results of the welded bead widths of parts obtained

by welding the test samples at different wire feed speeds are shown graphically in Figure 2. As can be seen from the effect of the wire feed speeds, the weld width increases as the amount of weld wire is purged into the weld pool increases i.e. due to the accumulated weld metal volume. The increase in the feeding rate also means there is more weld metal pool volume and hence, the increase in the weld width with the amount of weld metal positively affects the heat input with respect to higher average weld pool temperature [2, 3]. This is related to the frequency of deposition of hot liquid weld metal that is present in the weld zone during the welding process. As the deposition rate increases the average weld pool temperature increases and the heat input is raised due to the elevated number of droplets of liquid metal per unit time. On the other hand, the weld lengths are generally similar as oppose to the weld bead width [17, 19, 21]. The increase in the weld bead width is compensated with weld bead lengths with respect to the wire feed speed which are given in Figure 3.

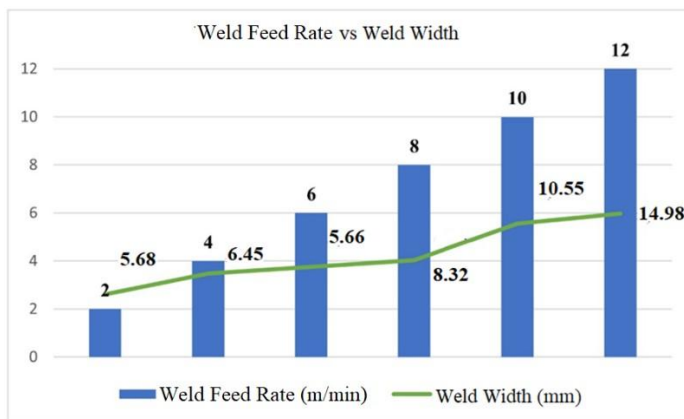


Figure 2. Weld bead width with respect to wire feed speed

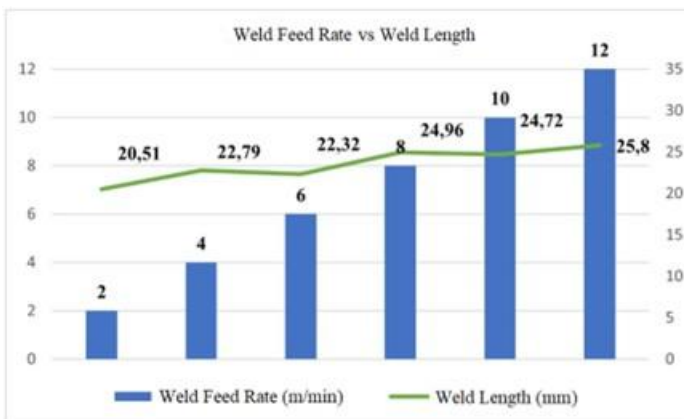


Figure 3. Weld bead length with respect to wire feed speed

After the welding process, the penetration depths were measured and the results are given in Figure 4. According to the results of the tests, the weld width increased as the welding wire feed speed increased. According to the welding image given in Test specimen Figure 5, it is seen that the optimum value of the welding wire feed speed is 10 m/min, and the curve in the graph in Figure 2 shows this. The weld length measurements also give the same result, and the appropriate welding image is obtained at a welding wire feed speed of 10 m/min. After the test process, the penetration depths were measured and the results are given in Figure 4.

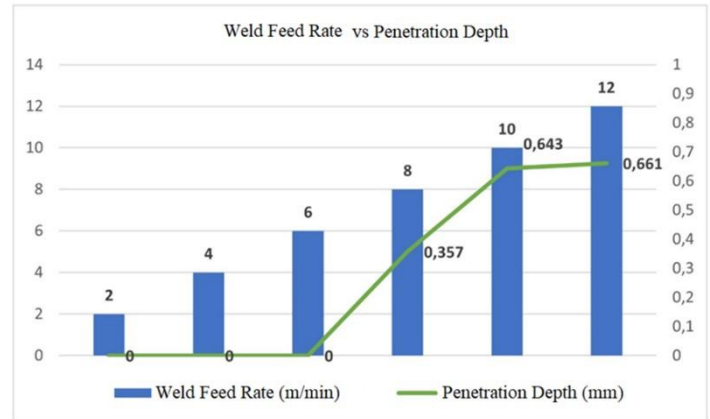


Figure 4. Penetration depths with respect to wire feed rate

As demonstrated in Figure 5, the macro images of the weld seam according to the welding wire feed speed are as follows: at a low welding wire feed rate, the weld seam was found to be spattered and narrow, with an absence of fusion or penetration defects at the edges; conversely, at welding feed rates of 4 m/min and above, the welds were smooth in appearance and exhibited minimal slag formation on the weld seam. The penetration depth desired by the main customer has reached the optimum value at the welding wire feed speed of 10 m/min, and the penetration depth increases as the welding wire feed speed increases. The penetration depth of 2, 4, 6 m/min was found to be unsuitable in the tests conducted for the production purposes. It is noteworthy that the width of the weld end crater increases with increasing welding wire feed speed, reaching a maximum at a wire feed speed of 12 m/min. This phenomenon can be attributed to the rise in the average temperature of the weld seam. The increase in the amount of molten metal, which is caused by an increase in the amount of welding wire rate, results in an increase in the temperature of the weld pool. This, in turn, as seen in Figure 5, leads to an increase in the length of the weld crater [3]. As illustrated in Table 10, a clear correlation emerges between the dimensions of weld bead craters and their length. The width-to-length ratio appears to be increasing dramatically above a wire feed speed of 8 m/min, from 0.277 to 0.581 ratio, which is almost double of the original the former value. The crater width-to-length ratio is also significant when compared to the weld bead width-to-length ratio, which records a dramatic jump from 0.312 to 0.579 ratio.

Weld penetration in GMAW welding is significantly influenced by wire feeding speed, as it directly affects the amperage and, consequently, the heat input into the weld. Wire feed rate controls the amount of wire fed into the arc, which in turn determines the weld current flow characteristics. Higher current flow generally results in greater heat input and deeper penetration [2, 5, 6]. While faster wire feed speeds increase amperage and potentially penetration, they may be offset by the faster travel speeds, increasing penetration effect because less time is spent heating any one area [2, 6, 12]. As the weld travel speed is constant in this study, the heating effect is elevated in favour of higher weld pool temperature and therefore larger weld pool size at higher weld wire feed rate.

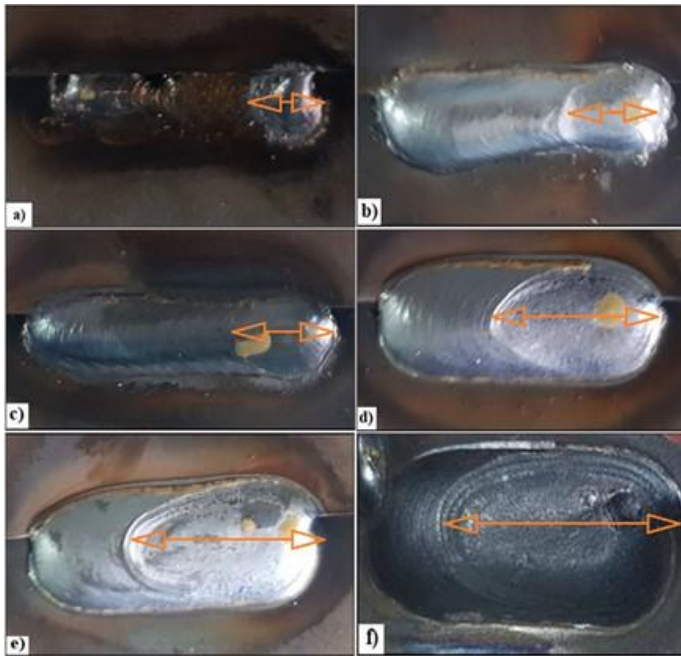


Figure 5. Appearance of GMAW weld beads deposited at different weld wire feed rates, a) 2 m/min, b) 4 m/min, c) 6 m/min, d) 8 m/min e) 10 m/min f) 12 m/min.

A well-penetrated weld typically exhibits optimal tie-in at the weld edges and a flat bead profile, whereas insufficient penetration may result in a narrow, convex bead. The relationship between welding speed and penetration depth is inversely proportional; as welding speed increases, penetration depth decreases due to several factors [4, 17, 19]. Faster welding speeds result in reduced time for the arc to heat a specific area, leading to decreased heat input and shallower penetration. Increased travel speeds result in the weld pool solidifying more rapidly, leading to reduced weld bead width and less time available for penetration. Conversely, slower speeds allow for deeper weld pools to form due to increased time for the base material to melt by absorbing more heat due to heat transfer restrictions in large weld pool volumes. However, slower speeds can also result in improved penetration due to more time for heat to penetrate the metal. However, excessively slow speeds can lead to increased spatter and other defects [19-21]. In summary, increased wire feeding rate results in decreased penetration depth due to reduced heat input and smaller weld pool size, whilst decreased wire feeding speed leads to increased penetration depth due to increased heat input and longer solidification time. The weld length exhibited minimal change with increasing welding wire feed rate, attributable to the constant welding feed rate. However, while no change is expected, the expansion of the weld deposition and the enlargement of the crater due to the effect of the weld heat input indicate that the weld is expanding forward or melting of the front of weld pool during the welding process [3, 13, 21].

As shown in Figure 6, the penetration depths of macrostructures are contingent upon the welding wire feed rate. The analysis of these macrostructures reveals that optimal weld penetration is achieved at weld wire feed rates of 10 m/min and 12 m/min. In contrast, the weld seam appearance at 2, 4, and 6 m/min wire feed rates exhibits minimal penetration, while welds at 8 m/min and above demonstrate substantial penetration. The penetration in the welding process is

usually directly related to the heat input, which can be related to the welding wire diameter, welding travel speed and wire feed rate, welding current and arc distance in wire fed systems [3, 4, 11, 14]. As a result of the examination of the macrostructure pictures, the amount of melting in the base metal can be easily seen. While the melting of the base metal is evident at rates exceeding 6 m/min, it is more pronounced at welding wire feed rates of 10 m/min and 12 m/min. The melting of base metal is also important in assessing the success of the weld bead. It is noticeable that the melting of upper sheet is not achieved until 8 m/min wire feed rate and the edges of upper sheet metal just under the weld bead disappears at 10 and 12 m/min wire feed rates successfully.

Table 7. The widths (W), lengths (L) and Crater Length (CL) of weld beads with respect to wire feed rate and relevant correlations between W, L and CL values (in mm) .

Wire feed rate (m/min)	Width (W)	Length (L)	Crater Length (CL)	W/L
2	5.68	20.51	6.4	0.277
4	6.45	22.79	6.73	0.283
6	5.66	22.32	7.21	0.254
8	8.32	24.96	12.25	0.333
10	10.55	24.72	13.32	0.427
12	14.98	25.8	14.94	0.581

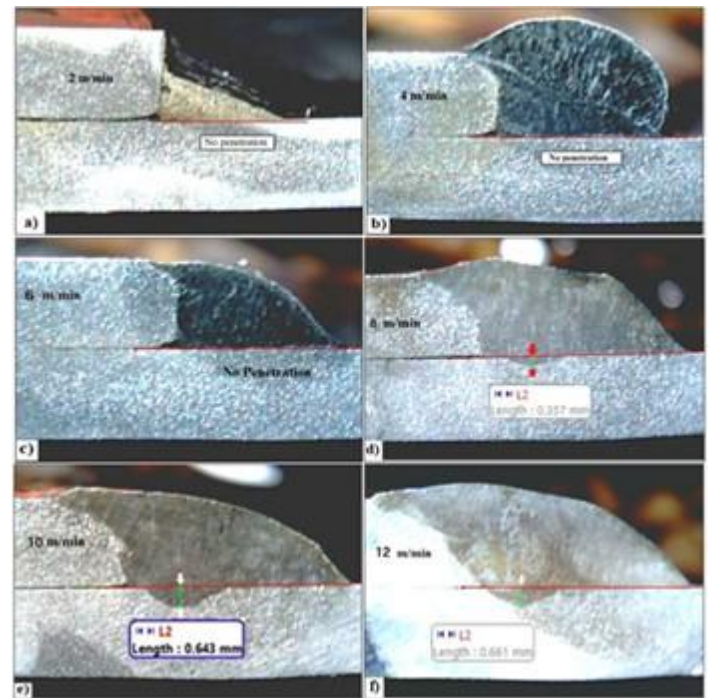


Figure 6. Cross-sectional macrostructures of GMAW weld beads deposited at different welding wire feed rates, a) 2 m/min, b) 4 m/min, c) 6 m/min, d) 8 m/min e) 10 m/min f) 12 m/min

4. Conclusions

The following general results were obtained in this study:

1. The penetration results of robotic welded seams at welding wire feed rates of 2, 4, 6, 10 and 12 m/min show that the optimal wire feed rate is 10 m/min and the critical rate is 8 m/min.
2. As the welding wire feed speed increases, the dimensions of the

weld pool crater resulting from the mostly solidification, also change. With increasing welding wire feed rate, the weld pool solidification crater dimensions increase.

3. It is hypothesised that the formation of a large weld crater as a result of the accumulation of a large amount of weld metal with high welding wire feed rate is due to the high average temperature of the weld pool.

4. The large weld pool crater further underscores the correlation between weld heat input and weld pool temperature.

5. The weld pool width is believed to be associated with the increasing quantity of liquid metal droplets.

6. The weld length exhibited minimal change with increasing welding wire feed rate, attributable to the constant welding feed rate. However, while no change is expected, the expansion of the weld deposition and the enlargement of the crater due to the effect of the weld heat input indicate that the weld is expanding forward or melting of the front of weld pool during the welding process.

Acknowledgment

This study was supported by Şahinkul Machinery with the project number ARGE-2024-042 24ARG00002 Thanks to Ergin VERİM and Erhan MUHTAR for technical support.

Conflict of Interest Statement

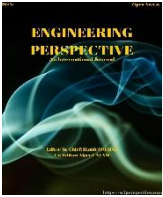
The authors must declare that there is no conflict of interest in the study.

CRediT Author Statement

Mustafa Yazar: Investigation, Project administration, Resources, Writing – original draft **Hilal Kır:** Investigation, Writing – review & editing **Şükrü Talaş:** Conceptualization, Formal analysis, Supervision, Methodology

References

- Dam, Q.T., Haidar, F., Mama, N., Chennapalli, S. J. (2024). Modeling and simulation of an Internal Combustion Engine using Hydrogen: A MATLAB implementation approach. *Engineering Perspective*. 4 (3). 108-118. <http://dx.doi.org/10.29228/eng.pers.76219>
- Zhao, D., Bezgans, Y., Vdonin, N., Radionova, L., Bykov, V. (2021). Modeling and Optimization of Weld Bead Profile with Varied Welding Stages for Weathering Steel A606. *International Journal of advanced Manufacturing Technology*. Volume 116. pages 3179–3192. <https://doi.org/10.1007/s00170-021-07722-y>
- Lancaster, J. F. (1999) *Metallurgy of Welding*. Woodhead publishing. ISBN: 978-1-85573-428-9
- Lertora, E., Gambaro, C., & Cypres, P. (2011). The influence of robotic MAG process welding parameters. *Welding International*. 25(10). 767–776. <https://doi.org/10.1080/09507116.2011.581349>
- Mills, K. C., & Keene, B. J. (1990). Factors affecting variable weld penetration. *International Materials Reviews*. 35(1). 185–216. <https://doi.org/10.1179/095066090790323966>
- Kim, I.S., Son, J.S., Kim, I.G., Kim, J.Y., Kim, O.S. (2003). A study on relationship between process variables and bead penetration for robotic CO2 arc welding. *Journal of Materials Processing Technology*. 136(1–3). 139–145. [https://doi.org/10.1016/S0924-0136\(02\)01126-3](https://doi.org/10.1016/S0924-0136(02)01126-3)
- Wu, Y., Kovacevic, R. (2002). Mechanical assisted droplet transfer process in gas metal arc welding. *Proceedings of the Institution of Mechanical Engineers, Part B: Journal of Engineering Manufacture*. 216(4). 555–564. <https://doi.org/10.1243/0954405021520247>
- Katayama, S., Kawahito, Y., Mizutani, M. (2010). Elucidation of laser welding phenomena and factors affecting weld penetration and welding defects. *Physics Procedia*. 5(Part B). 9–17. <https://doi.org/10.1016/j.phpro.2010.08.024>
- Li, K., Wu, Z.S., Liu, C.R., Chen, F.H. (2014). Arc characteristics of submerged arc welding with stainless steel wire. *International Journal of Minerals, Metallurgy, and Materials*. 21(8). 772–778. <https://doi.org/10.1007/s12613-014-0970-1>
- Li, X.R., Zhang, Y.M., Kvidahl, L. (2013). Penetration Depth Monitoring and Control in Submerged Arc Welding. *Welding Journal Research Supplement*. 92. 48s-56s.
- Ibrahim, I.A., Mohamat, S.A., Amir, A., Ghalib, A. (2012). The effect of gas metal arc welding (GMAW) processes on different welding parameters. *Procedia Engineering*. 41. 1502–1506. <https://doi.org/10.1016/j.proeng.2012.07.342>
- Roshan, R., Kumar Naik, A., Kumar Saxena, K., Arora, K. S., Shajan, N., Msomi, V., & Mehdi, H. (2023). Effect of welding speed and wire feed rate on arc characteristics, weld bead and microstructure in standard and pulsed gas metal arc welding. *Journal of Adhesion Science and Technology*. 37(23). 3297–3314. <https://doi.org/10.1080/01694243.2023.2192314>
- Suban, M., Tušek, J. (2001). Dependence of melting rate in MIG/MAG welding on type of shielding gas. *Journal of Materials Processing Technology*. 119(1-3). 185–192. [https://doi.org/10.1016/S0924-0136\(01\)00940-2](https://doi.org/10.1016/S0924-0136(01)00940-2)
- Praveen, P., Yarlagadda, P.K.D.V., Kang, M.J. (2005). Advancements in pulse gas metal arc welding. *Journal of Materials Processing Technology*. 164–165. 1113–1119. <https://doi.org/10.1016/j.jmatprotec.2005.02.100>
- Wang, J., Sun, Q., Ma, J., Jin, P., Sun, T., Feng, J. (2018). Correlation between wire feed speed and external mechanical constraint for enhanced process stability in underwater wet flux-cored arc welding. *Proceedings of the Institution of Mechanical Engineers, Part B: Journal of Engineering Manufacture*. 233(10). 2061–2073. <https://doi.org/10.1177/0954405418811783>
- Karadeniz, E., Ozsarac, U., & Yildiz, C. (2007). The effect of process parameters on penetration in gas metal arc welding processes. *Materials & Design*. 28(2), 649–656. <https://doi.org/10.1016/j.matdes.2005.07.014>
- Deshmukh, A.R., Venkatachalam, G., Divekar, H., Saraf, M.R.(2014). Effect Of Weld Penetration On Fatigue Life. *Procedia Engineering*. 97. 783 – 789. <https://doi.org/10.1016/j.proeng.2014.12.277>
- J. Tušek (2002). Factors Affecting Weld Shape in Welding With A Triple-Wire Electrode. *Metallurgija*. 2. 89-92.
- Mills, K. C., & Keene, B. J. (1990). Factors affecting variable weld penetration. *International Materials Reviews*. 35(1), 185–216. <https://doi.org/10.1179/095066090790323966>
- Lee, K-B., Kim, C., Kim, D-S. (2013). High deposition rate pulse gas metal arc welding for Al 5083 thick plate. *Proceedings of the Institution of Mechanical Engineers, Part B: Journal of Engineering Manufacture*. 227(6).848-854. <https://doi.org/10.1177/0954405413476860>
- Kozakov, R., Schöpp, H., Gött, G., Sperl, A., Wilhelm, G., & Uhrandt, D. (2013). Weld pool temperatures of steel S235 while applying a controlled short-circuit gas metal arc welding process and various shielding gases. *Journal of Physics D: Applied Physics*, 46(47), 475501. <https://doi.org/10.1088/0022-3727/46/47/475501>



Comparative Analysis of Road Safety Performance In Sub-Saharan African Countries Using Road Safety Performance Index

Jean Claude Sugira^{1*} , Jean de Dieu Ninteretse^{2*} , Marc Nshimiyimana³ , Philemon Niyogakiza⁴

¹ School of Transportation Engineering of Southeast University, Nanjing, China

² School of Civil Engineering /Southeast University, Nanjing,210096, China

³ Institute of Rock and Soil Mechanics, Chinese Academy of Sciences, Wuhan 430071, China

⁴ School of Civil Engineering of Southeast University, Nanjing China

ABSTRACT

Road traffic accidents claim approximately 1.25 million lives globally each year, with low- and middle-income countries bearing over 90% of these fatalities despite accounting for only 48% of the world's registered vehicles. Sub-Saharan Africa, in particular, faces severe road safety challenges due to inadequate infrastructure, weak enforcement of traffic laws, and rapid urbanization. This study introduces the Road Safety Performance Index (RSPI), a comprehensive composite index comprising 13 key indicators, to evaluate and compare road safety performance across 20 Sub-Saharan African countries. Using 2020 data from reputable sources such as the World Bank, government reports, and academic publications, the study employs multiple regression analysis to identify critical factors influencing road safety outcomes.

The results reveal significant disparities in road safety performance across the region. Mauritania emerged as the top performer with an RSPI score of 92.03, excelling in areas such as traffic law enforcement and road infrastructure quality. Conversely, Ethiopia and Nigeria demonstrated notable opportunities for improvement, particularly in traffic safety law enforcement and pedestrian safety measures. Key factors influencing road safety performance include urbanization rates, GDP per capita, alcohol consumption, and the quality of road infrastructure.

The RSPI provides a robust framework for policymakers and stakeholders to prioritize targeted interventions, allocate resources effectively, and foster cross-country knowledge exchange. By addressing critical challenges such as poor road infrastructure, distracted driving, and urban traffic congestion, Sub-Saharan African countries can significantly reduce road traffic accidents, injuries, and fatalities. This study contributes to the growing body of knowledge on road safety in low- and middle-income countries and underscores the importance of evidence-based strategies to create safer and more sustainable transportation systems.

Keywords: Composite index; fatalities; policy interventions; road safety performance; Sub-Saharan Africa; traffic accidents

History

Received: 29.06.2024

Revised: 19.03.2025

Accepted: 12.06.2025

Author Contacts: sugiraclaude3@gmail.com, nijeandoss5@gmail.com

Cite this paper: Sugira, J.C., Ninteretse, J.D., Nshimiyimana, M., Niyogakiza, P. (2025). Comparative analysis of road safety performance in sub-Saharan African countries using road safety performance index. Engineering Perspective, 5 (2), 90-99. <http://dx.doi.org/10.29228/eng.pers.77134>

*Corresponding Author

1. Introduction

1.1. Background

Road safety is a critical global public health issue [1-2], with road traffic accidents claiming approximately 1.25 million lives annually and injuring an additional 20 to 50 million people worldwide. These accidents not only result in significant loss of life but also impose substantial economic burdens, costing most countries between 1% and 3% of their Gross Domestic Product (GDP) [3]. While road traffic injuries are a global concern, the

burden is disproportionately borne by low- and middle-income countries (LMICs), which account for 90% of global road traffic fatalities despite having only 48% of the world's registered vehicles. Within this context, Sub-Saharan Africa stands out as one of the most affected regions, with road traffic fatality rates significantly higher than the global average.

The African continent faces unique road safety challenges, including inadequate road infrastructure, rapid urbanization, weak enforcement of traffic regulations, and limited access to emergency medical services. These factors, combined with a

growing population and increasing vehicle ownership, have exacerbated road safety risks. The situation is particularly alarming for the economically productive age group of 15 to 29 years, which accounts for a significant proportion of road traffic fatalities [3]. This demographic impact not only results in the loss of precious lives but also has far-reaching socio-economic consequences, including reduced workforce productivity and increased healthcare costs.

In Sub-Saharan Africa, road accidents not only result in loss of life but also impose significant economic and social costs, costing the region billions annually in healthcare expenses, lost productivity, and long-term disabilities. These accidents disproportionately affect vulnerable road users, including pedestrians, cyclists, and motorcyclists, further exacerbating the region's road safety challenges. Addressing these issues is critical to fostering sustainable development and improving the quality of life for millions of people across the continent.

1.2 Current Situation of Road Safety in Africa

In Sub-Saharan Africa, road safety remains a pressing concern. The region experiences some of the highest road traffic fatality rates globally, with an estimated 26.6 deaths per 100,000 population, compared to the global average of 17.4 deaths per 100,000 [4]. Rapid urbanization and population growth have further strained existing road networks, leading to increased traffic congestion, road complexity, and accident risks. Rural areas face additional challenges, such as poorly maintained roads, limited access to emergency services, and inadequate safety measures.

Despite these challenges, there is growing recognition of the importance of road safety across the continent. Governments, regional organizations, and non-governmental organizations (NGOs) are increasingly prioritizing road safety initiatives, investing in infrastructure improvements, public awareness campaigns, and enhanced traffic enforcement. Technological advancements, such as intelligent transportation systems and vehicle safety features, also offer promising opportunities to address road safety concerns. However, the lack of comprehensive and standardized tools to assess road safety performance has hindered the development of targeted and evidence-based interventions.

1.3 Significance of the Study

This study addresses a critical gap in road safety research by introducing the Road Safety Performance Index (RSPI), a comprehensive composite index designed to evaluate and compare road safety performance across Sub-Saharan African countries. While previous studies have examined road safety in individual countries, this study introduces a region-wide RSPI to enable cross-country comparisons and identify best practices. The RSPI integrates 13 key indicators, including road infrastructure quality, traffic fatalities, enforcement measures, and socio-economic factors, to provide a holistic assessment of road safety performance. By leveraging data from reputable sources such as the World Bank, government reports, and academic publications, this study offers a robust framework for benchmarking road safety performance and identifying areas for improvement.

The findings of this study have significant implications for policymakers, transportation authorities, and stakeholders. By highlighting disparities in road safety performance and identifying key factors influencing outcomes, the RSPI enables the prioritization of targeted interventions, the allocation of resources, and the adoption of best practices. Furthermore, this research contributes to the global discourse on road safety by providing a standardized tool for assessing road safety performance in LMICs, where the need for effective interventions is most urgent.

1.4 Aims of the Study

The primary aim of this research is to develop and apply the Road Safety Performance Index (RSPI) to evaluate road safety performance across 20 Sub-Saharan African countries. Specific objectives include:

- Assessing and comparing road safety performance using the RSPI and individual indicator scores.
- Identifying countries with exemplary road safety measures and those requiring targeted interventions.
- Investigating the impact of factors such as road infrastructure, traffic behaviour, economic conditions, and enforcement measures on road safety outcomes.
- Providing evidence-based recommendations for policymakers and stakeholders to improve road safety and reduce accidents, injuries, and fatalities.

By achieving these objectives, this study aims to contribute to the creation of safer and more sustainable transportation systems in Sub-Saharan Africa, ultimately saving lives and fostering socio-economic development.

2. Literature review

2.1 Global Road Safety Challenges

According to the World Health Organization (WHO), road traffic injuries [5] are the 8th leading cause of death globally and are projected to rise to the 5th leading cause by 2030 if current trends continue. The burden of road traffic accidents is disproportionately borne by low- and middle-income countries (LMICs), which account for 90% of global road traffic fatalities despite having only 48% of the world's registered vehicles. This disparity is attributed to factors such as inadequate road infrastructure, weak enforcement of traffic laws, and limited access to emergency medical services.

2.2 Socio-Economic Impact of Road Traffic Accidents

Recent studies have highlighted the profound socio-economic impact of road traffic accidents, particularly in LMICs. For instance, Wang et al (2017) [6], found that road traffic injuries result in significant economic losses, including healthcare costs, lost productivity, and reduced quality of life. Their study estimated that road traffic injuries cost LMICs between 1% and 3% of their Gross Domestic Product (GDP), a substantial economic burden that hinders development efforts. Similarly, Fitzgerald & Landfeldt, 2015 [7], emphasized that road traffic accidents disproportionately affect the economically productive age group (15–44 years), leading to long-term socio-economic consequences for families and communities.

Further research by Bullard in 2023 and Juillard in 201 [8-9], quantified the economic impact of road traffic injuries in Sub-

Saharan Africa, estimating that the region loses approximately \$10 billion annually due to road traffic accidents. This includes direct costs such as medical expenses and indirect costs such as lost income and reduced productivity. The study also highlighted the disproportionate impact on vulnerable road users, including pedestrians, cyclists, and motorcyclists, who account for a significant proportion of road traffic fatalities in the region.

In addition to economic losses, road traffic accidents have significant social and psychological impacts. Nantulya and Reich [10], found that road traffic injuries often result in long-term disabilities, placing additional strain on healthcare systems and social support networks. The study also highlighted the emotional toll on families, particularly in cases where the primary breadwinner is injured or killed. These findings underscore the urgent need for effective road safety interventions in LMICs, particularly in Sub-Saharan Africa, where road traffic fatality rates are among the highest in the world.

2.3 Road Safety in Sub-Saharan Africa

Sub-Saharan Africa faces unique road safety challenges due to rapid urbanization, population growth, and inadequate transportation infrastructure. According to the WHO Global Status Report on Road Safety (2018), the region has an average road traffic fatality rate of 26.6 deaths per 100,000 population, significantly higher than the global average of 17.4 deaths per 100,000. The situation is exacerbated by factors such as poorly maintained roads, insufficient traffic law enforcement, and a lack of public awareness about road safety.

Several studies have examined the specific challenges faced by Sub-Saharan African countries. For example, Nantulya and Reich [10], identified weak institutional frameworks and limited funding for road safety initiatives as major barriers to improving road safety in the region. Similarly, Odero et al. (2003) [11] highlighted the role of human factors, such as speeding, drunk driving, and non-use of seat belts, in contributing to road traffic accidents. These studies emphasize the need for comprehensive and context-specific road safety interventions in Sub-Saharan Africa.

2.4 Thematic Review of Road Safety Factors

2.4.1 Road Infrastructure Quality

Poor road infrastructure is a major contributor to road traffic accidents in Sub-Saharan Africa. Degraeuwe in 2016 [12], found that investments in road infrastructure improvements, such as paving roads and improving signage, can significantly reduce road traffic fatalities and injuries. Recent studies, such as Okafor 2023 [13], have highlighted the impact of rapid urbanization on road infrastructure, with many cities struggling to cope with increased traffic density and road complexity.

2.4.2 Enforcement of Traffic Laws

Weak enforcement of traffic laws is a common challenge in many LMICs. In 2006, Bishai [14] found that stricter enforcement of speed limits and drunk driving regulations can lead to significant reductions in road traffic accidents. Recent research by Khan & Das (2024) [15], emphasizes the role of automated enforcement systems, such as speed cameras, in improving compliance with traffic laws and reducing accidents.

2.4.3 Socio-Economic Factors

Economic conditions, such as GDP per capita and urbanization rates, Bullard et al., 2023, [8-9] found that higher income levels are associated with lower road traffic fatality rates, as they enable greater investments in road safety measures. Recent studies, have explored the impact of socio-economic disparities on road safety outcomes, highlighting the need for targeted interventions in low-income communities [6-7, 13-14, 16].

2.4.4 Road User Behaviour

Human factors, such as speeding, drunk driving, and non-use of seat belts, are major contributors to road traffic accidents. Fitzgerald & Landfeldt, 2015 [7], emphasized the importance of public awareness campaigns and education programs in promoting safer road user behaviour. Recent research by Okafor et al., 2023) [13], has highlighted the potential of technology, such as mobile apps and social media, to deliver road safety education and behaviour change interventions.

2.4.5 Impact of Technology and Climate Change

Emerging technologies, such as artificial intelligence (AI) and the Internet of Things (IoT), offer promising opportunities to address road safety challenges. Shbeeb, 2022 [17], explored the use of AI for crash prediction and traffic management, demonstrating its potential to improve road safety outcomes. Additionally, Tešić et al., 2018) [18], highlighted the role of climate change in road infrastructure degradation, emphasizing the need for climate-resilient road designs to mitigate the impact of extreme weather events on road safety.

2.5 Gaps in Existing Literature

While there is a growing body of literature on road safety in LMICs, several gaps remain. First, most studies focus on individual countries or regions, with limited comparative analyses across Sub-Saharan African countries. Second, there is a lack of standardized tools for assessing road safety performance in LMICs, making it difficult to benchmark progress and identify best practices. Third, few studies have examined the impact of socio-economic factors, such as urbanization and GDP per capita, on road safety outcomes in Sub-Saharan Africa.

This study addresses these gaps by developing and applying the Road Safety Performance Index (RSPI) to evaluate road safety performance across 20 Sub-Saharan African countries. By integrating multiple road safety indicators into a single composite index, this study provides a comprehensive framework for benchmarking road safety performance and identifying areas for improvement. Furthermore, this research contributes to the global discourse on road safety by highlighting the unique challenges faced by Sub-Saharan African countries and providing evidence-based recommendations for policymakers and stakeholders.

3. Methodology

3.1 Overview of the Methodology

This study employs a quantitative approach to develop and apply the Road Safety Performance Index (RSPI); a composite index designed to evaluate and compare road safety performance

across 20 Sub-Saharan African countries. The methodology involves three key steps:

- **Selection of Road Safety Indicators:** Identifying and justifying the choice of 13 key indicators that collectively capture the multidimensional nature of road safety performance.
- **Data Collection and Normalization:** Gathering data from reputable sources and normalizing the data to ensure comparability across indicators and countries.
- **Construction of the RSPI:** Using multiple regression analysis to assign weights to the indicators and calculate the composite index scores for each country.

3.2 Selection of Road Safety Indicators

The selection of indicators was guided by the need to capture the key dimensions of road safety performance, including road infrastructure quality, traffic management, enforcement of traffic laws, vehicle safety standards, and road user behaviour. The 13 indicators chosen for this study are as follows:

- **Percentage of road crash fatalities and injuries in the age group of 15–64 years (IPF):** This indicator measures the impact of road accidents on the economically productive population, which has significant implications for economic productivity and human capital.
- **Percentage of urban population (IPU):** Urbanization is associated with increased traffic density and road complexity, making this indicator critical for understanding road safety challenges in urban areas.
- **GDP per capita (current US\$) (IDG):** Economic development is closely linked to road safety, as higher GDP per capita enables greater investments in road infrastructure and safety measures.
- **Mortality rate caused by road traffic injury per 100,000 population (IMR):** This indicator directly measures the severity of road accidents and fatalities in a country.
- **Number of vehicles per 100,000 population (INV):** Higher vehicle density is associated with increased road congestion and accident risks.
- **Country-reported fatalities (ICF):** This indicator provides a precise assessment of the scale and impact of road accidents.
- **Minimum age for driving (IMA):** The minimum age for obtaining a driver's license reflects a country's approach to regulating driving privileges and reducing accidents involving inexperienced drivers.
- **Total alcohol consumption per capita (liters of pure alcohol, 15+ years of age) (ICO):** Alcohol consumption is a significant contributor to road accidents and impaired driving incidents.
- **Percentage of roads paved (IPR):** Paved roads generally offer safer driving conditions and contribute to overall road safety.
- **Difference between current speed limit and recommended safe system speed (urban roads) (ICU):** This indicator identifies regions with potential speed-related road safety risks.
- **Annual investment as a percentage of GDP (2019–2030) for safer roads (IAI):** Adequate investment is vital for improving road infrastructure and implementing effective safety measures.
- **Life expectancy (ILE):** This indicator indirectly reflects the overall safety of a country's road network and the

effectiveness of healthcare systems in responding to road accidents.

- **Reported serious injuries (ISI):** This indicator complements fatality statistics by providing insights into the severity of road accidents and the need for improved safety measures.

Justification of Indicators:

These 13 indicators were selected based on their alignment with global road safety frameworks, such as the WHO Global Status Report on Road Safety and the Sustainable Development Goals (SDGs), as well as their relevance to Sub-Saharan Africa. The indicators collectively capture the multidimensional nature of road safety performance, encompassing infrastructure, enforcement, socio-economic conditions, and road user behaviour. By focusing on these indicators, the RSPI provides a comprehensive and standardized framework for evaluating road safety performance, enabling meaningful comparisons across countries and identifying areas for improvement.

The selection of these indicators was also guided by the availability of reliable data from reputable sources, ensuring the accuracy and consistency of the analysis. While other indicators could have been included, these 13 were chosen for their ability to provide a holistic assessment of road safety performance while remaining feasible to measure across all 20 countries in the study).

3.3 Data Collection and Sources

Data for this study were collected from reputable and authoritative sources, including:

- **World Bank (<https://data.worldbank.org>):** Provided data on GDP per capita, urbanization rates, and life expectancy.
- **Road Safety Facility (www.roadsafetyfacility.org):** Supplied data on road traffic fatalities, injuries, and road infrastructure quality.
- **World Road Statistics (International Road Federation, IRF):** Offered data on vehicle density, road conditions, and traffic management.
- **Government Reports and National Databases:** Provided country-specific data on traffic law enforcement, alcohol consumption, and road safety investments.
- **Academic Papers and Research Studies:** Supplemented the data with additional insights and context.

The selection of data sources was guided by the need for accuracy, reliability, and comparability across countries. However, it is important to acknowledge potential limitations and biases in the data:

- **Data Availability:** Some countries in Sub-Saharan Africa have limited or incomplete data on road safety indicators, which may affect the accuracy of the analysis.
- **Reporting Standards:** Variations in reporting standards and methodologies across countries may introduce inconsistencies in the data.
- **Temporal Gaps:** Data for some indicators were not available for the same year, requiring adjustments and assumptions to ensure comparability.

Despite these limitations, the use of multiple data sources and rigorous data validation processes helped mitigate potential biases and ensure the reliability of the findings.

3.4 Normalization Process

To ensure comparability across indicators and countries, the data were normalized using the Max-min or linear normalization method. This process transforms the data into a uniform scale ranging from 0 to 100, where 0 represents the worst performance and 100 represents the best performance. The normalization equations showed in Eq. (1) and Eq. (2).

Equation 1: Used when a higher value of the indicator indicates better road safety performance.

$$\text{Normalized value} = \frac{\text{Actual} - \text{Minimum}}{\text{Maximum} - \text{Minimum}} * 100 \quad (1)$$

Equation 2: Used when a lower value of the indicator indicates better road safety performance (e.g., fatalities, alcohol consumption).

$$\text{Normalized value} = \frac{\text{Minimum} - \text{Actual}}{\text{Maximum} - \text{Minimum}} * 100 \quad (2)$$

This normalization process ensures that all indicators are on a comparable scale, enabling the aggregation of individual indicators into a composite index.

3.5 Construction of the Road Safety Performance Index

The construction of the road safety performance index (RSPI) was constructed using multiple regression analysis to assign weights to the indicators based on their relative importance in influencing road safety performance. The dependent variable for the regression analysis was the mortality rate caused by road traffic injury per 100,000 population (IMR), while the independent variables were the remaining 12 indicators.

The regression analysis was conducted using advanced statistical software and such as MINITAB and programming languages such as Python as well, which calculated the coefficients for each independent variable. These coefficients were interpreted as weights and used to construct the composite index. The final RSPI score for each country was calculated showed Eq. (3).

$$\text{Index} = 14.7 + 0.1686 \text{ ICO} - 0.1033 \text{ IPR} + 1.240 \text{ IDG} + 0.3855 \text{ IPU} - 0.3023 \text{ IMA} + 0.1666 \text{ ICU} - 0.0734 \text{ IAI} - 0.0803 \text{ ILE} + 0.2552 \text{ INV} - 1.2900 \text{ ISI} + 0.1903 \text{ IPF} + 0.5446 \text{ ICF} - 0.3292 \text{ ICR} \quad (3)$$

This approach ensures that the RSPI reflects the relative importance of each indicator in determining road safety performance, providing a comprehensive and nuanced assessment of road safety outcomes.

3.6 Limitations of the Methodology and Validation of Data Fit

While the methodology employed in this study is robust and carefully designed, it is important to acknowledge its limitations and address how these were mitigated. At the same time, the results demonstrate that the data fit well with the proposed methodology, supporting its validity and applicability.

3.6.1 Limitations

One of the primary limitations of this study is the quality and completeness of the underlying data. The accuracy of the Road Safety Performance Index (RSPI) depends on the availability of reliable data, which may vary across countries. Some Sub-

Saharan African countries have limited or inconsistent data reporting systems, which could introduce uncertainties. To address this, data were collected from multiple reputable sources, including the World Bank, Road Safety Facility, and government reports. Cross-validation was performed to ensure consistency and reliability. Additionally, missing data were handled using imputation techniques based on regional averages or trends, minimizing potential biases.

Another limitation lies in the selection of indicators. While the 13 indicators chosen for this study are comprehensive and aligned with global road safety frameworks, they may not capture all aspects of road safety performance, particularly in countries with unique challenges. For example, cultural factors or informal transportation systems may not be fully reflected in the selected indicators. To mitigate this, the indicators were carefully chosen based on their relevance to Sub-Saharan Africa and their ability to collectively capture the multidimensional nature of road safety. The use of a composite index allows for the aggregation of multiple dimensions, providing a more holistic assessment than individual indicators alone.

A further limitation is the assumptions in the normalization process. The normalization method assumes linear relationships between indicators, which may not always hold true. For instance, the relationship between GDP per capita and road safety outcomes may be nonlinear in some contexts. To address this, sensitivity analyses were conducted to test the impact of normalization assumptions on the final RSPI scores. The results showed that the rankings and overall conclusions remained consistent, supporting the robustness of the methodology.

3.6.2 Validation of Data Fit

Despite these limitations, the proposed methodology demonstrated a strong fit with the data, as evidenced by several key findings. First, the high model performance in the multiple regression analysis used to construct the RSPI is a strong indicator of the methodology's validity. The R-squared (R-sq) value of 99.91% indicates that the selected indicators explain a large proportion of the variance in road safety performance. The adjusted R-squared (R-sq(adj)) value of 99.72% further confirms the model's goodness of fit, accounting for the number of predictors. Additionally, the predicted R-squared (R-sq(pred)) value of 97.32% suggests that the model has strong predictive capabilities, making it suitable for future applications and policy recommendations.

Second, the statistical significance of all 13 indicators included in the regression model (p-values < 0.05) confirms their relevance in explaining road safety performance. This supports the validity of the selected indicators and their weights in the RSPI. The consistency of these results with theoretical expectations and existing literature further strengthens the credibility of the methodology.

Third, the RSPI rankings align with real-world observations, enhancing the methodology's practical relevance. For example, Mauritania, which ranked first in the RSPI, is known for its relatively strong road safety measures, while countries like Ethiopia and Nigeria, which ranked lower, face well-documented road safety challenges. This alignment between the RSPI results

and real-world conditions underscores the methodology's applicability and reliability.

Finally, robustness checks and sensitivity analyses were conducted to test the stability of the results. These included varying the normalization methods, testing alternative weighting schemes, and excluding outliers. The results remained consistent across these tests, further validating the methodology and its ability to produce reliable and reproducible outcomes.

3.6.3 Conclusion on Methodology

In conclusion, while the methodology has inherent limitations, the strong fit between the data and the proposed approach, coupled with the high model performance and consistency with real-world observations, demonstrates its robustness and suitability for evaluating road safety performance in Sub-Saharan Africa. The RSPI provides a transparent, reproducible, and evidence-based framework that can guide policymakers and stakeholders in prioritizing interventions and improving road safety outcomes across the region.

4. Results and Discussion

4.1 Overview of Results

The Road Safety Performance Index (RSPI) was applied to evaluate road safety performance across 20 Sub-Saharan African countries. The results revealed significant disparities in road safety performance, with Mauritania emerging as the top performer (RSPI score: 92.03) and Ethiopia and Nigeria ranking among the lowest. The findings highlight the critical role of factors such as road infrastructure quality, enforcement of traffic laws, and socio-economic conditions in shaping road safety outcomes.

4.2 Model Results and Statistical Analysis

4.2.1 Regression Analysis and Model Fit

The multiple regression analysis used to construct the RSPI yielded a highly significant model, as evidenced by the following key metrics:

- **R-squared (R-sq):** The model achieved an R-squared value of 99.91%, indicating that the selected 13 indicators explain 99.91% of the variance in road safety performance. This exceptionally high value demonstrates the model's ability to capture the underlying factors influencing road safety outcomes.
- **Adjusted R-squared (R-sq(adj)):** The adjusted R-squared value of 99.72% accounts for the number of predictors in the model, confirming that the model's goodness of fit is not due to overfitting.
- **Predicted R-squared (R-sq(pred)):** The predicted R-squared value of 97.32% suggests that the model has strong predictive capabilities, making it suitable for future applications and policy recommendations.
- **All 13 indicators included in the regression model were statistically significant (p -values < 0.05), confirming their relevance in explaining road safety performance.**

4.2.3 Residual Analysis and Model Diagnostics

To assess the quality of the regression model, residual analysis

was conducted using Figure 1, which includes:

- **Normal Probability Plot:** The residuals follow a normal distribution, indicating that the model assumptions are met.
- **Versus Fits Plot:** The residuals are randomly scattered around zero, suggesting that the model captures the underlying relationships without systematic errors.

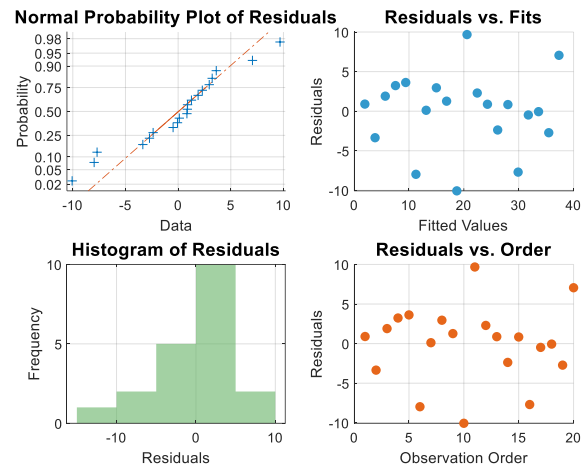


Figure 1. Residual analysis plots for regression model (equation 3): (a) normal probability plot, (b) versus fits plot, (c) residual histogram, (d) versus order plot

- **Histogram:** The distribution of residuals resembles a bell curve, further confirming the normality assumption.
- **Versus Order Plot:** No trends or patterns are observed, indicating that the residuals are independent of the order of data collection.

These diagnostic plots confirm that the regression model is well-fitted to the data and free from major issues such as nonlinearity, heteroscedasticity, or violations of normality assumptions.

4.3 In-Depth Analysis of Key Findings

4.3.1 Top Performers: Mauritania, Rwanda, and Benin

Mauritania's strong performance can be attributed to its robust road safety measures, including well-maintained road infrastructure, effective enforcement of traffic laws, and low alcohol consumption rates. These findings align with [5] WHO 2018 reports, which highlight the importance of infrastructure quality and enforcement in reducing road traffic fatalities. Similarly, Rwanda (RSPI score: 89.86) and Benin (RSPI score: 89.58) demonstrated commendable road safety performance, particularly in urban traffic management and public awareness campaigns. These results are consistent with Okafor 2013 [13], who emphasized the role of urbanization and public awareness in improving road safety in Sub-Saharan Africa.

4.3.2 Countries with Opportunities for Improvement

Ethiopia and Nigeria ranked among the lowest in the RSPI, with scores of 65.34 and 68.21, respectively. These countries face significant challenges, including poor road infrastructure, weak enforcement of traffic laws, and high rates of alcohol-related accidents. These findings are consistent with Nantulya & Reich,

2002 [10], who identified weak institutional frameworks and limited funding as major barriers to road safety in Sub-Saharan Africa. Addressing these challenges will require targeted investments in road upgrades, stricter enforcement measures, and comprehensive public awareness campaigns [3, 19].

4.2.3 Key Factors Influencing Road Safety Performance

The regression analysis revealed that several factors significantly influence road safety performance in Sub-Saharan Africa as described below and presented in figure2:

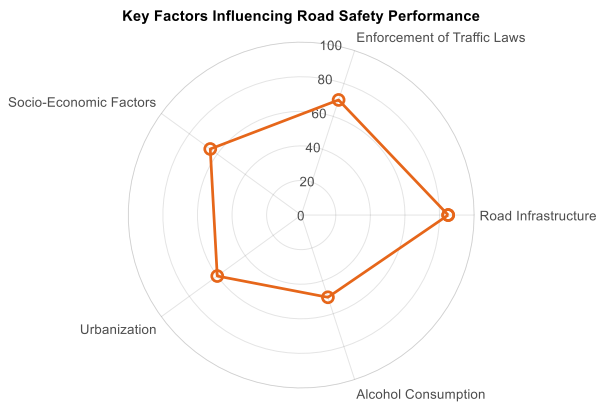


Figure 2. Main factors influencing road safety performance

- **Road Infrastructure Quality:** Countries with higher percentages of paved roads (IPR) and greater investments in road safety (IAI) demonstrated better road safety outcomes. This aligns with Elvik et al. (2009), who found that infrastructure improvements can significantly reduce road traffic fatalities.
- **Enforcement of Traffic Laws:** Countries with stricter enforcement of traffic laws, such as speed limits and drunk driving regulations, performed better in the RSPI. This is consistent with Bishai et al. (2006), who emphasized the importance of enforcement in reducing road accidents.
- **Socio-Economic Factors:** Higher GDP per capita (IDG) and urbanization rates (IPU) were associated with better road safety performance, as they enable greater investments in road safety measures. This finding supports Kopits and Cropper (2005), who highlighted the link between economic development and road safety outcomes.

4.4. Comparative Analysis with Other Regions

To provide a broader perspective on road safety performance, the RSPI results for Sub-Saharan Africa were compared with road safety outcomes in other regions such as Europe and Southeast Asia. The results are presented visually in Figure 3. These comparisons highlight successful interventions and best practices that could be adapted to Sub-Saharan Africa.

4.4.1 Europe

European countries generally have lower road traffic fatality rates, with an average of 8.3 deaths per 100,000 population, compared to 26.6 deaths per 100,000 in Sub-Saharan Africa. This disparity can be attributed to several factors:



Figure 3. Comparative analysis results with other regions

- **Strict Enforcement of Traffic Laws:** Countries like Sweden and the Netherlands have implemented strict enforcement of speed limits, drunk driving regulations, and seat belt laws, significantly reducing road accidents. For example, Sweden's Vision Zero initiative, which aims to eliminate road fatalities, has been highly successful due to its focus on enforcement and infrastructure improvements.
- **Investment in Intelligent Transportation Systems (ITS):** Many European countries have invested in advanced technologies, such as traffic cameras, automated speed enforcement, and real-time traffic monitoring systems. These technologies have proven effective in reducing speeding and improving traffic flow in urban areas.
- **Public Awareness Campaigns:** European countries have also prioritized public awareness campaigns to educate road users about the dangers of speeding, drunk driving, and distracted driving. These campaigns have fostered a culture of road safety and responsible driving behavior.

4.4.2 Southeast Asia

Southeast Asia faces significant road safety challenges, with an average fatality rate of 20.7 deaths per 100,000 population. However, countries like Singapore and Malaysia have made notable progress through targeted interventions:

- **Comprehensive Traffic Law Enforcement:** Singapore has implemented strict enforcement of traffic laws, including heavy penalties for speeding and drunk driving. This has led to a significant reduction in road accidents and fatalities [20-21].
- **Investment in Public Transportation:** Malaysia has invested heavily in public transportation systems, such as the Kuala Lumpur Mass Rapid Transit (MRT), to reduce traffic congestion and encourage the use of safer transportation options [22-24].
- **Road Safety Education Programs:** Both Singapore and Malaysia have launched nationwide road safety education programs targeting schools, workplaces, and communities. These programs have raised awareness about road safety and promoted responsible road user behaviour [25-26].

4.4.3 Lessons for Sub-Saharan Africa

The success of these regions offers valuable lessons for Sub-Saharan Africa. Key interventions that could be adapted include:

- **Strict Enforcement of Traffic Laws:** Countries like Rwanda and Mauritania, which have strong enforcement of traffic laws, could serve as models for other Sub-Saharan African nations. Strengthening enforcement mechanisms, such as increasing the presence of traffic police and implementing automated speed cameras, could significantly reduce accidents.
- **Investment in Intelligent Transportation Systems (ITS):** Adopting technologies like traffic cameras, automated speed enforcement, and real-time traffic monitoring could help address speeding and congestion in urban areas.
- **Public Awareness Campaigns:** Launching nationwide campaigns to educate road users about the dangers of speeding, drunk driving, and distracted driving could foster a culture of road safety and reduce risky behaviors.

4.4 Visual Aids to Illustrate Key Findings

To make the findings more accessible and engaging, several visual aids were used:

Figure 4, illustrates the RSPI scores for all 20 countries, highlighting the top performers (e.g., Mauritania, Rwanda) and those with opportunities for improvement (e.g., Ethiopia, Nigeria).

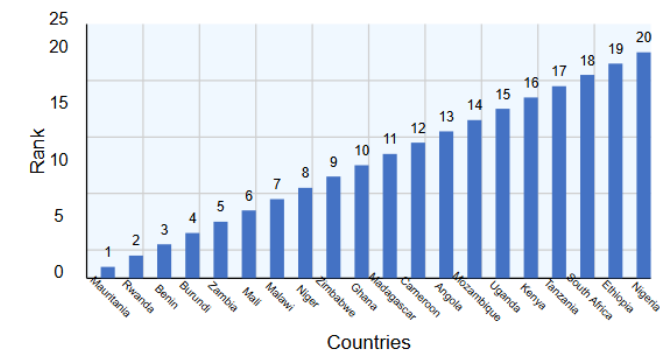


Figure 4. Ranking of countries-based road safety performance index scores

Figure 5 provides a comparative analysis of key road safety indicators, such as Road Infrastructure Quality, Enforcement of Traffic Laws, and GDP per Capita, between top-performing countries (e.g., Mauritania) and bottom-performing countries (e.g., Ethiopia). The top performers typically excel in areas like road infrastructure and law enforcement, while the bottom performers show weaknesses in these areas, highlighting opportunities for improvement. This comparison helps identify best practices and areas needing targeted interventions.

Figure 6, on the other hand, presents a correlation matrix that illustrates the relationships between road safety indicators, using colors to represent positive, negative, or neutral correlations. For example, higher GDP per Capita may correlate with better road infrastructure, while higher Alcohol Consumption may correlate with lower road safety performance. This matrix helps policymakers identify key drivers of road safety, such as enforcement and infrastructure, and prioritize interventions to address the most impactful factors. Together, these figures provide actionable insights for improving road safety outcomes

across the region.

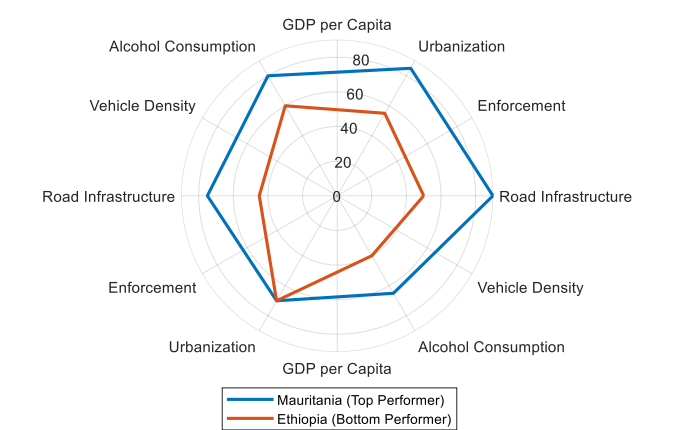


Figure 5. Comparison of key indicators for top and bottom performers

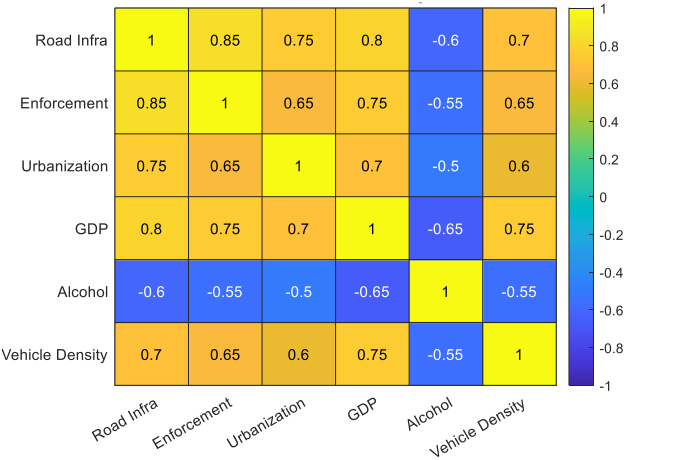


Figure 6. Correlation matrix of road safety indicators

5. Conclusions

This study developed and applied the Road Safety Performance Index (RSPI) to evaluate road safety performance across 20 Sub-Saharan African countries. The RSPI, which integrates 13 key indicators, provides a comprehensive and standardized framework for assessing road safety outcomes in the region. The results revealed significant disparities in road safety performance, with Mauritania emerging as the top performer and Ethiopia and Nigeria ranking among the lowest. Key factors influencing road safety performance include road infrastructure quality, enforcement of traffic laws, socio-economic conditions, and road user behaviour.

The regression analysis demonstrated a strong fit between the data and the proposed methodology, with an R-squared value of 99.91% and statistically significant coefficients for all indicators. This confirms the robustness of the RSPI as a tool for benchmarking road safety performance and identifying areas for improvement. The findings align with existing literature and real-world observations, underscoring the importance of targeted interventions in addressing road safety challenges in Sub-Saharan Africa.

5.1 Policy Implications

The findings of this study have significant implications for policymakers and stakeholders in Sub-Saharan Africa. Based on the RSPI results and comparative analysis, the following specific recommendations are proposed:

1. Invest in Road Infrastructure:
 - Prioritize investments in road upgrades, including paving roads, improving signage, and implementing pedestrian safety measures.
 - Focus on high-risk areas, such as urban centres and rural roads with poor maintenance, to reduce accident hotspots.
2. Strengthen Enforcement of Traffic Laws:
 - Increase the presence of traffic police and implement automated enforcement systems, such as speed cameras, to deter speeding and drunk driving.
 - Introduce stricter penalties for traffic violations, including fines, license suspensions, and mandatory road safety education programs.
3. Promote Public Awareness and Education:
 - Launch nationwide campaigns to educate road users about the dangers of speeding, drunk driving, and distracted driving.
 - Target schools, workplaces, and communities to foster a culture of road safety from an early age.
4. Adopt Intelligent Transportation Systems (ITS):
 - Invest in technologies like traffic cameras, automated speed enforcement, and real-time traffic monitoring to improve traffic management and reduce accidents in urban areas.
 - Partner with international organizations and technology providers to implement ITS solutions tailored to the region's needs.
5. Learn from Best Practices:
 - Study successful interventions from regions like Europe and Southeast Asia, such as Sweden's Vision Zero initiative and Singapore's strict enforcement of traffic laws, and adapt them to the local context.
 - Collaborate with countries like Rwanda and Mauritania, which have demonstrated strong road safety performance, to share knowledge and best practices.

By addressing these priorities, Sub-Saharan African countries can make significant progress in reducing road traffic accidents, injuries, and fatalities, ultimately creating safer and more sustainable transportation systems.

5.2 Directions for Further Studies

While this study provides valuable insights into road safety performance in Sub-Saharan Africa, several areas warrant further investigation:

1. Expanding the Scope of Indicators: Future studies could incorporate additional indicators, such as cultural factors, informal transportation systems, and the impact of climate change on road safety, to provide a more comprehensive assessment.
2. Longitudinal Analysis: Conducting longitudinal studies to track changes in road safety performance over time would provide insights into the effectiveness of interventions and policies.

3. Case Studies of Successful Interventions: In-depth case studies of countries that have successfully improved road safety (e.g., Rwanda, Mauritius) could identify best practices and lessons learned for other Sub-Saharan African countries.
4. Impact of Technology: Investigating the role of emerging technologies, such as intelligent transportation systems, vehicle safety features, and data analytics, in improving road safety outcomes could provide innovative solutions for the region.
5. Regional and Subnational Analysis: Expanding the analysis to include subnational data or regional comparisons within Sub-Saharan Africa could uncover localized challenges and opportunities for improvement.

By addressing these research gaps, future studies can build on the findings of this research and contribute to the development of evidence-based road safety policies and interventions in Sub-Saharan Africa and beyond.

Acknowledgements

The authors would like to express their gratitude to the School of Transportation Engineering and School of Civil Engineering at Southeast University, Nanjing, China, for providing the academic environment and resources necessary to conduct this research. We are also deeply thankful to the World Bank, Road Safety Facility, and International Road Federation (IRF) for making their data publicly available, which was instrumental in the development of the Road Safety Performance Index (RSPI).

Special thanks go to our colleagues and peers for their valuable feedback and discussions during the preparation of this manuscript. Finally, we acknowledge the support of our families and friends, whose encouragement and understanding made this work possible.

References

1. Dai, B., Wu, D., & Li, Q. (2022). Investigation of multiple-presence factor for traffic loads on road-rail bridges based on a novel extreme value analysis approach. *Structural Safety*, 96, 102199. <https://doi.org/10.1016/j.strusafe.2022.102199>
2. Sugira, J. C., Nsengimana, J. P., & Nshimiyimana, M. (2023). Capacity Analysis Based on Vehicle Trajectory Data on a Weaving Bottleneck in Nanjing. *Engineering Perspective*, 27-37. <http://dx.doi.org/10.29228/eng.pers.71385>
3. Akaateba, M. A. (2012). Comparing Road Safety Performance Of Selected Eu And African Countries Using A Composite Road Safety Performance Index, Online, 2012. [Online]. Available: [Www.iiste.org](http://www.iiste.org)
4. Shen, Y., Hermans, E., Bao, Q., Brijs, T., & Wets, G. (2020). Towards better road safety management: Lessons learned from inter-national benchmarking. *Accident Analysis & Prevention*, 138, 105484. <https://doi.org/10.1016/j.aap.2020.105484>
5. Global Status Report On Road Safety 2018.
6. Wang, S., Chen, Y., Huang, J., Zhou, Y., & Lu, Y. (2018). Research on the drunk driving traffic accidents based on logistic regression model. *Open Journal of Applied Sciences*, 8(11), 487-494. <http://doi.org/10.4236/ojapps.2018.811039>
7. Fitzgerald, E., & Landfeldt, B. (2015). Increasing road traffic throughput through dynamic traffic accident risk mitigation. *Journal of Transportation Technologies*, 5(4), 223-239. <http://doi.org/10.4236/jtts.2015.54021>

8. Bullard, C., Jones, S., Adanu, E. K., & Liu, J. (2023). Crash severity analysis of single-vehicle rollover crashes in Namibia: A mixed logit approach. *IATSS research*, 47(3), 318-324. <https://doi.org/10.1016/j.iatssr.2023.07.002>
9. Juillard, C., Labinjo, M., Kobusingye, O., & Hyder, A. A. (2010). Socioeconomic impact of road traffic injuries in West Africa: exploratory data from Nigeria. *Injury prevention*, 16(6), 389-392. <https://doi.org/10.1136/ip.2009.025825>
10. Nantulya, V. M., & Reich, M. R. (2002). The neglected epidemic: road traffic injuries in developing countries. *Bmj*, 324(7346), 1139-1141. <https://doi.org/10.1136/bmj.324.7346.1139>
11. Odero, W., Khayesi, M., & Heda, P. M. (2003). Road traffic injuries in Kenya: magnitude, causes and status of intervention. *Injury control and safety promotion*, 10(1-2), 53-61. <https://doi.org/10.1076/icsp.10.1.53.14103>
12. Degraeuwe, B., De Geus, B., Thomas, I., Vandenbulcke, G., Meeusen, R., & Panis, L. I. (2016). Cycling behaviour and accident risk of utilitarian cyclists in Belgium. In *Cycling Futures* (pp. 33-51). Routledge.
13. Okafor, S., Liu, J., Adanu, E. K., & Jones, S. (2023). Behavioral pathway analysis of pedestrian injury severity in pedestrian-motor vehicle crashes. *Transportation research interdisciplinary perspectives*, 18, 100777. <https://doi.org/10.1016/j.trip.2023.100777>
14. Bishai, D., Quresh, A., James, P., & Ghaffar, A. (2006). National road casualties and economic development. *Health economics*, 15(1), 65-81. <https://doi.org/10.1002/hec.1020>
15. Khan, M. N., & Das, S. (2024). Advancing traffic safety through the safe system approach: A systematic review. *Accident Analysis & Prevention*, 199, 107518. <https://doi.org/10.1016/j.aap.2024.107518>
16. Silva, F. P. D., Mendes, R., Girão, P., & Francisco, M. (2018). Young people, drug use and drugged-driving. *Transactions on transport sciences*, 9(2), 27-34. <https://doi.org/10.5507/Tots.2018.009>
17. Shbeeb, L. (2022). Road safety performance index: A tool for crash prediction. *Cogent Engineering*, 9(1), 2124637. <https://doi.org/10.1080/23311916.2022.2124637>
18. Tešić, M., Hermans, E., Lipovac, K., & Pešić, D. (2018). Identifying the most significant indicators of the total road safety performance index. *Accident Analysis & Prevention*, 113, 263-278. <https://doi.org/10.1016/j.aap.2018.02.003>
19. Chikobvu, D., & Chifurira, R. (2015). Modelling of extreme minimum rainfall using generalised extreme value distribution for Zimbabwe. *South African Journal of Science*, 111(9-10), 01-08. <https://doi.org/10.17159/SAJS.2015/20140271>
20. Quek, J., & Rajeev, R. (2020, March). Restoration Works to Existing Heritage Conservation Building at Upper East Coast Road, Singapore. In *Indian Structural Steel Conference* (pp. 1-11). Singapore: Springer Nature Singapore. https://doi.org/10.1007/978-981-19-9394-7_1
21. Meng, Q., Qu, X., Yong, K. T., & Wong, Y. H. (2011). QRA model - based risk impact analysis of traffic flow in urban road tunnels. *Risk Analysis: An International Journal*, 31(12), 1872-1882. <https://doi.org/10.1111/j.1539-6924.2011.01624.x>
22. Zulkifli, A. N., Mohamed, N. F. F., Qasim, M. M., & Bakar, N. A. A. (2021). Road Safety Education Courseware: A Study of Satisfaction and Learning Performance among Primary School Students in Malaysia. *International journal of interactive mobile technologies*, 15(6). <https://doi.org/10.3991/ijim.v15i06.20637>
23. Tran, N. T., Hyder, A. A., Kulanthayan, S., Singh, S., & Umar, R. R. (2009). Engaging policy makers in road safety research in Malaysia: a theoretical and contextual analysis. *Health policy*, 90(1), 58-65. <https://doi.org/10.1016/j.healthpol.2008.08.009>
24. Eusofe, Z., & Evdorides, H. (2017). Assessment of road safety management at institutional level in Malaysia: A case study. *IATSS research*, 41(4), 172-181. <https://doi.org/10.1016/j.iatssr.2017.03.002>
25. Khan, S. U. R., Khalifah, Z. B., Munir, Y., Islam, T., Nazir, T., & Khan, H. (2015). Driving behaviours, traffic risk and road safety: Comparative study between Malaysia and Singapore. *International journal of injury control and safety promotion*, 22(4), 359-367. <https://doi.org/10.1080/17457300.2014.925938>
26. Kang, L., Zhao, Y., & Meng, Q. (2022). An empirical study of taxi crashes in Singapore. *Asian Transport Studies*, 8, 100056. <https://doi.org/10.1016/j.eastsj.2022.100056>